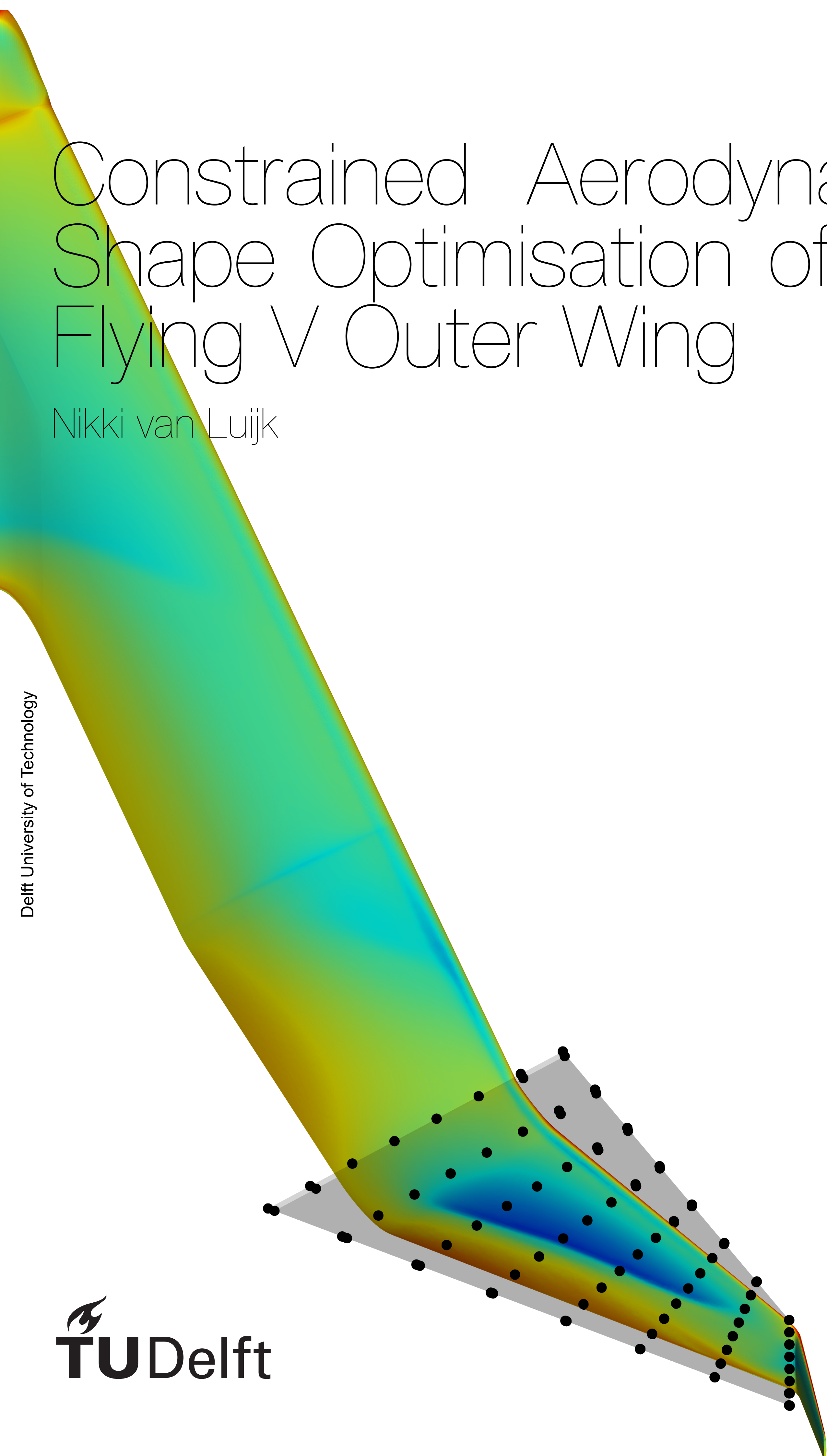

Constrained Aerodynamic Shape Optimisation of the Flying V Outer Wing

Nikki van Luijk

Delft University of Technology

TU Delft

Constrained Aerodynamic Shape Optimisation of the Flying V Outer Wing

by

Nikki van Luijk

to obtain the degree of Master of Science at the Delft University of Technology,
to be defended publicly on Wednesday March 8, 2023 at 13:30.

Studentnumber:	4551842	
Institution:	Delft University of Technology	
Project Duration:	09, 2021 - 03, 2023	
Supervisor:	Dr. ir. R. Vos	
Thesis Committee:	Dr. ir R. Vos	TU Delft, Supervisor & Chair
	Dr. ir A.H. van Zuijlen	TU Delft, External Examiner
	Dr. ir. J. Benad	TU Delft, Examiner
	ir. M. Pini	TU Delft, Examiner

TU Delft

Preface

With this thesis, an end has come to my time as a student in Delft. While this project followed a somewhat unconventional planning by starting the literature study in my first year of the master's next to my courses, and taking a 6 month break for my internship, in the end, I can say that I am proud of the result. Conducting this thesis partly from home during the COVID-19 pandemic also made me realise the positive effects of having fellow students around. Therefore, I am grateful for the long days at the university with my friends when this was possible again. While this project was not easy at all times due to the unforeseen setbacks, unconventional planning, and the pandemic, it brought me many new insights and sparked my interest in research. For this, I must admit that I owe a lot to all the people involved in the thesis project as well as in my personal life.

To start, I would like to thank Roelof Vos who gave me the opportunity to work on this project and trusted me to take it to a successful conclusion. Our meetings involved many interesting discussions and brainstorming sessions to tackle the unforeseen setbacks, and guided me in the correct direction when needed. Roelof's feedback in combination with his eye for detail ensured the academic quality of this work for which I am grateful. I would also like to thank Justus Benad who joined the faculty while I was working on this project. Having the creator of the Flying V concept providing feedback on the design strategy was of invaluable help. Especially when Roelof was unavailable in the later stages of my thesis, the discussions and afternoons spent on the issues I was facing helped me to find a way out. Many discussions also took place with my fellow students working on the Flying V. As we were all facing similar problems at a certain stage, being able to brainstorm on it together turned out to be very valuable. For this, I want to thank all of you and hope you can also be proud of your final result. The last persons I want to thank for their contribution to this study are Max Baan and Reinier van Dijk from ParaPy. They provided me with the experimental Gordon surfaces functionality which has not been implemented in the platform yet. Particularly the many emails discussing the functionality of this new module were of much help in using the new lofting technique to the best of the current abilities.

On a personal note, there are also many people who helped me get through the thesis when things were not looking very bright. For this, I would like to thank my boyfriend Christopher who always kept my spirit high despite my many complaints at certain times. Similarly, I would like to thank my roommates for providing welcome distractions by playing games together as well as putting up with my sometimes stressed self. Additionally, I would like to thank my family and friends to whom I could always go to get out of the thesis mindset for a weekend or a night. To all the people who helped me achieve this feat while always keeping faith in me, I will forever be grateful for you.

Nikki van Luijk
Delft, February 2023

Executive Summary

As long as people tend to fly more and more, the need for more sustainable aircraft will continue to increase as well. However, the efficiency seems to be stagnating with the current state-of-the-art aircraft. Therefore, new and unconventional configurations should be considered. This idea was brought to life in the design of the Flying V. In its current state, however, its aerodynamic performance is worse than reference aircraft such as the Airbus A350. The goal of this study is therefore to optimise the design of the outboard wing of the Flying V to maximise the lift-to-drag ratio. For this, an aerodynamic design strategy is devised consisting out of various steps. These include the geometry preparation phase in which the existing parametrisation is adjusted to include the new lofting technique making use of Gordon surfaces. The use of Gordon surfaces removes several undesired characteristics of the initially linear lofted geometry such as the streamwise discontinuities, toroidal geometry, and sharp leading and trailing edge kinks. The next step is to perform a baseline design optimisation in which the planform variables of this new parametrisation are optimised with the objective of attaining an elliptical lift distribution. This is done via an optimisation guided by the Differential Evolution algorithm and Athena Vortex Lattice. The designs originating from the optimisation are subsequently evaluated by analysing them with the Euler equations flow model of SU2. Additionally, the outboard control surfaces are sized to furthermore ensure the feasibility of the design from a controllability perspective. Structural recommendations following from earlier conducted studies are also included by increasing the overall taper ratio and thickness-to-chord ratio of the tip section. The resulting designs of these first two steps are analysed using the Reynolds Averaged Navier Stokes (RANS) equations model of SU2 to provide a better understanding of the effects of the design changes.

This is followed by a constrained aerodynamic shape optimisation conducted using the Free-Form Deformation (FFD) parametrisation method implemented in SU2. The FFD optimisation is guided by the Sequential Least Squares Programming algorithm and relies on the Euler equations. The objective of this optimisation is to minimise the drag coefficient of the aircraft at its design condition. The resulting drag coefficient is augmented with an empirical viscous drag approximation to account for the viscous drag components to provide a more accurate prediction. This is furthermore ensured by establishing a correlation between the RANS model and the Euler model augmented with the empirical drag module. The FFD optimisation is moreover subjected to constraints related to the pitching moment coefficient, the continuity with respect to the inboard wing and winglets, and the integration of the outboard control surfaces. To evaluate the effect of the control surface constraint, a FFD optimisation neglecting this constraint is conducted as well. This results in 240 design variables, whereas including this constraint reduces the design flexibility to 220 variables. The mesh used in both the RANS and Euler flow analyses is composed of 6.2 million cells as this provides a balance between the accuracy of the results and the required computational time.

The re-parametrisation leads to the largest efficiency increase observed in this study, as well as the highest lift-to-drag ratio. In particular, the efficiency increased from 17.9 to 21.4 representing a rise of 19.6%. It however also results in a thick outboard wing suffering from strong shock waves which render the outboard wing inefficient. The subsequent baseline design optimisation reduces the aerodynamic efficiency to 19.1 as a result of the implemented design changes related to the structural considerations. The FFD optimisation thereafter increases the lift-to-drag ratio to 19.4 by mitigating these effects. However, the control surface constraint severely limits the optimiser as a maximum lift-to-drag ratio of 20.3 can be attained when neglecting this constraint, indicating that the constraint results in a 4.4% decrease in efficiency. Additionally, it is noted that the pitching moment coefficient constraint is not met by all designs considered in this study. This is attributed to the inefficient outboard wing in combination with the large suction area on the nose of the aircraft caused by the integration of the cockpit. Overall, the complete aerodynamic design process results in an 8.4% and 13.4% increase in aerodynamic efficiency with respect to the initial linear lofted geometry depending on the integration of the control surface constraint.

Contents

Nomenclature

Abbreviations

Abbreviation	Definition
API	Application Programming Interface
AVL	Athena Vortex Lattice
CFD	Computational Fluid Dynamics
DE	Differential Evolution
FFD	Free-Form Deformation
HPC	High Performance Computing
JST	Jameson Schmidt Turkel central scheme
KKT	Karush-Kuhn-Tucker
LE	Leading edge
MAC	Mean Aerodynamic Chord
MMG	Multi-Model Generator
RANS	Reynolds Averaged Navier Stokes
ROE	Roe upwind scheme
SA	Spalart-Allmaras turbulence model
SA-E	Spalart-Allmaras turbulence model with Edwards correction
SA-NEG	Negative Spalart-Allmaras turbulence model
SLSQP	Sequential Least Squares Programming
SST	Shear Stress Transport turbulence model
SU2	Stanford University Unstructured Code

Symbols

Symbol	Definition	Unit
AR	Aspect ratio	[-]
b	(Semi-)Wing span	[m]
C_D	Drag coefficient	[-]
C_{D0}	Zero lift drag coefficient	[-]
C_{D_f}	Friction drag coefficient	[-]
$C_{D\text{inv}}$	Inviscid drag coefficient	[-]
C_{D_p}	Pressure drag coefficient	[-]
C_f	Friction coefficient in x direction	[-]
C_L	Lift coefficient	[-]
C_l	Sectional lift coefficient	[-]
C_m	Pitching moment coefficient	[-]
C_p	Pressure coefficient	[-]
C_p^*	Critical pressure coefficient	[-]
c	Chord length	[m]
$\bar{c}$	Mean aerodynamic chord length	[m]
E	Normalised lift distribution	[-]
e	Oswald efficiency factor	[-]
f	Form factor	[-]

Symbol	Definition	Unit
h	Altitude	[m]
k	Kink relative position	[-]
L_4	Leading edge kink position	[m]
M	Mach number	[-]
Re	Reynolds number	[-]
S	Surface area	[m^2]
S_{ref}	Wing reference area	[m^2]
S_{wet}	Wetted surface area	[m^2]
T_∞	Free stream temperature	[K]
t/c	Thickness-to-chord ratio	[-]
V	Velocity	[m/s]
$\overline{x}$	Design vector	[-]
y^+	Non-dimensional first layer height	[-]
α	Angle of attack	[°]
Γ	Dihedral angle	[°]
δ	Orientation angle of section 4	[°]
δ_{99}	99% Boundary layer thickness	[m]
δs	Hinge line offset	[m]
ϵ	Angle of incidence	[°]
η	Spanwise position	[-]
Λ	Sweep angle	[°]
λ	Taper ratio	[-]
μ	Torus angle	[°]
μ_∞	Free stream dynamic viscosity	[Ns/m^2]
ρ_∞	Free stream density	[kg/m^3]

Subscripts

Symbol	Definition
cg	Centre of gravity
con	Control surface
cr	Cruise
in	Inboard
opt	Optimal
out	O utboard
r	Root
t	Tip
0	Initial
∞	Free stream

List of Figures

List of Tables

1
Introduction

Ever since the commercialisation of the aviation sector, tremendous efforts have been undertaken to improve the performance of aircraft. This resulted in the well-known tube-wing aircraft configuration which has dominated the sky over the past 50 years. Thanks to advancements in the fields of, for example, the power-plant, avionics and aerodynamic design, modern-day airliners are twice as efficient as passenger aircraft from five decades ago [1]. Nevertheless, it appears that with the current state-of-the-art aircraft such as the Boeing 787 and the Airbus A350, the efficiency has reached a plateau. The efficiency of these tube-wing aircraft cannot be doubled once again despite further developments in the many fields of aircraft design and manufacturing [2]. However, there is ever increasing public and political pressure to make the aviation industry more efficient, and, consequently, sustainable [1] [2]. Additionally, the sector is anticipated to grow excessively after recovering from the COVID-19 pandemic, while restrictions on noise, pollution and environmental impact are tightened [3]. New solutions must thus be explored.

1.1. Flying Wings & Blended Wing Bodies

A solution is found in radically different aircraft configurations. Several studies conducted by Qin et al. put forward the flying wing and blended wing body concept as the solution to reducing the environmental impact of aircraft [3–5]. More specifically, these types of configurations have the potential to reduce the fuel consumption per seat-kilometer. This is ascribed to the reduction in wetted area per unit volume due to the blending of the aerodynamic shape, structural components, and the payload bay. Additionally, these aircraft do not require high lift devices during take-off and landing, reducing the noise pollution as well [1, 6]. While it is suggested that these aircraft configurations can be the solution to the current sustainability problem, flying wings and blended wing bodies have been around since the start of the aviation era. The first recorded flight of a tailless aircraft already took place in 1911 with the D-8 tailless biplane developed by John Dunne [2, 7]. Thenceforth, developments in the field of unconventional aircraft configurations advanced thanks to many pioneers such as Alexander Lippisch, who built the very first delta wing aircraft [8]. These discoveries led to the well-known Aérospatiale-BAC Concorde passenger aircraft, and its Russian counterpart the Tupolev Tu-144. To this day, these remain the only tailless passenger aircraft on the commercial market. On the contrary, various military fighter aircraft were designed according to the flying wing or tailless aircraft principle, with the prime example being the Northtrop Grumman B-2 Spirit Bomber [6]. Yet, a commercial passenger aircraft in the form of a flying wing is still a dream today.

Studies showed, however, that the that the aerodynamic performance of aircraft alike is superior to the current conventional configurations [1–3]. Still, before the commercial aviation market can also make use of the advantages of blended wing bodies and flying wings, it must first overcome the challenges associated with these type of passenger aircraft. Stability and controllability issues limit the aircraft to

[1] NATS Aviation index 2020, Retrieved on 25-04-2022 from `https://www.nats.aero/features/aviation-index-2020/`
[2] Destination 2050, Retrieved on 25-04-2022 from `https://www.destination2050.eu`
[3] Economic Impacts of COVID-19 on Civil Aviation, Retrieved on 25-04-2022 from `https://www.icao.int/sustainability`

be only viable in cruise, and the weight of a non-circular fuselage are merely examples of the issues faced [6]. Nonetheless, attempts were made by Qin et al., and Lyu and Martins to devise a design of a passenger blended wing body. Qin et al. used a multi-fidelity approach to evaluate the aerodynamic characteristics of the designed aircraft. The analysis started with a low-fidelity panel method, while gradually increasing the fidelity of the aerodynamic model via the Euler equations to the Reynolds Averaged Navier Stokes equations (RANS) [3, 5]. On the other hand, Lyu and Martins used a single-fidelity aerodynamic model based on the RANS equations. The design was concurrently devised via a gradient based optimisation approach [9]. A similar approach was verified by Reist et al. for the investigation into a hybrid blended wing body [10]. While these studies show promising results, more research is needed by considering other design aspects apart from the aerodynamic performance of the novel configuration.

1.2. The Flying V

Also Benad saw the advantages of blended wing bodies and flying wings and took on the challenge to develop a conceptual design of a passenger aircraft of that type. Together with the Future Project Office (FPO) at Airbus GmbH, this study resulted in the Flying V. According to Benad the idea of the Flying V is "...to arrange two cylindrical pressurized sections for the payload swept back in the shape of a V and place them inside the front section of a wing with the same sweep angle" [6]. This results in the configuration shown in figure 1.1. Directional control is established via the rudders located on the winglets, whereas lateral and longitudinal control is ensured by elevons and split flaps positioned on the outboard wing. The main goal for proposing this novel design is to develop an aircraft with the highest possible lift-to-drag ratio while being competitive with the current state-of-the-art long-haul aircraft like the Airbus A350 [6]. This objective can directly be translated to the top level requirements of the design: 361 passengers at a cruise Mach number of 0.85 with a nominal range of 14,350 km and a service ceiling of 13 km. To investigate the potential efficiency gain of the Flying V configuration, Faggiano performed a two-step multi-fidelity aerodynamic shape optimisation on the developed parametrisation [11]. A vortex lattice method was employed to explore the design space after which a genetic algorithm was used in combination with an Euler flow solver augmented with an empirical viscous drag module. This resulted in the estimate of a 25% higher aerodynamic efficiency as compared to NASA's Common Research Model (CRM) [11].

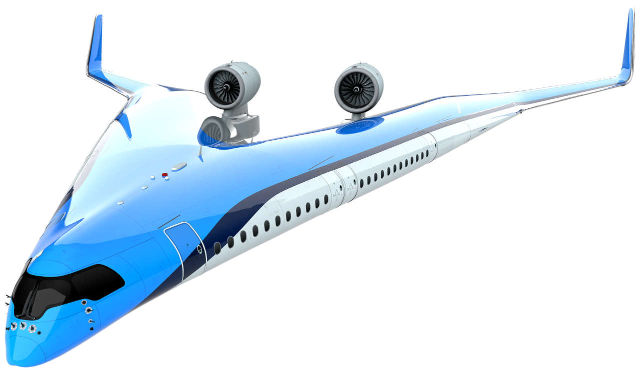

Figure 1.1: Artist impression of the Flying V aircraft.

Throughout the years, the aircraft was investigated more in depth to develop a design which satisfied constraints other than merely aerodynamic aspects. In this regard, van der Pluijm and Brouwer investigated the cockpit and centre-body fairing integration to incorporate pilot and systems integration requirements [12, 13]. Van der Pluijm devised a parametrisation for the cockpit and centre-body and subsequently utilised a similar aerodynamic model as Faggiano [12]. Brouwer took the resulting design as starting point after which an updated parametrisation was developed. Furthermore, the higher-fidelity RANS flow model was used to investigate the aerodynamic aspects of the design, resulting in a 3.3% drag reduction compared to Fagginao's centre body design [13]. Concurrently, the effect of the winglet design on lateral-directional stability and control was analysed by Horwitz. Following from the main objective of the investigation, a low-fidelity vorticity based 3D Panel method was chosen as aerodynamic model [14]. A similar approach was taken by Oosterom in devising the conceptual family design of the Flying V. A multi-objective optimisation was performed in which also the aerodynamic performance was assessed. As the main goal of the analysis was not hard aerodynamic proof, a low-fidelity panel method was used [15]. Simultaneously, Hillen developed a new parametrisation of the Flying V with the aim of making it more structurally efficient. The resulting (non-optimised) design was analysed using the aerodynamic module of Faggiano, resulting in a 13% lower lift-to-drag-ratio than the initial aerodynamically optimised design [16].

1.3. Research Scope

As the current design of the Flying V has a degraded aerodynamic performance due to the incorporation of the structurally efficient parametrisation, the full potential of the aircraft cannot be reached. This research is therefore aimed at developing an aerodynamically optimised design for the Flying V while respecting the developed structurally efficient parametrisation. The result of this study helps to progress the design process of the Flying V by ensuring that both aerodynamic and structural considerations are taken into account. A new design is proposed by performing a so-called constrained aerodynamic shape optimisation of the outer wing of the Flying V. The study is limited to the design of the outer wing as the inboard wing is driven by structural and top-level requirements rather than aerodynamic considerations. Furthermore, the aerodynamically adverse geometries resulting from the structurally efficient parametrisation are found on the outer wing.

The second goal of this study is to provide definitive proof regarding the lift-to-drag ratio of the aircraft as previous studies were based on low-fidelity aerodynamic models. This means that the focus is placed on the quality of the aerodynamic proof rather than on a highly efficient optimisation routine. Additionally, the optimisation only has to be executed a limited number of times, making it acceptable if the computational time is increased. This being the result of the optimisation only being considered at design conditions. The development of the aerodynamic shape optimisation routine can be divided into three main components: the geometry preparation, the optimisation structure, and the aerodynamic model setup. The final result of the study is the aerodynamic efficiency, in terms of lift-to-drag ratio, for the aerodynamically optimised Flying V at both design and off-design conditions. Additionally, relevant aerodynamic coefficients and flow characteristics are derived.

1.4. Research Objectives

Following the framework presented above, the main objective of this research can be formulated as follows:

> "To maximise the aerodynamic efficiency of the Flying V at its design condition by optimising the aerodynamic design of the structurally efficient parametric Flying V geometry while using suitable high-fidelity flow solvers and satisfying relevant aerodynamic constraints."

To reach the main goal of this research, several sub goals can be identified. The main focus of the study is the quality of the aerodynamic model, however an appropriate geometric model is key in accomplishing this. The first sub goal that can be identified is therefore the preparation of the geometric model. Including re-parametrisation of the current Flying V design where needed. High-fidelity aerodynamic models also require a meshed geometry to solve the underlying flow equations. The parameterised geometry coupled with a meshing tool will therefore form the second sub goal. Once the geometric model is formed, the high-fidelity aerodynamic model can be set up, forming the third goal. As the objective of this research also includes the optimisation of the aerodynamic efficiency, the following step is to set up the optimisation problem including relevant constraints. These sub-goals result in the aerodynamic shape optimisation routine needed to obtain the optimised aerodynamic efficiency of the Flying V.

1.5. Research Questions

The research objectives outlined in Section 1.4 form the basis to formulate the research questions. The main research question of this study is:

> "What is the maximal lift-to-drag ratio of the Flying V while respecting the structurally efficient parametrisation and satisfying relevant aerodynamic constraints?"

Breaking up this main question in several sub-questions simplifies the problem. The sub-questions identified are:

1. How can the limitations of the current aerodynamic design and aerodynamic model of the Flying V be resolved?
2. Which flow models and solvers are suitable to determine the aerodynamic efficiency of the Flying V?
3. How can the aerodynamic shape optimisation problem be formulated, i.e., what are the design variables involved, objective, constraints and suitable algorithms?
4. What is the impact of the relevant aerodynamic constraints on the maximal lift-to-drag ratio of the Flying V in terms of active constraints?

1.6. Report Structure

The remainder of this report answers the research questions outlined in Section 1.5. To provide the reader with sufficient knowledge about the Flying V and its design, relevant previously conducted studies are summarised in Chapter 2. The methodology used to conduct the constrained aerodynamic shape optimisation is explained in Chapter 3. This chapter discusses the three main components of geometry preparation, aerodynamic model setup and optimisation structure. Thereafter, Chapter 4 presents the verification and validation of the chosen aerodynamic model to provide confidence in the results. Chapter 5 summarises the results of the aerodynamic shape optimisation and discusses their implications. Finally, conclusions are drawn and recommendations for future work are provided in Chapters 6 and 7.

2

Flying V Background

To provide the reader with a background on the design process of the Flying V, this chapter summarises relevant previously conducted studies. The background information serves as a framework for the (design) choices made throughout this study. The discussion of previous work is divided into the three main topics of the geometric model, aerodynamic model and optimisation approach. The development of the parametrisation of the aircraft is discussed in Section 2.1, whereas the aerodynamic model used to assess the geometry is elaborated on in Section 2.2. Finally, Section 2.3 touches upon the optimisation approach used to perform the aerodynamic shape optimisations in previous work.

It is important to note that the design and analysis of the Flying V is implemented in the ParaPy environment; a Knowledge Based Engineering (KBE) Python based framework[1] which enables the automation of repetitive engineering tasks. The 3D model of the aircraft is generated by the implemented Multi-Model Generator (MMG) following a multi-level parametrisation and a small number of user defined inputs. The MMG relies on classes incorporated in the ParaPy platform to generate the geometry of the aircraft. Also several Application Programming Interfaces (APIs) are provided by ParaPy. These include an API for Salome Mesh [2], which automates the generation of unstructured meshes based on geometry built using ParaPy, and an interface with Stanford University Unstructured (SU2) [3], a software offering multi-physics simulations. The applicability within ParaPy remains an important requirement in the development of the geometric and aerodynamic model.

2.1. Geometric Model

The geometry of any object can be described by a set of parameters, the number of parameters and their function determine the flexibility of the design they represent. This makes the parametrisation of the Flying V an important aspect in its development. The initial aerodynamic design study conducted by Faggiano [11] is based on an aerodynamically favourable parametrisation. Specifically, the parameters ensure that aerodynamic shapes, such as airfoils, are simple to describe. Though, this turns out to have an adverse effect on the structural considerations as double curved surfaces arise and the aerodynamic profiles are not in-line with the structural components of the wing. To make the design structurally efficient, Hillen therefore revised the parametrisation in 2020 [16]. Section 2.1.1 describes the initial aerodynamically focused parametrisation, while section 2.1.2 touches upon the most recent parametrisation of Hillen. Additionally, the detailed winglet parametrisation is shortly discussed in Section 2.1.3.

2.1.1. Aerodynamic Parametrisation

The parametrisation of the Flying V includes both the outer mould line, as described by the planform and winglets, and the cross-section, as described by the cabin and the wing airfoils, making it a multi-level parametrisation. While the planform of the Flying V is different from conventional tube-wing aircraft, it

[1] ParaPy - Knowledge Based Engineering Platform, Retrieved on 24-08-2021. `https://www.parapy.nl/`
[2] Salome Mesh, Retrieved on 29-04-2022 from `https://docs.salome-platform.org/7/gui/SMESH/index.html`
[3] Stanford University Unstructured (SU2), Retrieved on 29-04-2022 from `https://su2code.github.io/`

can nonetheless be described by the classic parameters used in open literature [17, 18]. These include sweep angles, span, chord lengths and wing twists. This results in the design variables listed in Table 2.1, and the planform parametrisation shown in Figure 2.1 [11].

Table 2.1: Planform parameters as described by Faggiano [11].

Design Variable	Symbol	Design Variable	Symbol
Surface area	S [m^2]	Kink rel. position 1	k_2 [-]
Span	b [m]	Kink rel. position 2	k_2 [-]
Root chord	c_r [m]	Taper ratio	λ [-]
Leading edge sweep 1	Λ_1 [°]	Twist section IV	ϵ_{IV} [°]
Leading edge sweep 2	Λ_2 [°]	Twist section V	ϵ_V [°]

The planform itself can subsequently be divided into sections: section I corresponds to the root of the wing, section II is located at the so-called transition point where the cabin transitions from section 2 to 3 (shown in blue), section III corresponds to the trailing edge kink while section IV is defined by the leading edge kink, finally section V indicates the wing tip [11]. The division of these sections stems from the assumption that the wing is characterised by two kinks: a leading edge and a trailing edge kink. The streamwise orientation of the sections originates from the goal of an aerodynamically favourable parametrisation. This ensures that the parameterised cross-sections form smooth airfoils in the flow direction. Lastly, it must be noted that only the wing twist at sections IV and V, the outer wing, are design variables, as the twist of the inboard sections is dictated by the cabin design [11].

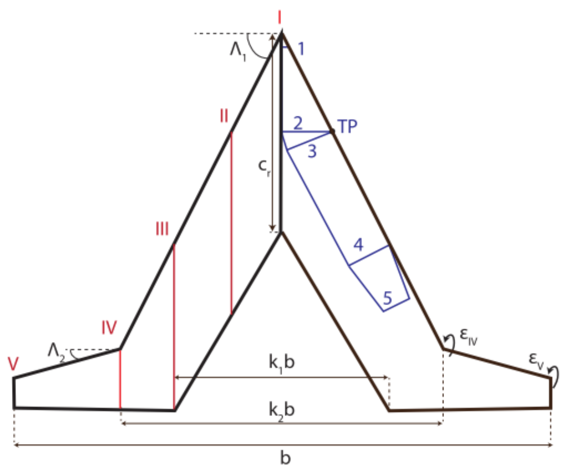

Figure 2.1: Top view of the Flying V with the cross-section profiles shown in red, and the cabin sections shown in blue [11].

The parametrisation of the inboard wing sections is driven by the design of the cabin, resulting in a reduced design flexibility. On the other hand, the outboard wing sections (IV and V) can be formed as pure airfoils as there are no limiting factors. The CST coefficients method developed by Kulfan is used to describe these outboard sections [11, 19]. The CST method describes an airfoil according to a class and shape function. The class function defines the general shape, while the shape function can modify the shape locally without changing its properties [19]. After evaluation of the method, it is determined that 12 CST coefficients per section are needed to describe an airfoil with a satisfactory error [11]. Finally, a simplified parametrisation for the winglets is used. These include the aspect ratio, leading edge sweep angle, and taper ratio. The root chord of the winglet is equal to the wing's tip chord to ensure a smooth transition. Furthermore, the cant angle of the winglet is set to zero degrees as gate requirements limit the wing span [11].

2.1.2. Structurally Efficient Parametrisation

Several studies using the aerodynamic parametrisation of Faggiano showed that the parametrisation has various pitfalls. First of all, the fuselage is too small to accommodate all payload, and the cabin protrudes the outer mould line near the outboard wing. Furthermore, the excess space between the tapered cabin section and the outer mould line, see Figure 2.1, results in a complex and structurally inefficient design [16]. Further research regarding the structural design of the aircraft showed a mismatch between the parametrisation and the location of the structural components [20, 21]. The ribs of the wing must be placed orthogonal to the leading edge to carry the loads, while the wing's profiles are described in the streamwise direction. As the ribs provide the airfoil shape, streamwise structures would be necessary to adhere to Faggiano's design, which contradicts van der Schaft's conclusions [20]. The findings underline the importance of the structurally efficient parametrisation devised by Hillen. In this approach the cabin now serves as a basis and the wing is designed around it. In other words, an inside-out approach is used.

The inside-out approach results in a detailed parametrisation for the cabin in which both the cross-sections and planform are explicitly defined instead of derived from the wing parametrisation. This approach also incorporates a constant cross-section cabin loft to allow for the Flying V family concept [15]. Furthermore, it solves the problem of the excess space between the cabin and the outer mould line by rotating the outboard cabin section by angle μ. This results in a constant leading edge sweep angle along the entire cabin length, but also in a complex torus shaped transitional loft [16]. The approach taken for the inboard airfoil parametrisation is similar to Faggiano's: the airfoil is constructed around the cabin shape. Yet, there is an important difference. Faggiano constructed the airfoil profiles in a plane parallel to the aircraft's symmetry axis, whereas Hillen proposes to place the airfoil profiles in a plane perpendicular to the cabin's centreline [16]. The position of the airfoil profiles coincides with the position of the cabin ovals such that the structural frames of the cabin can be used to create the airfoil shape. On the other hand, the outboard airfoils are described by the same CST coefficients method employed in previous parametrisation.

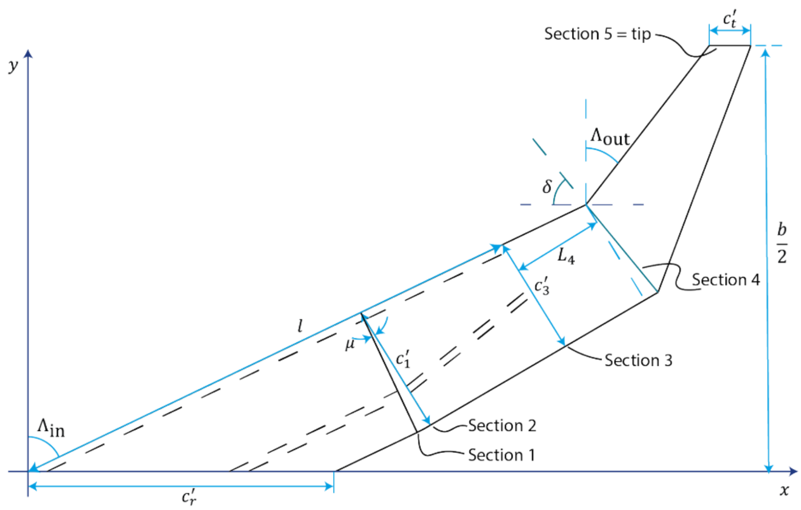

Figure 2.2: Wing planform parametrisation by Hillen with the cabin indicated by black dashed lines [16].

Another consequence of the inside-out approach is that the use of classic wing planform parameters is invalidated. Therefore the new parametrisation shown in Figure 2.2 [16] is proposed, the wing planform parameters are listed in Table 2.2 [16]. L_4 indicates the position of the leading edge kink for a given cabin length. This parameter simplifies the integration of the fuel tank as an extension of the cabin [16]. Another variable worth mentioning is the angle δ, which determines the orientation of section 4. This parameter introduces a peculiar characteristic of the parametrisation: the trailing edge possesses four distinct sweep angles. This is ascribed to sections 2 and 4 being oriented according to the angles μ and δ, introducing a new sweep angle for every linear lofted surface. This results in a non-smooth outer mould line near these sections [16].

Table 2.2: Wing planform (normalised) design variables according to Hillen [16].

Design Variable	Symbol	Design Variable	Symbol
Span	b [m]	Taper ratio	λ [-]
Normalised chord section 1	$\overline{c}_1$' [-]	Normalised LE kink position	$\overline{L}_4$ [-]
LE sweep inboard wing	Λ_{in} [°]	Normalised chord section 3	$\overline{c}_3$' [-]
LE sweep outboard wing	Λ_{out} [°]	Orientation section 4	δ [°]
Dihedral section 4	Γ_4 [°]	Dihedral section 5	Γ_5 [°]
Twist section 4	ϵ_4 [°]	Twist section 5	ϵ_5 [°]
Torus angle	μ [°]		

2.1.3. Winglet Parametrisation

In contrast to the aerodynamic parametrisation, the structurally efficient version does not include the parametrisation of the winglet. On that account, special attention to the winglet was paid by Horwitz. The goal is to design a winglet for improved lateral-directional stability and control. Initially the winglet parametrisation consisted of only three parameters and the blending of the winglet and wing tip was not considered. The parametrisation suggested by Horwitz [14] includes more variables, thereby increasing the design flexibility. The design variables include the winglet length, cant angle, leading edge sweep angle, taper ratio, blend radius and tip twist angle. It is assumed that the winglet is constructed using the same airfoil profile as the wing tip to limit the number of design variables [14]. As the winglet also functions as a rudder, it must allow for a hinged control surface. This is included in the design by placing a geometric constraint on the airfoil sections such that a straight hinge line can be constructed [14]. It is important to note that, currently, the winglet is not yet correctly sized for stability and controllability requirements. This introduces uncertainties when using Horwitz's design.

2.2. Aerodynamic Model

To assess the aerodynamic efficiency of the design, several studies analysed the parameterised geometry using flow solvers. For this, Faggiano coupled an aerodynamic analysis module to the geometry of the Flying V within the ParaPy environment. The goal of the research is to obtain the aerodynamic coefficients at cruise conditions where 3D effects, such as separation, do not come to pass. Furthermore, the aerodynamic analysis module is used in an optimisation routine, adding requirements regarding the computational efficiency of the model. These considerations lead to the selection of the Euler equations to resolve the flow around the aircraft. This flow model neglects viscous effects and heat transfer but is nonetheless capable of accurately predicting transonic flow phenomena. In particular, the transonic wave drag which is an important contributor to the overall drag in cruise [11]. The chosen flow model and the requirement of being implemented in ParaPy results in the use of the Stanford University Unstructured Code (SU2) as flow solver. SU2 is a C++ based computational analysis tool focused on Computational Fluid Dynamics (CFD) and optimisation applications [22].

While the Euler equations neglect viscous effects, the contribution to the overall drag caused by these effects cannot be neglected. To account for this, a separate viscous drag module based on empirical relations is used. The inviscid drag contributors, vortex induced drag and wave drag, are derived from SU2 and are grouped into $C_{D\text{inv}}$. The profile drag, encompassing skin friction, pressure, and lift induced profile drag, are grouped into C_{D0} and are derived from the viscous drag module. The lift induced profile drag is however neglected as its contribution can be neglected in cruise conditions [11, 23]. The remaining contributors are included according to Equation 2.1, in which C_f indicates the flat plate skin friction coefficient, f the form factor, S_{wet} the wetted surface area, and S_{ref} the reference surface area [11]. The form factor includes the effects of pressure drag due to viscous flow separation [18], and is different for every aircraft component. In the case of the Flying V, the components considered are the wing, nacelles, pylons and winglets. For each of these components Equation 2.1 is applied in which the flat plate skin friction is determined using a semi-empirical relation from Raymer, see Equation 2.2 [18]. It assumes a turbulent flow, which is deemed realistic as the cruise conditions of the Flying V are at high Mach (M) and Reynolds (Re) numbers.

$$C_{D_0} = C_f \cdot f \cdot \frac{S_{\text{wet}}}{S_{\text{ref}}} \tag{2.1}$$

$$C_F = \frac{0.455}{(log_{10}Re)^{2.58}(1 + 0.144M^2)^{0.65}} \tag{2.2}$$

However, Equation 2.2 can underestimate the skin friction coefficient if the surface is rough. To take this inaccuracy into account, the Reynolds number plugged into the equation is the smallest one between the actual Reynolds number and the cut-off Reynolds number defined by Raymer [17]. The form factor for every component is subsequently derived from relationships proposed by Torenbeek [17]. It must be noted that SU2 is not the only flow solver used in the study of Faggiano. Athena Vortex Lattice (AVL) is a vortex lattice based model [24] used for the exploration of the design space of the shape optimisation [11].

Later studies conducted by Horwitz and Oosterom employ similar lower-fidelity flow models for the aerodynamic performance evaluation. The objectives of these studies are focused on establishing the design trends and sensitivity of the objective with respect to the design variables rather than providing irrefutable aerodynamic evidence. Oosterom therefore applied AVL to obtain a computationally efficient estimation of the lift-to-drag ratio [15], whereas Horwitz used a vorticity based 3D panel method incorporated in the software FlightStream[4] to obtain stability and controllability derivatives [14].

2.3. Optimisation Approach

In previous work, several optimisation approaches were developed to optimise the design of the aircraft for a specific objective. Faggiano conducted a single disciplinary optimisation with the goal of maximising the aerodynamic efficiency of the Flying V, while Oosterom conducted a multi-disciplinary optimisation to minimise the fuel burn of the Flying V family designs. Nieuwenhuizen also conducted a multi-disciplinary optimisation of the conceptual design of the Flying V, resulting in an important conclusion about the optimisation algorithm used. The single-disciplinary optimisation approach is discussed in section 2.3.1, whereafter the multi-disciplinary optimisations are described in section 2.3.2.

2.3.1. Single-Disciplinary Optimisation

The approach taken by Faggiano to optimise the aerodynamic design of the aircraft by maximising the lift-to-drag ratio consists out of two methods. The first is a dual step optimisation in which the planform variables are optimised followed by the airfoil optimisation. The second is a single step optimisation in which the planform and airfoil parameters are optimised simultaneously. Both optimisations are driven by the Differential Evolution (DE) algorithm devised by Storn and Price [11, 25]. The algorithm is based on a direct search approach which has the ability of finding the global optimum of continuous design spaces limited by constraints. The implemented constraints relate to the pitching moment coefficient, angle of attack, passenger capacity, and thickness-to-chord ratio. The pitching moment constraint ensures that the aircraft can be trimmed with a minimum flap deflection and is statically stable, while the angle of attack constraint relates to the maximum desired angle of attack during landing when considering pilot visibility. The thickness-to-chord ratio originates from structural considerations as a thinner wing increases the weight of the structural components [11]. The objective of the optimisation is calculated every iteration using the Euler equations in combination with the empirical viscous drag module discussed in Section 2.2.

Prior to these optimisation steps, a manual multi-fidelity design space exploration enables the designer to actively adjust the parameters to optimise the design. This ensures that the initial starting point for the automated optimisations is feasible, thereby increasing the optimisation efficiency. The design space exploration consists out of a flow analysis using AVL, followed by the assessment of the lift distribution and relevant aerodynamic coefficients [11]. It is concluded that the single step optimisation is the most efficient with respect to computational time, as well as with respect to the maximum attainable objective function value. The computational time can be improved by incorporating a low-fidelity feasibility filter which checks whether a design is feasible before analysing it with the higher-fidelity flow model. It must however be noted that this approach has only been verified for the dual step optimisation [11].

[4]Research in Flight, Retrieved on 01-09-2021. `https://researchinflight.com/index.html`

2.3.2. Multi-Disciplinary Optimisation

Oosterom [15] and Nieuwenhuizen [26] on the other hand conducted a multi-disciplinary analysis within the optimisation procedure. Oosterom optimised the designs for a Flying V family concept by reducing the fuel burn. The analyses module consists of a low-fidelity aerodynamic analysis using AVL, whereafter an initial weight estimation is calculated followed by the fuel burn evaluation. The optimisation structure is divided into an inner loop, in which all analyses take place, and an outer loop which conducts the optimisation itself. The optimisation of the design takes place in two steps, first by optimising the design variables with a large impact on the fuel burn, followed by less impactful variables. The iteration between these optimisation steps is conducted manually to ensure the feasibility of the designs. The optimisation of the variables itself is controlled by the DE algorithm similar to Faggiano [15].

Nieuwenhuizen focused on optimising the conceptual design of the largest version of the Flying V. Also, in this case the fuel burn represents the objective function. The analyses module contains, similar to Oosterom, a low-fidelity aerodynamic analysis, an initial weight estimation, and a performance evaluation from which the fuel burn can be deduced. In this case however, an empirical aerodynamic model is used to reduce the computational time of this analysis step. Also, a reduced number of design variables is used to improve the computational efficiency [26]. This leads to the choice for a single step optimisation driven by the DE algorithm. After evaluation of the optimisation result, it is noticed that the optimiser does not result in the optimum point. Further research is necessary to determine the origin of this problem [26]. For the current study, this means that the results of a DE guided optimisation must be carefully examined.

3

Design Strategy & Methodology

This chapter presents the design strategy and methodology developed to optimise the outer wing of the Flying V. As established in Chapter 2, the parametric model of the aircraft is built using the ParaPy platform. The functionalities of this platform and the integration of the aerodynamic shape optimisation serve as important guidelines in the development of the methodology. The first step of the design strategy is to adjust the pre-existing parametric model to make it suitable for the optimisation process. This method is described in Section 3.1. Subsequently, Section 3.2 outlines the aerodynamic design strategy in which the geometric model is used. To conclude, Section 3.3 provides a description of the aerodynamic model on which the design strategy is based.

3.1. Geometric Model Development

The parametric model developed by Hillen [16] described in Chapter 2, serves as the starting point for the geometric model developed in this study. Due to the inside-out approach of this parametrisation, the inboard wing sections are dictated by the shape of the cabin. As mentioned in Chapter 1, the main focus of the aerodynamic shape optimisation is therefore placed on the outer wing of the aircraft. This results in the area of optimisation shown in Figure 3.1 [16]. The inboard wing extends from the root up to section 3, whereas the outer wing is defined by sections 3 up to 5. This means that section 3 is dictated by the oval shape of the cabin, whereas sections 4 and 5 are described by the CST coefficients method of Kulfan [19]. The complete wing is subsequently constructed by forming linear lofted surfaces between each section. These so-called trunks extend from one section to the next, i.e., they do not span multiple sections.

The trunk located between sections 1 and 2 represents a peculiar type of geometry. Both sections can namely possess the same leading edge point while their respective trailing edge points are separated by the angle μ. The resulting geometry is a horn torus, in which the major and minor radius are the same [16]. This horn torus causes a change in the trailing edge sweep angle such that the trunk between sections 2 and 3 is tapered. This coincides with the tapering of the cabin trunk located between those sections. Also the trunk located between sections 3 and 4 represents an unconventional loft. Section 3 is shaped by the oval cabin whereas section 4 is a pure airfoil, resulting in inherently different cross-sectional geometries. This causes the trunk connecting them to experience radical cross-sectional shape changes over a small spanwise distance. Moreover, the geometry exhibits sharp leading and trailing edge kinks as the sweep angle of the outboard wing is significantly lower than the inboard sweep angle. The trailing edge contains another curious characteristic, due to sections 2 and 4 being rotated by angles μ and δ respectively, the trailing edge contains four distinct sweep angles. This results in a non-smooth outer mould line near the transition points [16].

From an aerodynamic design and analysis perspective, the characteristics of the parametrisation are undesired. The singular leading edge point of sections 1 and 2 results in a toroidal geometry which is hard to mesh. Additionally, due to the sharp leading and trailing edge kinks, unwanted aerodynamic effects can occur leading to premature stall. The main issue of this parametrisation is however the linear

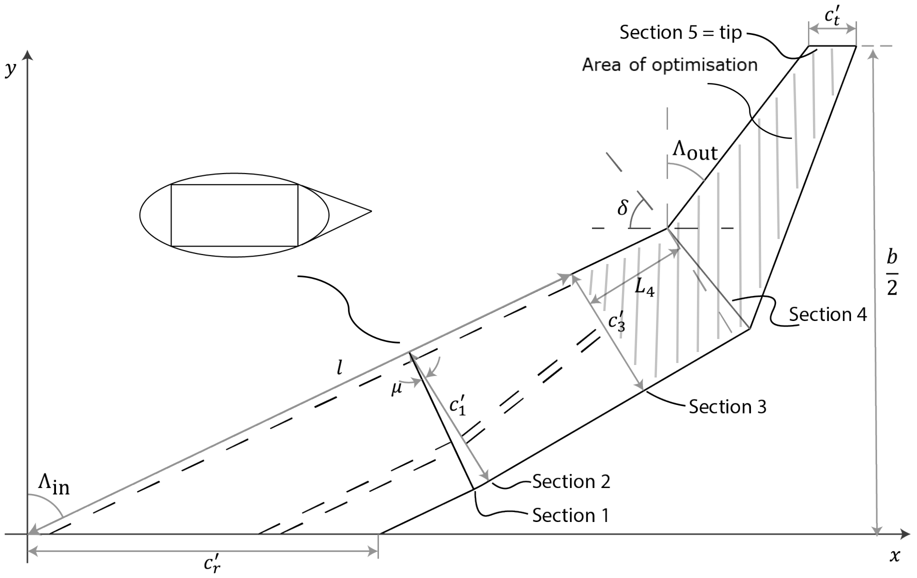

Figure 3.1: Semi-wing planform parametrisation by Hillen including the area of optimisation for the current study [16].

lofted trunk between sections 3 and 4. The cross-section of the trunk displays C0 discontinuities in the free stream direction as the cross-sectional shape change occurring in the trunk is located at an angle with respect to the flow. Hillen demonstrated that this resulted in strong shock waves over the outboard wing of the aircraft, thereby contributing significantly to the 13% efficiency loss compared to the design devised by Faggiano [16]. The goal of the geometric model developed in this study is to maintain the structural efficiency of the parametrisation, while removing its undesired aerodynamic characteristics. Section 3.1.1 further discusses the method to re-parameterise the geometry, whereafter in Section 3.1.2 an additional module to design the outboard wing control surfaces is explained.

3.1.1. Flying V Re-Parametrisation

To reach the goal of a structurally and aerodynamically efficient parametrisation, the main inside-out approach of the parametrisation must be adhered to. This means that the orientation of the wing sections cannot be changed. In particular, the sections are oriented according to the structural design of the aircraft such that the ribs can provide the airfoil shape required. Orienting them differently results in a similar mismatch between the aerodynamic and structural design as experienced by the parametrisation of Faggiano. A solution to both the structural and aerodynamic requirements imposed on the parametrisation is a new way to loft the wing trunks. The linear lofted trunks used in the model of Hillen lie at the core of the problems related to the geometry. Therefore, Gordon surfaces are used to loft the trunks instead. Gordon surfaces are based on a closed network of curves in the parametric $u-v$ space. The network of curves must contain intersection points where the curves cross each other's plane, and curves are not allowed to end in a single point. In short, all curves should end in an intersection point. An example of a valid network of curves is shown in Figure 3.2. The curves are called guides, which are indicated by $f_i(u)$, and profiles, indicated by $g_j(v)$ with i and j being the index of the respective guide and profile. The Gordon surfaces are subsequently formed using the curve network interpolation method of W.J. Gordon [27, 28]. This method involves four main steps which are visualised in Figure 3.4:

1. A skinning surface [1] $S_u(u, v)$ is created by interpolating the curves $f_i(u), \forall i$.
2. A skinning surface $S_v(u, v)$ is created by interpolating the curves $g_j(v), \forall j$.
3. A surface $T(u, v)$ is created by interpolating the intersection points of the curve network.
4. The Gordon surface is constructed following a superposition of these surfaces according to:

$$G(u, v) = S_u(u, v) + S_v(u, v) - T(u, v) \tag{3.1}$$

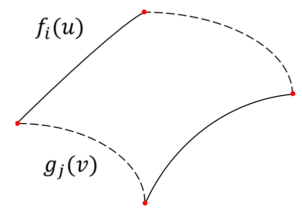

Figure 3.2: A closed network of curves.

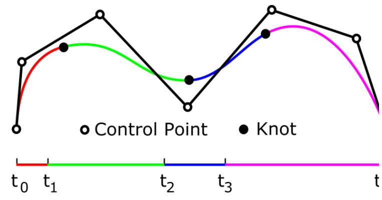

Figure 3.3: B-spline approximation [28].

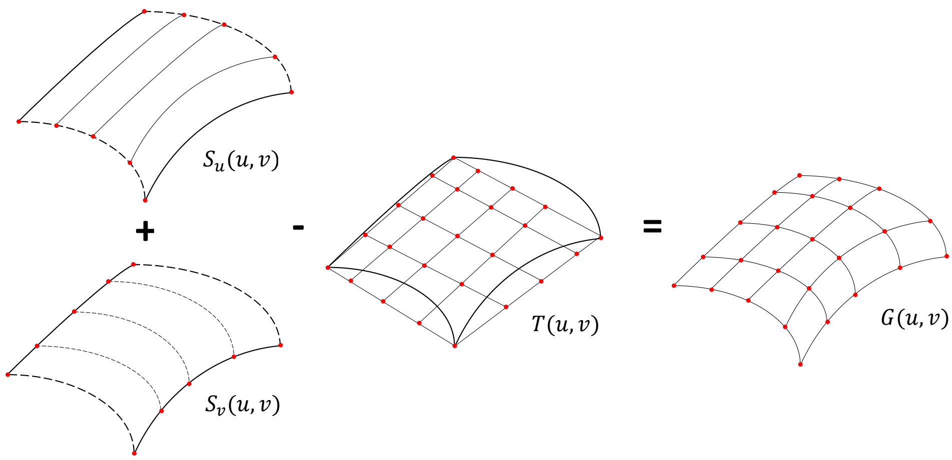

Figure 3.4: Build-up of a Gordon surface according to the superposition principle.

When considering a wing, the leading and trailing edge are represented by guides, whereas the airfoil's upper and lower curves are the profiles. In the case of the Flying V, the guides for the Gordon surfaces are based on the linear lofted geometry. By sampling the leading and trailing edge of the linear lofted trunks in the spanwise direction, sets of points representing the leading and trailing edge are formed. These sets of points function as control points for B-splines describing the leading and trailing edge of the new lofting method. This is visualised in Figure 3.5. B-splines provide more control over the sharpness of the kinks in the leading and trailing edge. This can be explained by the mathematical description of these spline curves, see Figure 3.3 [28] and Equation 3.2. $\overline{P_i^c}$ represent the control points vector, $N_i^d(u,\bar{t})$ the B-spline basis functions, and $\bar{t}$ the knot vector. The resulting B-spline $c(u)$ is closer to passing through each control point with an increasing degree of the spline, in other words, with a higher number of knots. For the trailing and leading edge of the Flying V, this means that the sharpness of the kinks can be controlled by adjusted the degree of the B-spline by which they are represented.

$$c(u) = \sum_{i=0}^{n} \overline{P_i^c} \cdot N_i^d(u,\bar{t}) \tag{3.2}$$

The Gordon surfaces lofting technique is used for sections 1 up to 5. The trunk lofted between the root and section 1 remains a linear lofted surface as this part has a constant cross-section along its length. Note that while this study is focused on optimising the outboard wing design, the inboard wing trunks running from sections 1 to 3 are also included in the updated parametrisation. The use of Gordon surfaces for these inboard trunks ensure that the toroidal geometry is removed. The complete wing outline needed to construct the Gordon surfaces is shown in Figure 3.6. The leading and trailing edge guides are shown in blue, while the airfoil profiles are shown in black. Note that the use of Gordon surfaces makes sections 2 and 4 redundant, thereby decreasing the amount of design variables without reducing the design flexibility. While the CST coefficients of section 4 can be neglected, the angle δ is still needed as it positions the trailing edge kink with respect to the leading edge kink.

[1]A skinning surface is a non-unique surface containing a set of curves.

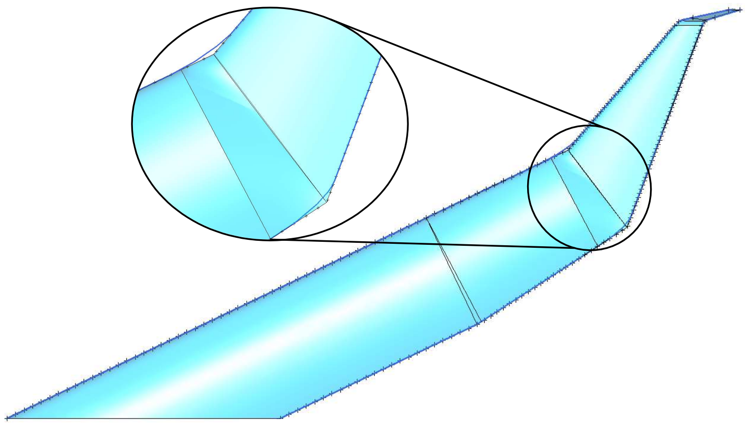

Figure 3.5: Sampling of the leading and trailing edge of the linear lofted wing, and the subsequent spline construction.

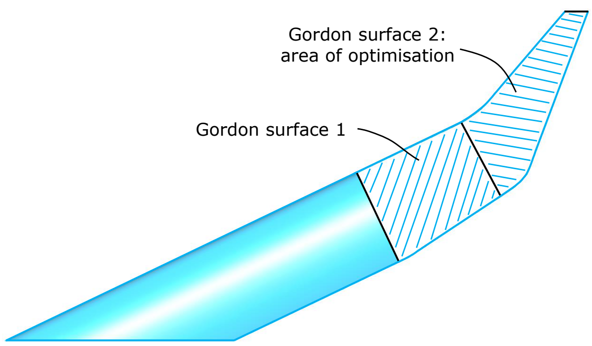

Figure 3.6: Curve network of the semi-wing planform.

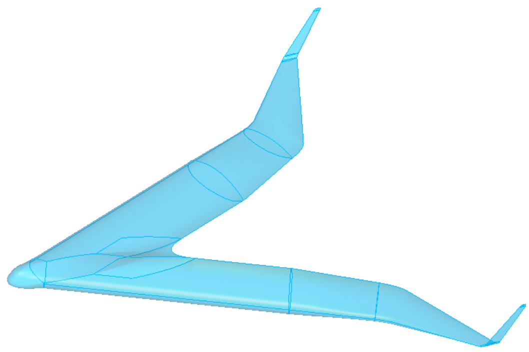

Figure 3.7: Complete Flying V geometry.

The complete geometry used in the subsequent design steps is presented in Figure 3.7. To provide a complete picture of the aerodynamic performance of the aircraft, the cockpit, centre body fairing, and winglets are included in the geometry as well. As these components and their interference effects can significantly impact the flow behaviour, they must be included in the analysis to provide definitive proof regarding the aerodynamic performance of the design. The cockpit and centre body fairing incorporated in the geometric model were devised by Brouwer [13], whereas the winglets were designed by Horwitz [14]. As mentioned in Chapter 2, the winglets are not correctly sized for stability and controllability requirements. Nonetheless, the correct size of the winglets is expected to be similar, meaning that the interaction between the winglets and the wings will not change drastically once the winglet designs are updated. The initial geometry of the complete wing is based on the design variables for the FV-1000 as found by Oosterom [15]. This study is focused on the largest version of the family as it has the most critical design in terms of aerodynamics. This is attributed to the large wetted area of the aircraft. Additionally, all Flying V family designs possess the same outer wing, hence a single design is needed to provide the complete Flying V family with an optimised outer wing.

3.1.2. Control Surface Design

To ensure the feasibility of the wing design when considering other disciplines besides aerodynamics, an additional module is created to generate the design of the outboard wing control surfaces, or elevons. The integration of the elevons can severely impact the design flexibility of the wing, neglecting them thereby means that the shape optimisation can result in designs which are unfeasible when implementing the control surfaces at a later stage. This is attributed to the requirement a control surface integration imposes on the design. The positioning of the hinge line plays a crucial role in this. An effective deflection of a control surface is only possible when the hinge line is straight and passes through the camber lines of all intermediate airfoil sections, resulting in strict constraints related to possible hinge line locations. The control surface design process is thus mainly focused around positioning the hinge line in the plane of the intermediate airfoil sections.

However, the location of the root and the tip of the control surface also have to be determined. To comply with the Flying V sub-scale test model [29], the root of the elevon is placed perpendicular to the trailing edge of the outboard wing, whereas the tip is defined as section 5 of the parametrisation. An additional constraint is imposed on the most forward x/c location of the hinge line at the tip section to ensure the effectiveness of the control surface. The maximum chord length of the control surface at the tip is limited to 35% c, which is based on the fact that the control surface effectiveness does not increase further with a larger chord length [30]. Also from a structural point of view this constraint is relevant as the torque box needed to support the winglets is positioned in front of the control surface and requires sufficient space as well. To determine feasible hinge line positions between the root and tip sections while considering the limitations, a so-called constraint satisfaction problem is set-up. The main steps of this control surface generation process are explained below, and are visualised in Figure 3.8:

1. The root and tip sections of the control surface are generated, and points along their camber lines are sampled. These represent the starting and end points of possible hinge line locations respectively.

2. Feasible hinge line locations are determined according to a constraint satisfaction problem, which states: to find a combination of starting and end points between which a straight hinge line can be formed satisfying the camber line intersection constraint. This problem is broken down as follows:

    a) For each combination of starting and end points, a straight line is drawn between them to generate a hinge line.
    b) For each hinge line location, the camber lines of the airfoil sections through which the hinge line passes are obtained.
    c) For each airfoil section, the offset δs between the hinge line and the camber line is determined in the airfoil's plane.
    d) For each hinge line location, the maximum offset between the hinge line and the camber lines is determined.
    e) For each maximum offset, the value is compared to a predetermined maximum allowed offset. If the maximum offset of a hinge line location is smaller than this value, it is considered a valid location.

3. The best location of all valid hinge line locations is qualified by the largest resulting surface area for the control surface.

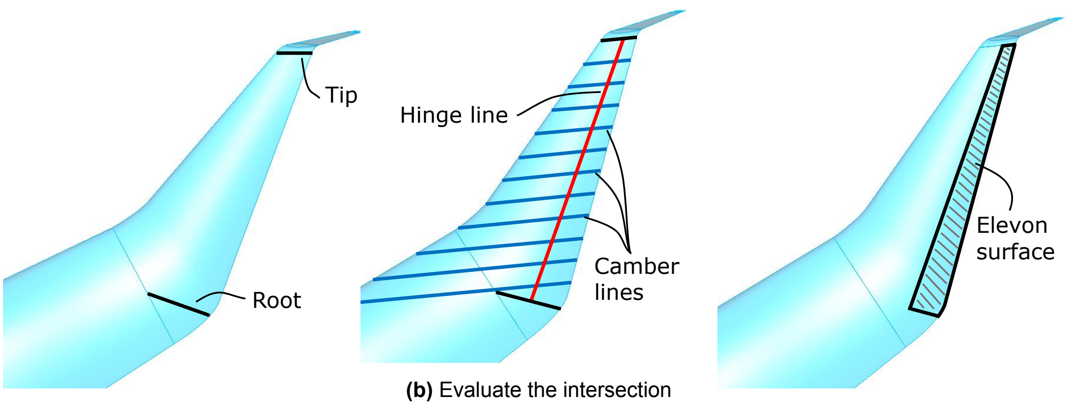

(a) Locate the root and tip sections. **(b)** Evaluate the intersection constraint. **(c)** Determine the resulting area.

Figure 3.8: Automated control surface sizing sequence (top view).

The largest resulting surface area of the control surface is a function of the maximum allowed offset between the hinge line and the camber lines. As this limit is increased, the resulting control surface area increases as well. A larger offset however results in a more ineffective deflection of the elevon. Therefore, a requirement is imposed on the minimum size of the control surface and thereby on the maximum hinge line offset. Following from the scale model used in sub-scale flight testing, the minimum control surface area of a single wing half should equal approximately 27.85 m^2 [31]. Flight tests demonstrated that this is sufficient to full fill the controllability requirements of the aircraft.

3.2. Aerodynamic Design Strategy

To revisit Chapter 1, the objective of this study is to perform a constrained aerodynamic shape optimisation of the outer wing of the Flying V to obtain the maximal lift-to-drag ratio. For this, an aerodynamic design strategy is devised. The complete strategy, including the re-parametrisation outlined in Section 3.1.1, can be divided into several steps. This process is visualised in Figure 3.9. The first step is to re-parameterise the geometry and convert the linear lofted wing into the Gordon surfaces lofted geometry. The related designs are called *linear design (0)* and *initial design (1)* respectively. The next step is to perform a low-fidelity baseline design optimisation, resulting in *baseline design (2)*. This design serves as a starting point for the higher-fidelity Free-Form Deformation (FFD) shape optimisation. This final step of the aerodynamic shape optimisation is divided into two approaches based on the integration of the elevons. Neglecting the integration of the control surfaces results in one FFD optimisation which leads to *single step design (3)*. On the other hand, including the control surface design based on the process outlined in Section 3.1.1 results in a two-step FFD optimisation. This finally leads to *dual step design (4)*. Details regarding the baseline design and FFD optimisations are explained in Sections 3.2.1 and 3.2.2 respectively.

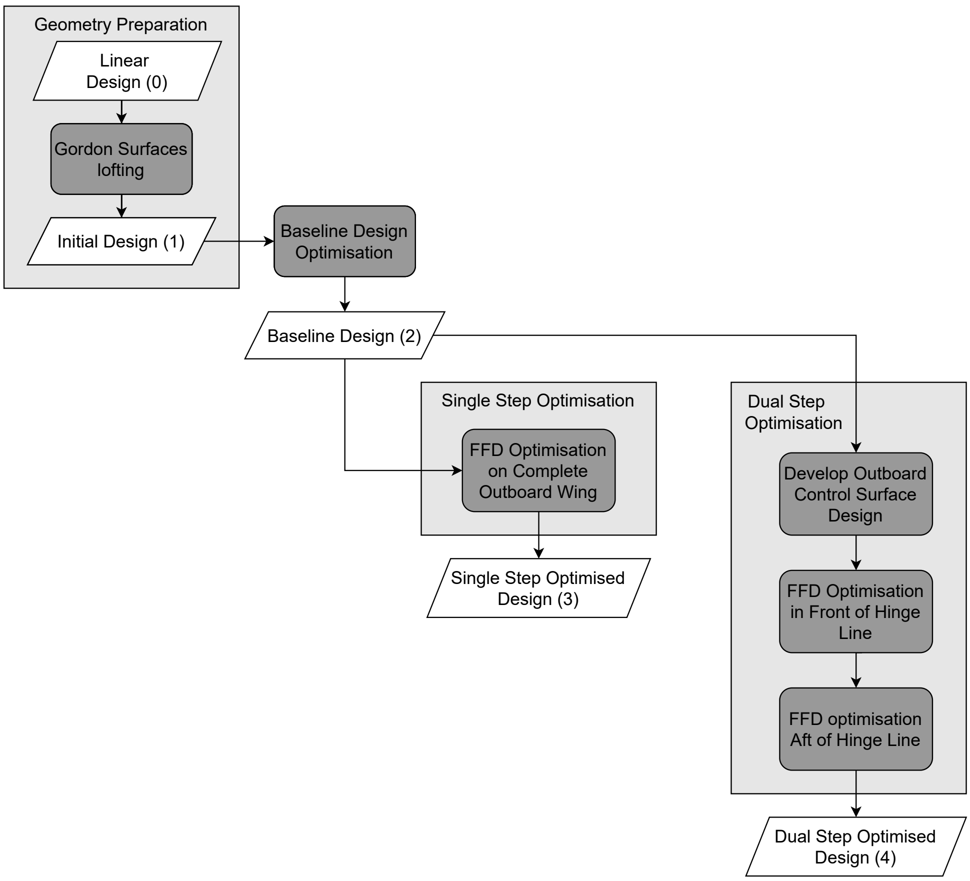

Figure 3.9: Aerodynamic design strategy of the Flying V outboard wing.

3.2.1. Baseline Design Optimisation

The baseline design optimisation is the first step of the design strategy in which the geometry is analysed and automatically optimised. It is a low-fidelity optimisation with the aim of efficiently generating a starting point for the FFD optimisation. The baseline optimisation adjusts the wing planform design variables and incorporates several predetermined design changes. Afterwards, the FFD optimisation adjusts the cross-sectional shape of the wing including relevant constraints. Providing an optimised starting point for the FFD optimisation gives rise to a reduced computational time as fewer, large, adjustments are needed. Additionally, *linear design (0)* is based on the Flying V design of Hillen, which was not optimised but solely re-parameterised. Thus, the design variable values are not adjusted to the new parametrisation resulting in possible mismatches between the geometry and structural requirements. The baseline optimisation therefore includes the necessary design changes to ensure a feasible starting point from various perspectives. The following sections discuss the baseline optimisation structure and working principles.

Optimisation Problem Setup

The baseline design optimisation workflow is visualised in Figure 3.10. It can be divided into two main steps: first an automated low-fidelity optimisation process, after which the resulting design is analysed using a higher-fidelity flow model and the control surfaces design module. In the automated optimisation process, the wing planform parameters are adjusted to obtain an elliptical lift distribution. The optimisation itself is guided by the genetic Differential Evolution algorithm, similar to earlier conducted studies related to the Flying V. The gradient-free algorithm is said to be able to find the global optimum of nonlinear and non-differentiable objective functions. Moreover, it exhibits favourable convergence behaviour and allows for parallel computing [25]. Especially the latter capability ensures that the baseline optimisation can efficiently be performed on a local notebook, thereby ensuring a quick evaluation of the starting point for the FFD optimisation. The combined characteristics of the algorithm make it particularly suitable for this type of application. The optimisation can be expressed in mathematical terms as follows:

$$\begin{aligned} \text{min} \quad & \Delta E(\overline{x}) \\ \text{s.t.} \quad & -2.5 \leq \Delta S_{\text{ref}} \leq 2.5 \\ & b \leq 32.5 \end{aligned} \tag{3.3}$$

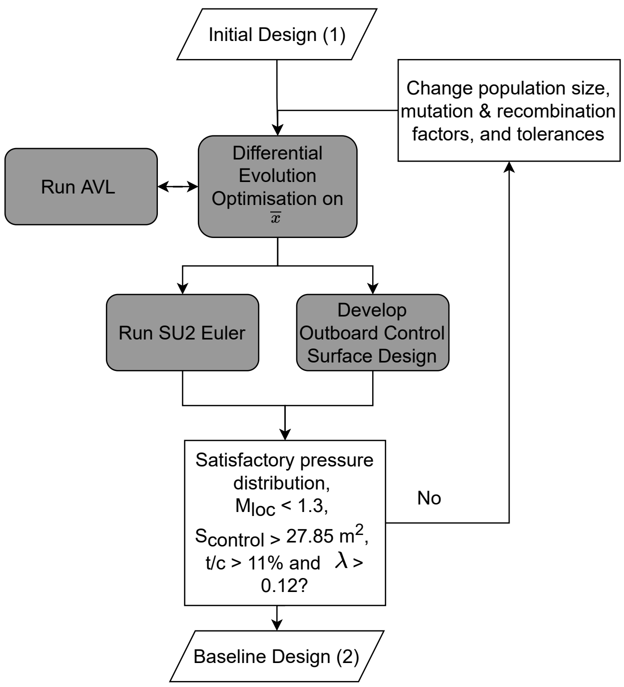

Figure 3.10: Multi-fidelity baseline design optimisation strategy.

The objective $\Delta E(\overline{x})$ indicates the difference between the actual lift distribution and a perfectly elliptical distribution. The optimisation is setup such that it minimises this difference while respecting the inequality constraints related to the reference area and the wing span. To maintain the same wing loading, which is an important factor for the low-speed requirements, the resulting change in reference area cannot be larger than 2.5 m^2. Furthermore, the semi-wing span cannot exceed 32.5 m which is based on span constraints at airport gates. The design variables used in this optimisation to reach the objective are the wing planform parameters. These include the taper ratio λ, the semi-span of the wing b, the location of the leading edge kink L_4, the outboard sweep angle Λ_{out}, the orientation of section 4 δ (which in essence positions the trailing edge kink with respect to the leading edge kink), and the tip section incidence angle ϵ_5. Especially the incidence angle of the tip section is an important variable as the wing twist is a highly efficient tool to adjust the lift distribution. The lift distribution itself is obtained using AVL which can efficiently output the force coefficients of a certain planform geometry [24]. The computational efficiency of AVL is particularly useful in the DE guided optimisation as many function evaluations are needed. Additionally, ParaPy provides an API for AVL which eases the implementation. As AVL is based on a linear vortex lattice model, the thickness of the wing is not taken into account. However, in the case of the baseline design optimisation, this limitation is considered minor as the optimisation is based on the wing planform parameters only, and the thickness profile does not vary throughout the optimisation. Therefore, the objective function only has to be sensitive to the selected design variables.

Design Evaluation
After the automated planform optimisation, the resulting design is analysed using the higher-fidelity Euler equations flow model incorporated into the SU2 flow solver [22]. It is decided to use SU2 as the flow solver due to its integration within ParaPy and its proven strength in previous studies as outlined in Chapter 2. This step is added to validate the results of the DE guided optimisation. Concurrently, the outboard control surfaces are sized to evaluate the feasibility of the design. The results of the SU2 Euler analysis and the elevon sizing are used to manually compare the design to *initial design (1)*. This comparison is based on several criteria including the strength of the shock wave if present, the maximum local Mach number, the minimum required size of the control surfaces, and the size of the tip airfoil considering structural requirements. Whenever the design is considered insufficient or unfeasible, the DE algorithm setup is adjusted by varying the population size, the mutation and recombination factors, and the tolerances. This induces new designs as the generated population and subsequent generations are constructed differently. This process is repeated until a design is deemed sufficient; this design is called *baseline design (2)*.

The aforementioned incorporated design changes relate to the structural design of the wing. Earlier studies indicated that the structural design of the wing is insufficient to efficiently carry the loads generated by the winglets [20]. The findings are based on the tip design established during the Flying V family study conducted by Oosterom [15]. This study resulted in an overall taper ratio of 0.1, and a tip airfoil with a thickness-to-chord ratio of 9.6% From an aerodynamic perspective, a low taper ratio and small thickness are desired to minimise transonic phenomena. However, it also results in a heavy tip structure to support the loads of the winglets, leading to a less feasible wing design from a structural point of view. To incorporate the structural perspective, a lower bound of 0.12 is placed on the taper ratio, while the tip airfoil is said to have a thickness-to-chord ratio of 11% in the free stream direction. These bounds are therefore included in the comparison criteria to determine whether a design is satisfactory. Note that these changes increase the thickness of the tip section by 37.5%, which in turn increases the second moment of area by 90% approximately. This latter property ensures that a lighter tip structure can be used. The baseline design optimisation therefore not only ensures that the starting point of the FFD optimisation is aerodynamically feasible but is also feasible from a structural perspective.

3.2.2. Free-Form Deformation Optimisation

While the baseline design optimisation is focused on optimising the planform of the aircraft, the next step in the aerodynamic shape optimisation is focused on adjusting the cross-sectional shape of the wing. This is done via a SU2-based Free-Form Deformation shape optimisation. The main steps of this process are visualised in Figure 3.11. The required inputs for the shape optimisation are the FFD parameterised geometry in the form of a computational mesh, the objective function $f(\overline{x})$, the constraints $g_i(\overline{x})$, and the design vector $\overline{x}$. The first iteration of the process starts with a flow analysis to determine the value of the objective function and constraints. Afterwards, the gradients for the objective $\nabla f(\overline{x})$ and constraints $\nabla g_i(\overline{x})$ are obtained in the sensitivity analysis, which is based on the continuous adjoint method. The gradients are necessary to drive the gradient-based Sequential Least Squares Programming (SLSQP) algorithm implemented in SU2. The SLSQP algorithm is particularly useful for functions and constraints which are twice continuously differentiable. However, in general it can work with any arrangement of bounds, types of constraints, and multi-variable objective functions [32]. The optimisation process is said to be converged if it meets the Karush-Kuhn-Tucker (KKT) conditions, or if the maximum number of iterations (100) is met. The KKT conditions determine whether a solution to a nonlinear optimisation problem is optimal by performing first order derivative tests. This is done by forming the Lagrangian function of the optimisation problem, including the constraints. The saddle point of this function represents the optimum for the optimisation problem at hand. A saddle point can be identified by its characteristic that all orthogonal derivatives are zero, and that it is not a local extremum [33]. The FFD technique used and the setup of the optimisation problem are discussed in the following sections.

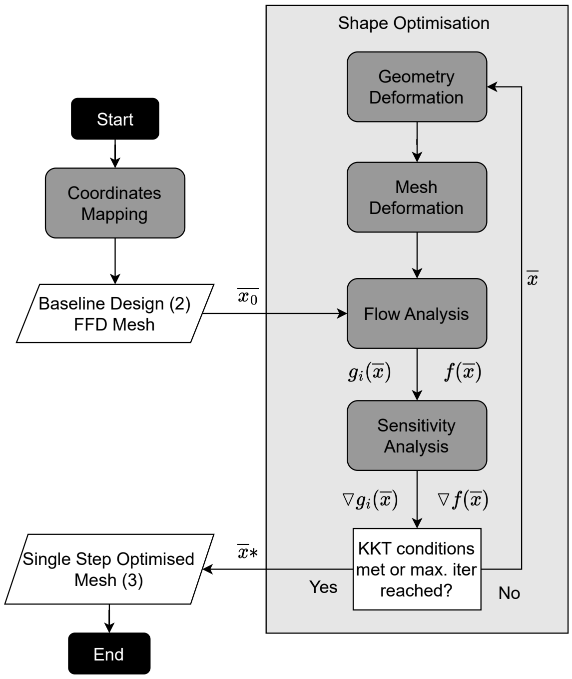

Figure 3.11: FFD gradient-based shape optimisation of SU2.

Free-Form Deformation Technique

As opposed to previous work, the developed geometric model is not used to parameterise the geometry during the optimisation. Alternatively, the Free-Form Deformation approach is used. The FFD approach represents the geometry and its deformation in an efficient way. Specifically, the deformation of the geometry instead of the geometry itself is parameterised [9]. This method increases the design flexibility of the wing compared to traditional parametrisation techniques as the geometry description is not limited to a number of parameters. Instead, the geometry is represented by a mesh and its nodes, which are subsequently deformed using the FFD technique. The FFD technique consists out of placing a so-called FFD box around the geometry that needs to be deformed. The sides and vertices of the box contain control points which represent the design variables in $\overline{x}$. The FFD box surrounding the outer wing of the Flying V is shown in Figure 3.12. Note that a FFD box is described in the parametric space, while the geometry is described by the mesh nodes in the physical space. A mapping using a trivariate tensor product Bernstein polynomial is used to relate the control points to the physical coordinates of the geometry. Bernstein polynomials have the capability of providing local control over the deformation but ensure that the continuity of the geometry is maintained [34]. To deform a geometry using the FFD technique, the following steps are taken [35]:

1. The geometry described in the physical space by the a mesh is mapped to the parametric space of the FFD box. During this mapping, the parametric coordinates of every point in the physical space are determined. This mapping only has to be performed once.
2. A perturbation is imposed on the FFD box control points leading to the deformation of the box as well as the geometry in the parametric space.
3. The new coordinates of the geometry in the physical space are determined using Bernstein polynomials and the developed mapping between the parametric and physical space.

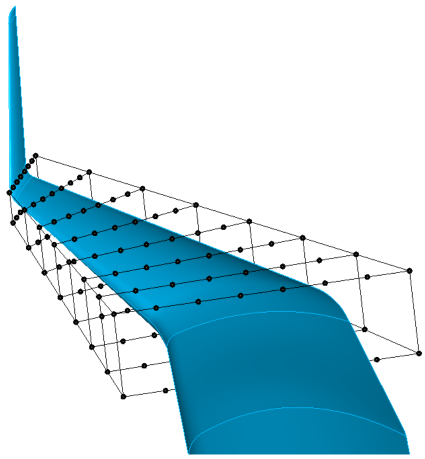

Figure 3.12: FFD box around the complete outboard wing of the Flying V.

Note that the mesh file serving as input to the FFD optimisation already includes the information on the mapping of the coordinates from the physical to the parametric space. As this mapping only has to be executed once, it is not part of the design loop. The above steps merely describe the deformation of the surface mesh based on the control points movement. However, also the volume mesh must be deformed to account for the updated surface mesh geometry. This is done in SU2 by modelling the volume mesh as an elastic solid using the equations of linear elasticity [36]. The modulus of elasticity for each volume cell can be used to control the quality of the deformation of that particular cell. In general, it is assumed that the modulus must be inversely proportional to the cell volume to preserve the mesh quality [35]. The mesh deformation approach incorporated in SU2 ensures that the geometry does not have to be re-meshed every design iteration, thereby reducing the computational time of a single iteration. It is however discovered that the method of modelling the mesh cells as an elastic solid is only robust for inviscid meshes. The method is unstable for complex viscous meshes including prism layers. These types of meshes are typically used in RANS flow analyses to capture the boundary layer effects. As a consequence, the flow analysis step in the FFD shape optimisation is performed using the inviscid Euler equations flow model. This choice ensures a high mesh quality throughout the optimisation as well as a reduced computational time as the Euler equations do not resolve the boundary layer. Though, these benefits are only valid if the initial mesh representing the starting geometry is of sufficient quality. Note that the FFD technique outlined in this section encompasses the *Coordinates Mapping*, *Geometry Deformation*, and *Mesh Deformation* steps of the FFD optimisation structure shown in Figure 3.11.

Optimisation Problem Setup

The goal of this study is to maximise the lift-to-drag ratio of the aircraft while satisfying relevant constraints. For the FFD optimisation this means that the objective can be formulated as: to minimise the drag coefficient of the design. Additionally, relevant aerodynamic and geometric constraints restrict the optimisation to ensure a feasible result. This results in the following mathematical description of the optimisation problem:

$$\begin{array}{ll} \text{min} & C_D(\overline{x}) \\ \text{s.t.} & -0.010 \leq C_m \leq 0.010 \\ & t/c_i \geq 0.11 \\ & C_L = 0.26 \end{array} \tag{3.4}$$

To minimise the drag coefficient of the design, the design variables $\overline{x}$ are represented by the control points of the FFD box. As the FFD parametrisation technique is a highly efficient method to represent a geometry and its deformation, the number of design variables can be much higher compared to a conventional parametrisation approach. Martins et al. performed several studies using the FFD technique in which the number of design variables reached over 700 [37–39], while the parametrisation of Faggiano used in the initial aerodynamic shape optimisation of the Flying V amounted to 56 variables [11]. The next aspects of the optimisation problem are the implemented aerodynamic and geometric constraints. An equality constraint is imposed on the lift coefficient to represent the design condition at which the optimisation takes place. The design lift coefficient is determined by analysing the drag polar of the FV-1000 as obtained by Oosterom [15] and amounts to C_L = 0.26. The last aerodynamic constraint imposed relates to the pitching moment coefficient around the centre of gravity. The pitching moment coefficient contributes to the trim drag experienced by the aircraft. Particularly in blended wing body aircraft the trim drag is critical as the distance between the centre of gravity and the control surfaces is less compared to a conventional aircraft. This in turn results in larger required control surface deflections causing the trim drag. For blended wing bodies and flying wings, the value for the pitching moment coefficient around the centre of gravity should remain within the bounds of -0.01 $\leq C_m \leq$ to ensure a minimised trim drag [40, 41]. In the case of the Flying V, the centre of gravity is located at 52.8% of the total aircraft length. Note that the aircraft length is measured from the aircraft's nose when the cockpit integration is neglected [42–44]. The cockpit integration causes a blunt nose such that the x = 0 point (x is in the direction of the aircraft's length, or flight direction) is located in front of the aircraft's actual nose.

A geometric constraint directly implemented into the FFD optimisation is the minimum thickness-to-chord ratio of the outboard wing sections. This minimum thickness ratio is limited to 11% to ensure a structurally feasible wing. Note that this constraint is similar to the constraint imposed on the tip airfoil in the baseline design optimisation. Additionally, a continuity constraint is imposed at the intersection of the FFD box and the existing aircraft geometry to ensure a G2 continuity level. This is not directly implemented into the optimisation problem but is controlled via the design variables, or control points of the FFD box in $\overline{x}$. A continuity constraint means that the control points near the plane where this constraint is active, are not allowed to move. Depending on the desired level of continuity, either one or two planes of control points parallel to the constrained plane must remain fixed. As the control points remain fixed, they can be removed from the design variables vector. In the case of the outboard wing optimisation, this constraint is active at the root plane (section 3), and the tip plane (section 5). Section 3 is namely limited by the oval shape of the cabin, whereas section 5 is fixed due to compliance requirements with the geometry of the adjacent winglet. The fixed planes correspond to the root and the tip of the FFD box around the outer wing, as shown in Figure 3.12.

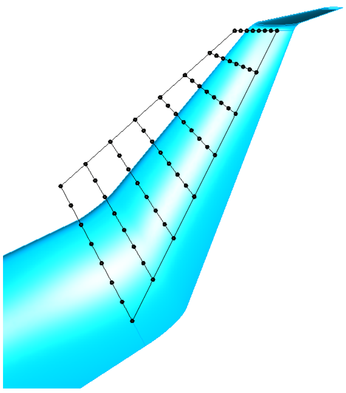

Figure 3.13: FFD box in front of the hinge line (top view).

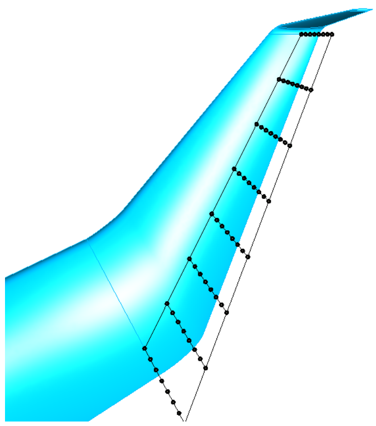

Figure 3.14: FFD box aft of the hinge line (top view).

Also the integration of the outboard control surfaces can be seen as a geometric constraint. However, this constraint is included in the optimisation via the FFD box setup and the FFD optimisation sequence, as shown in Figure 3.9. As stated in Section 3.1, a feasible control surface design is characterised by a straight hinge line which passes through the camber lines of all intermediate airfoil sections. However, using the FFD optimisation approach might prohibit forming a valid control surface design afterwards as the camber lines of the wing sections can change significantly. Therefore, a control surface design is generated for *baseline design (2)* which serves as starting point for the FFD optimisation. By imposing a continuity constraint on the plane of the hinge line, the control points are fixed and thereby the camber lines. This ensures that the control surface design remains feasible even after the optimisation. As a result, the FFD optimisation is broken into two steps: the geometry in front of the hinge line is optimised followed by the optimisation of the geometry aft of the hinge line. This means that two separate FFD boxes are needed which are positioned based on the location of the hinge line. These boxes are shown in Figures 3.13 and 3.14. This two-step FFD optimisation approach results in *dual step design (4)*. The effect of the outboard control surfaces integration is evaluated by also performing a FFD optimisation without considering the integration. This optimisation is performed in a single step using the FFD box shown in Figure 3.12, and results in *single step design (3)*.

3.3. Flow and Sensitivity Analysis Models

The aerodynamic shape optimisation outlined in Section 3.2 touches upon the flow models used during the various optimisation steps. To provide a better understanding of these models, Section 3.3.1 elaborates on their application and working principle within the framework of this research. Additionally, the flow sensitivity model used in the gradient-based FFD optimisation is outlined in Section 3.3.2. Note that this section only touches upon the working principles and application of the models, the performance of the models is subsequently investigated in Chapter 4 to confirm their validity and predictive power.

3.3.1. Flow Models

The steps of the aerodynamic shape optimisation visualised in Figure 3.9 rely on various aerodynamic flow models. Specifically, the baseline design optimisation is based on the linear vortex lattice method implemented in AVL, whereas the baseline design evaluation is based on the Euler equations model of SU2. Also the FFD optimisation relies on the Euler equations model of SU2. The fidelity of the design evaluation during the baseline optimisation is limited to an inviscid flow to ensure a quick assessment of the designs, and allow for the possibility to perform the analysis on a local notebook. Similarly, the limitations of the mesh deformation method of SU2 restrict the FFD optimisation to rely on the Euler equations as well. Considering that the objective of this study is to obtain high quality proof of the aerodynamic performance of the aircraft, an inviscid model alone is not sufficient. Therefore, the flow results of the FFD shape optimisation, belonging to *single step design (3)* and *dual step design(4)*, are augmented with the empirical viscous drag module of Faggiano [11]. This module is not used for the baseline design evaluation as the assessment criteria related to the pressure distribution and local Mach number are not affected by it. The working principles of the empirical viscous drag module are outlined in Chapter 2. In short, the viscous drag components, including the skin friction and pressure drag, are obtained using semi-empirical relations and grouped into C_{D_0}. The inviscid drag components are determined using the SU2 Euler flow analysis and are called $C_{D\text{inv}}$. The augmented lift-to-drag ratio is subsequently calculated according to Equation 3.5. The Euler flow model augmented with the empirical viscous drag module is hereafter called the Euler+ model.

$$\frac{C_L}{C_D} = \frac{C_L}{C_{D_0} + C_{D\text{inv}}} \tag{3.5}$$

Additional RANS flow analyses are performed on *linear design (0)*, *initial design (1)*, and *baseline design (2)* to provide a better insight into the drag contributions of the pressure and friction drag. The RANS equations are capable of resolving the boundary layer, thereby capturing viscous effects ignored during the Euler analyses. The flow solver SU2 also allows for flow analyses using the RANS equations. These equations use an additional turbulence model to close the system of equations needed to resolve the boundary layer. Several turbulence models are available in SU2 including the Spalart-Allmaras (SA), Spalart-Allmaras with Edwards correction (SA-E), the negative Spalart-Allmaras (SA-NEG), and the Shear Stress Transport (SST) [45, 46]. The applicability of these turbulence models is further discussed in Chapter 4. To allow for a performance comparison of all designs, *baseline design*

(2) is also analysed using the Euler+ model. This ensures a correlation between the RANS analyses and Euler+ analyses can be formed. An overview of the designs established in this study and the flow models used to evaluate their aerodynamic performance is shown in Table 3.1. Additionally, the flow and sensitivity models used in the design steps outlined in Figure 3.9 are included.

Table 3.1: Overview of the flow models used to evaluate the performance of the designs, and the flow models used in the various aerodynamic design steps.

Design	Flow Model(s)	Design Step	Flow Model(s)
Linear design (0)	SU2 - RANS	Geometry Preparation	N/A
Initial design (1)	SU2 - RANS	Baseline design Optimisation	AVL & SU2 - Euler
Baseline design (2)	SU2 - RANS	FFD shape optimisation	SU2 - Euler+
	SU2- Euler+		SU2 - Euler Continuous Adjoint
Single step design (3)	SU2 - Euler+		
Dual step design (4)	SU2 - Euler+		

Both the Euler and RANS flow analyses require a meshed computational domain. The implemented APIs for Salome Mesh and SU2 in ParaPy allow to create an unstructured mesh for the computational domain, and can create the required configuration file needed for SU2. This file contains user-specified information related to the numerical solver settings, flight and boundary conditions, convergence criteria and reference values. The computational domain used for both the Euler and RANS analyses is shown in Figure 3.15. To reduce the computational time, a half model of the aircraft is used. This is realised by imposing a symmetry condition at the symmetry plane of the domain. The free stream conditions are represented by the far field boundary condition incorporated in SU2. As suggested by Chan et al. [47] and verified in earlier conducted studies by Faggiano and Brouwer [11, 13], the far field of the domain is located 20 body lengths away from the aircraft. This distance is sufficient for the flow to recover from the effects of the aircraft such that the flow at the far field planes resembles free stream conditions.

A difference between the computational domain for an Euler analysis and a RANS analysis is found in the boundary condition imposed on the surface of the aircraft. In the case of the inviscid Euler equations, a so-called Euler wall condition is imposed. On the other hand, a RANS analysis requires an adiabatic no-slip wall condition. This is needed to capture the zero advection flow velocity near the surface. An additional difference is found in the mesh near the surface of the aircraft. As the RANS equations resolve the viscous boundary layer, a refined mesh is needed in the regions where the related viscous effects are prevalent. This results in the addition of prism layers near the aircraft's surface. An example of a (coarse) unstructured mesh including prism layers is shown in Figure 3.16. This mesh is constructed using the Salome Mesh software via the ParaPy integration.

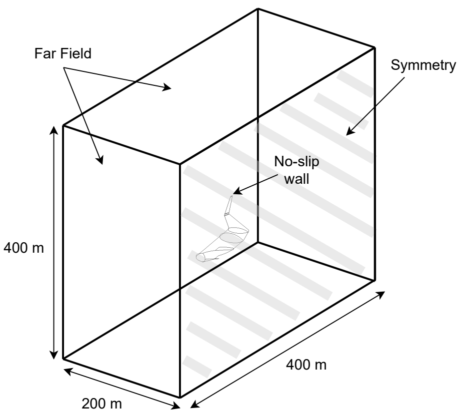

Figure 3.15: Computational domain including dimensions and boundary conditions.

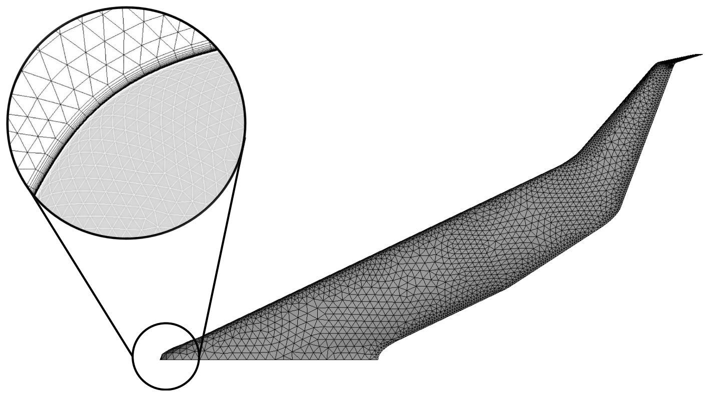

Figure 3.16: Example of a coarse mesh including prism layers for a half model of the Flying V.

3.3.2. Sensitivity Model

As the FFD optimisation relies on a gradient-based optimisation algorithm, the sensitivities, or gradients, with respect to the design variables of the objective function and constraints are needed. For this, the continuous adjoint method implemented in SU2 is used. It has the advantage that the gradient evaluation is virtually independent of the number of design variables. This is particularly advantageous for gradient-based algorithms such as the SLSQP algorithm used in this study. This characteristic also allows to benefit from the advantages of a FFD parametrisation, which results in a high number of design variables and thus provides a high degree of design flexibility throughout the optimisation. The sensitivities of both the objective function and the constraints can be computed using Equation 3.6 [22].

$$\begin{bmatrix} \frac{\partial f}{\partial x_1} \\ \frac{\partial f}{\partial x_2} \\ \vdots \\ \frac{\partial f}{\partial x_n} \end{bmatrix} = \begin{bmatrix} \frac{\partial s_1}{\partial x_1} & \cdots & \frac{\partial s_m}{\partial x_1} \\ \vdots & \ddots & \vdots \\ \frac{\partial s_1}{\partial x_n} & \cdots & \frac{\partial s_m}{\partial x_n} \end{bmatrix} \cdot \begin{bmatrix} \frac{\partial f}{\partial s_1} \\ \frac{\partial f}{\partial s_2} \\ \vdots \\ \frac{\partial f}{\partial s_m} \end{bmatrix} \tag{3.6}$$

In this equation, n represents the number of control points; m the number of surface mesh nodes in the physical space; f the function for which the gradient is sought; x_i are the design variables (i.e. control points) with $i = 1, 2, ..., n$; and s_j represent the surface normal displacements of mesh nodes $j = 1, 2, ..., m$. The gradients for every design variable $\delta f/\delta x_i$ can subsequently be computed via the dot product between the geometric sensitivities $\delta s_m/\delta x_n$ and the surface sensitivities $\delta f/\delta s_m$. The geometric sensitivities represent the change in the design variables, or control points, due to a change in the surface mesh nodes. These can be obtained using a finite difference approach. This means that the computational effort of obtaining the geometric sensitivities can essentially be neglected as they do not depend on a flow solution. On the other hand, the surface sensitivities indicate the change in f, either the objective or constraint function, due to a change in the geometry. This geometry change causes a small change in the local surface normal. The gradient is then obtained at every mesh node m via a continuous adjoint equation. The computational effort of solving this equation is equal to obtaining one flow equation [22].

4

Verification & Validation

After developing the aerodynamic design strategy, a verification and validation study is performed to evaluate the performance and the predictive power of the models used. As the underlying mesh used in the flow simulations dictates the quality of the results, a study into the mesh parameters needed to fully resolve the flow is also conducted. Establishing the correct parameters ensures that the aerodynamic performance of all designs in this study can be compared without being influenced by the quality of the computational grid. Additionally, the performance of the flow model is evaluated by comparing the results to experimental and numerical data. First, a study into the mesh density is presented in Section 4.1, after which the mesh quality is evaluated in Section 4.2. This is followed by the validation of the SU2 flow model in Section 4.3. The chapter is concluded with an assessment of the FFD optimisation approach in Section 4.4.

4.1. Mesh Convergence Study

A mesh convergence study is performed to determine the density of the computational grid needed to effectively resolve the flow phenomena. The objective of this study is to identify the size, or number of cells, of the coarsest mesh that produces reliable results. More specifically, resolving the governing aerodynamic effects is more critical during an aerodynamic shape optimisation than obtaining the exact values of the aerodynamic coefficients. The sensitivities of the aerodynamic coefficients with respect to the design variables are particularly of importance as they drive the gradient-based optimisation. The aerodynamic coefficients obtained by the viscous RANS equations are more sensitive to the mesh refinement compared to the inviscid Euler equations. This is attributed to the fact that the RANS equations resolve the boundary layer flow whereas the Euler equations neglect it. Therefore, the minimum required mesh density is investigated for the RANS flow model of SU2. Additionally, mesh convergence studies for an inviscid Euler mesh for the Flying V have already been conducted in earlier work by Faggiano and Hillen [11, 16].

The unstructured tetrahedral meshes including the prism layers for the SU2 RANS analyses are generated using Salome Mesh via the ParaPy API. Note that the prism layer parameters are not adjusted in this investigation, solely the parameters related to the triangular and tetrahedral elements are varied. This results in six computational grids with varying level of refinement. The number of 3D elements in the grids ranges from 2.1 million to 8.6 million cells. The results for the mesh convergence study are shown in Figure 4.1 and Table 4.1. Note that the relative error shown in Figure 4.1b is computed with respect to the finest grid. From Figure 4.1, it can be seen that the value for the pitching moment coefficient is especially sensitive to the mesh refinement, with a maximum relative error of 23%. On the other hand, the drag coefficient displays a maximum relative error of approximately 7% for the coarsest mesh. As the RANS equations are used to model the flow, also the pressure and friction drag components are resolved; these are collected in Table 4.1. The coarsest mesh overestimates the contribution of the pressure drag, consequently, the contribution of the friction drag component is underestimated. This behaviour is expected as the coarsest mesh is not capable of accurately resolving the viscous effects in the boundary layer contributing to C_{D_f}. Additionally, the surface elements size determines the accuracy with which the surface is modelled. The smaller the surface elements, the more accurate and smooth the geometry is represented. A coarse surface mesh in essence alters the shape of the wing, thereby affecting the resulting C_{D_p}.

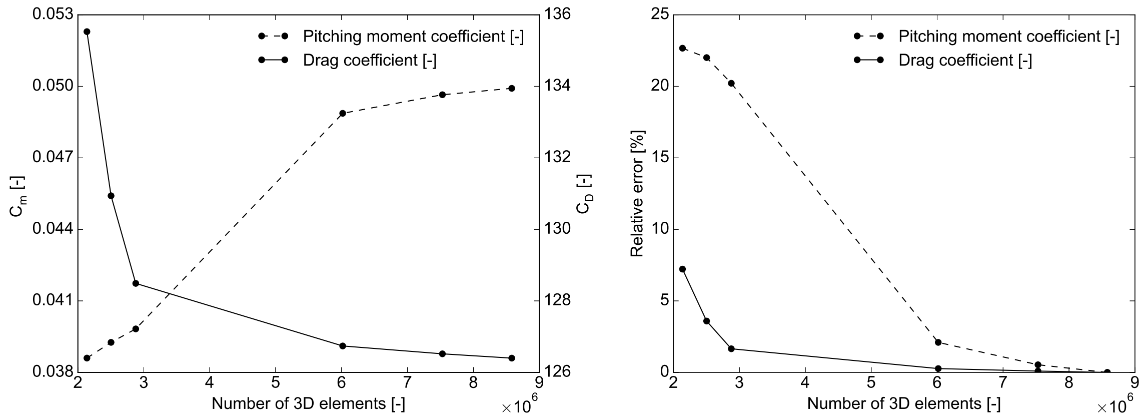

(a) Aerodynamic coefficients convergence. **(b)** Relative error w.r.t. the finest grid.

Figure 4.1: Salome Mesh grid convergence study at M = 0.85 and C_L = 0.26.

It is observed that the contribution of the drag components remains relatively stable from a mesh refinement of 6.2 million cells onwards. This corresponds to a surface mesh size of 0.125 m, whereas the mesh size at the far field planes of the domain reach 17 m. In other words, the size of the triangular surface mesh elements is 0.54% of the root chord of the (inboard) wing, while the size of the elements on the boundary planes of the domain is 3% of the total domain length. The maximum and minimum size of the tetrahedrons in the mesh are subsequently matched with the surface and far field triangular cell sizes. This mesh results in a relative error of 0.3% and 2.1% for the drag coefficient and pitching moment coefficient respectively. Increasing the mesh density further thereby increases the computational time significantly without providing notably more accurate results. As the RANS analyses are used in an optimisation process, this increased accuracy is deemed unnecessary. It is therefore determined that the grid with 6.2 million cells provides sufficient accurate results for the aerodynamic shape optimisation. This is further supported by the accepted flow errors in previously conducted optimisation studies by Faggiano and Versprille [11, 48]. The resulting mesh size is also deemed valid for the conducted Euler analyses as the results are less sensitive to the mesh refinement due to their inviscid nature.

Table 4.1: Salome Mesh grid convergence study of the drag coefficient components.

Number of 3D elements	C_D [-]	C_{D_p} [%]	C_{D_f} [%]
2.14x10^6	135.53	60.64	39.36
2.50x10^6	130.94	59.36	40.64
2.88x10^6	128.49	58.76	41.24
6.16x10^6	126.74	57.66	42.34
7.53x10^6	126.52	57.84	42.22
8.58x10^6	126.40	57.81	42.19

4.2. Mesh Quality Study

Next to the mesh refinement, also the quality of the resulting mesh is analysed. Various quality metrics are available for this based on the nature of the mesh under investigation. Section 4.2.1 discusses the quality of the prism layers in the mesh needed to resolve the boundary layer. Relevant parameters are discussed and an optimum combination is found to describe the flow with sufficient accuracy. This is followed by Section 4.2.2 in which the quality of the surface mesh is evaluated.

4.2.1. Prism Layers Quality

The most important metric to evaluate the quality of a viscous mesh is the y^+ value. This indicates the non-dimensional first layer height of the prism layers. The first layer height is measured for the first prism layer starting at the surface of the aircraft. The thickness of this layer needs to be chosen such that the viscous effects in the boundary layer are effectively captured. In this case, the corresponding value for y^+ is equal to, or less than one [47]. A y^+ value higher than one indicates that the nodes for the first prism layer are located outside of the boundary layer. This means that the velocity gradient inside the boundary cannot be captured. The y^+ value is a result of the flow analysis and can be obtained from the flow solution of SU2. This results in a trial and error approach to compute the first layer height such that satisfactory y^+ values are obtained.

Additionally, the total thickness of the prism layers as a function of the number of layers must be determined such that the complete boundary layer is captured. The order of magnitude of this thickness can be determined using the empirical relation for the turbulent boundary layer thickness along a flat plate, see Equation 4.1 [49]. A turbulent boundary layer can be assumed due to the high Reynolds number encountered in the design condition. The boundary layer thickness δ_{99} is a function of the streamwise position on the airfoil section x, and the Reynolds number Re_x where x indicates the number is based on the local characteristic length of the section. Following from the boundary layer theory, the thickest boundary layer is observed near the trailing edge of the section with the largest characteristic length, in this case the inboard wing root. Note that δ_{99} indicates that the local flow velocity measured at the edge of the boundary layer is equal to 99% of the free stream velocity [49]. This results in a first guess for the total boundary layer thickness of 0.19 m.

$$\delta_{99}(x) = 0.37 \cdot \frac{x}{Re_x^{0.2}} \tag{4.1}$$

An iterative trial and error process is subsequently conducted to establish the prism layer parameters including the first layer height, the total number of prism layers, and the growth ratio of the prism layers. The resulting meshes are evaluated according to the y^+ values and the transition of the prism layers to the triangular and tetrahedral cells. The latter transition must be smooth in order to ensure a stable flow simulation. A first layer thickness of 1.9 μm in combination with 38 prism layers with a stretch factor of 1.32 results in a mesh capable of capturing the complete boundary layer flow. The total thickness of the prism layers then amounts to 0.23 m. The y^+ distribution for this mesh is shown in Figure 4.2. It must be noted that the histogram is focused on values between 0 and 0.25 because the number of cells with a y^+ value between 0.25 and 1 is too small to be visualised. However, as seen in Figure 4.2b, y^+ values of up to 0.8 are found near the trailing edge of the winglet. This is the result of using a constant first prism layer height over the entire aircraft, in combination with the local thickness of the boundary layer. As the number of cells exhibiting a higher y^+ value is limited and still within the acceptable range of values, the mesh settings are deemed valid.

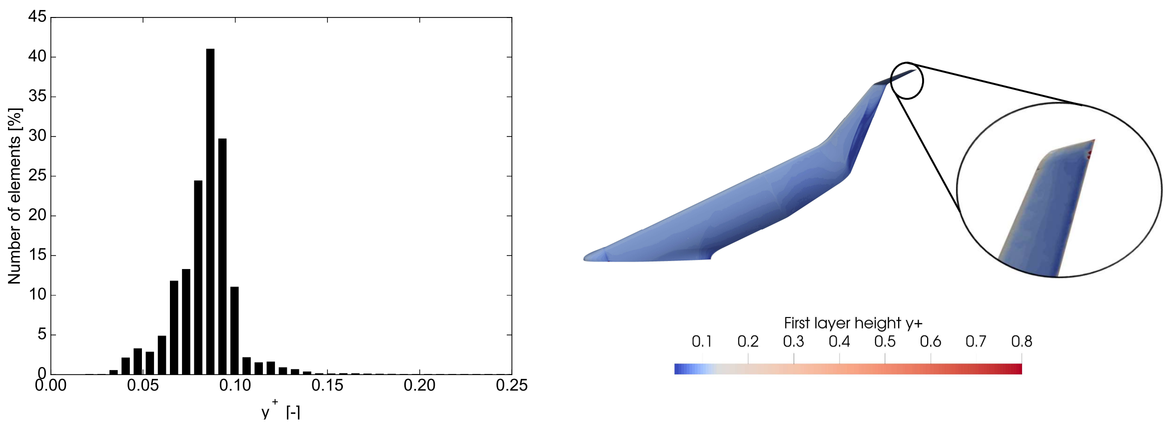

(a) First layer height distribution. **(b)** First layer height distribution on the winglet.

Figure 4.2: Salome Mesh grid quality study of the first prism layer height.

4.2.2. Surface Mesh Quality

Once the mesh refinement and prism layers settings are determined, the resulting surface mesh can be evaluated. This is done according to the skew angle and 2D aspect ratio of the cells. The skew angle is an indication of the angular quality of an element as compared to an ideally shaped equilateral triangle. A skewed triangular element is shown in Figure 4.3 [1]. The skew angle is calculated using the minimum interior angle, which is $min\{\theta_1, \theta_2\}$. Ideally, the skew angle is as close as possible to 0°. However, a range between 0°and 45°is deemed acceptable [50]. On the other hand, the 2D aspect ratio of a surface element is a measure of the conformity of the element with respect to a non-deformed and ideal version of its type, in this case an equilateral triangle. An example of the 2D aspect ratio of a triangle is shown Figure 4.4 [2]. The value of the aspect ratio can be calculated using the length ratio of the encompassing rectangle. For a high quality mesh, all aspect ratios should be close to one, however, values ranging from 1 to 5 are accepted [51]. It must be noted that the aspect ratio of a triangle can exhibit a value lower than one. In general, values above 0.2 are acceptable, while values beyond 5 are to be avoided as they can result in unstable flow simulations. Meshes with cells exhibiting aspect ratios below and above one should be avoided as this means that the cells are stretched into various directions leading to an uneven distribution of the surface mesh nodes [51].

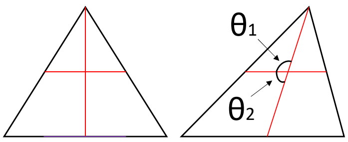

Figure 4.3: Skewness of a triangular element [1].

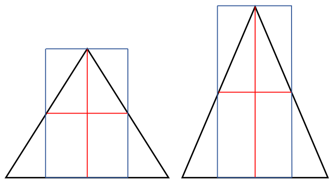

Figure 4.4: Aspect ratio of a triangular element [2].

Figure 4.5 shows the histograms for the skew angle and 2D aspect ratio of the surface mesh for the Flying V. According to Figure 4.5a, the largest skew angle present in the mesh is found to be 42°. Considering the low occurrence rate and the angle being within the acceptable bounds, this is deemed valid. This is furthermore supported by the fact that 66% of the elements exhibit a skew angle of 10°or lower. A Similar trend is observed in Figure 4.5b in which the 2D aspect ratio is shown. As the grid does not contain cells with an aspect ratio smaller and larger than 1, the most important criterion is met. Additionally, all cells possess an aspect ratio between 1 and 2, staying well below the limit of 5. Based on the surface mesh quality, the computational grid generated using Salome Mesh is deemed sufficient.

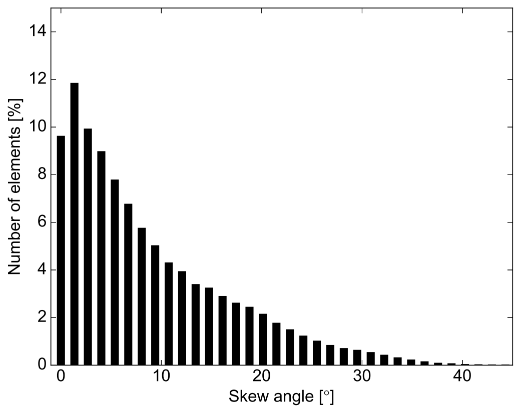

(a) Skew angle distribution.

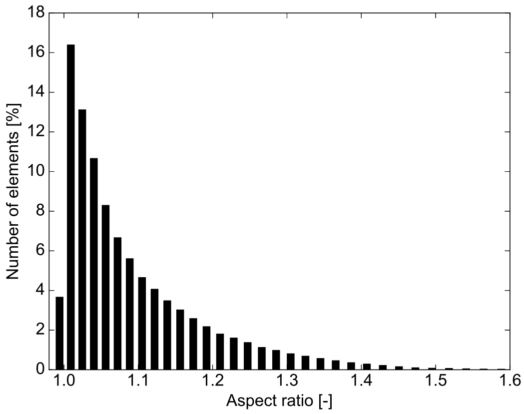

(b) 2D aspect ratio distribution.

Figure 4.5: Salome Mesh grid quality study of the surface mesh.

[1] Skewness Calculation for 2D Elements, Retrieved on 23-05-2022 from `https://www.engmorph.com/skewness-finite-elemnt`

[2] Aspect Ratio Calculation for 2D Elements, Retrieved on 23-05-2022 from `https://www.engmorph.com/2d-element-aspect-ratio-calc`

4.3. Aerodynamic Model Validation

The predictive power and validity of the flow model used to evaluate the performance of the aircraft must be established to provide confidence in the results. The SU2 model outlined in Chapters 2 and 3 is validated using experimental and numerical data for the Onera M6 wing. This model was specifically developed to serve as a validation model for CFD applications. This study focuses on the validity of the SU2 RANS model as the Euler version of SU2 has been validated by Faggiano and Hillen using a similar approach [11, 16]. Additionally, the empirical viscous drag module has been verified by Faggiano and Oosterom in their previous work [11, 15]. The validation is divided into the comparison of the data against experimental and numerical data. This is a consequence of the experimental data only containing the pressure distributions. However, as the aerodynamic shape optimisation is driven by the aerodynamic coefficients, it is important to verify these results as well. Therefore, numerical studies are used to evaluate the results obtained from the SU2 RANS model. The pressure distribution validation based on the experimental data is discussed in Section 4.3.1, whereafter the aerodynamic coefficients are compared to numerical data in Section 4.3.2.

4.3.1. Pressure Distribution Validation

The chordwise pressure distributions as predicted by SU2 are compared to experimental data from test 2308 executed by Schmitt and Charpin [52]. The analysis is conducted at a Mach number of 0.8395, an angle of attack of 3.06°, and with a Reynolds number of 11.72×10^6, corresponding to transonic conditions close to the ones experienced by the Flying V. To further ensure equivalency, the computational domain used is similar to the one visualised in Figure 3.15. The mesh itself contains 315,806 hexahedral elements and is provided by SU2 as one of the test cases. The validation of the model includes the verification of the solver settings as specified by the user in the configuration file. The numerical method used to solve the convective flow equations, as well as the turbulence model used to close the system of equations in a RANS analysis can be chosen. The numerical methods available are the Jameson Schmidt Turkel (JST) central scheme, which is stable and exhibits fast convergence behaviour, and the Roe (ROE) upwind scheme, which is more accurate for a similar mesh refinement [22]. Both numerical methods are compared to the experimental data at various spanwise locations, the most important results are presented in Figure 4.6. The complete set of pressure distributions generated for the data comparison is shown in Appendix A.

It is observed that the overall trend of the predicted pressure distributions resembles the experimental data. However, clear discrepancies can also be distinguished. The high suction peak observed in the experimental data shown in Figure 4.6a is not captured by the numerical flow simulations. Considering the that the data belongs to the most inboard wing station, wall interference effects not modelled in the simulations can explain this error. At a spanwise location of η = 0.65, a larger discrepancy between the results is observed. As can be seen in Figure 4.6b, the strength of the shock waves and pressure gradients occurring at x/c = 0.20 and 0.50 are not accurately predicted. Taking into account that the computational grid is of limited refinement, mismatches between the observed and predicted pressure gradients arise as the mesh refinement can significantly impact the accuracy of the simulations. A similar situation is observed in Figure 4.6c, where the steep adverse pressure gradient near x/c = 0.20 is not completely captured by the models. In general, the coarser the computational grid, the smaller the pressure gradient are that can be resolved accurately. This leads to underpredicted pressure gradients. While both numerical methods fail to precisely capture the flow phenomena in this study, the ROE upwind scheme does capture the upper surface shock wave better than the JST central scheme. These findings correspond to the characteristics attributed to the methods. As the convergence speed in an optimisation process is more important than providing a completely accurate flow prediction, the JST scheme is deemed sufficient for the current application.

SU2 also allows the user to specify the turbulence model used to close the system of equations. The models available within the flow solver are the Spalart-Allmaras (SA), Spalart-Allmaras with Edwards correction (SA-E), negative Spalart-Allmaras (SA-NEG), and Shear Stress Transport (SST) models [45, 46]. The results for the different turbulence models in combination with both the JST and ROE convective schemes do not show significant differences. It is therefore decided that the SA model is used in the subsequent performance evaluations. This is furthermore supported by the fact that the SA model was specifically developed for aerospace applications and shows a fast and beneficial convergence behaviour [45]. Note that the SA model is also used to construct the pressure distributions shown in Figure 4.6 and Appendix A.

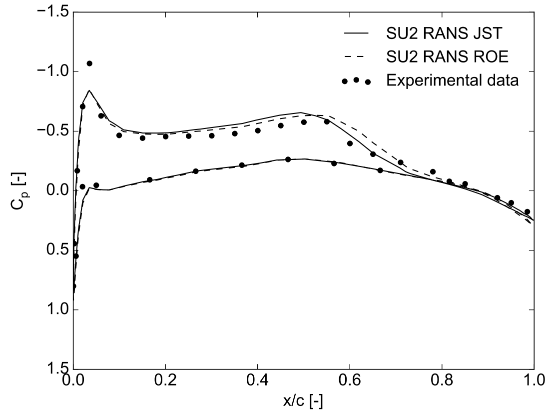

(a) η = 0.20

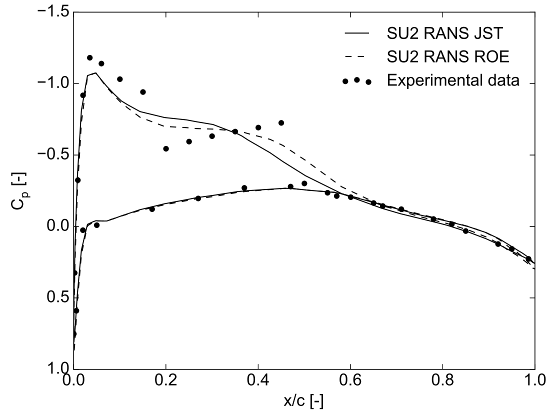

(b) η = 0.65

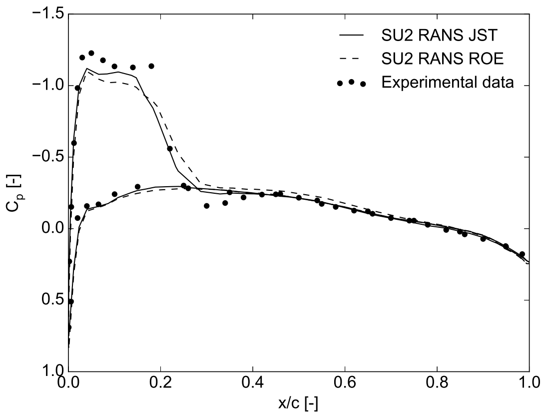

(c) η = 0.95

Figure 4.6: SU2 RANS-SA solver validation using experimental data of the Onera M6 wing test 2308 at spanwise wing stations η = 0.20, 0.65, 0.95.

4.3.2. Aerodynamic Coefficients Validation

Next to the pressure distributions, also the aerodynamic coefficients are validated as they drive the aerodynamic shape optimisation. As indicated, the experimental data of the Onera M6 wing only contains data points for the chordwise pressure distributions. Therefore, the results of several earlier conducted numerical studies regarding the Onera M6 wing are used to evaluate the performance of the SU2 RANS-SA model. The selected studies are based on RANS analyses in combination with various turbulence models to ensure the fidelity of the flow solvers is similar. It must be noted that the validation studies conducted by Araya [53], Le Moigne and Qin [54], and Nielsen and Anderson [55] do not disclose the values for all aerodynamic coefficients. Consequently, an extra study conducted by Crovato et al. [56] is added to be able to compare the pitching moment coefficient. Additionally, both the JST and ROE convective models for the SU2 RANS analyses are evaluated to determine their influence on the aerodynamic coefficients. As the performance of the turbulence models provided by SU2 is found to be comparable, solely the SA model is evaluated. The results of the validation studies and the SU2 RANS-SA analyses are shown in Table 4.2.

While the experimental data does not contain direct numbers for the aerodynamic coefficients, the experimental lift coefficient can nonetheless be obtained by integrating the wind tunnel pressure distributions along the wing. This results in the relative error between the predicted and actual lift coefficient. It can be seen that the SU2 RANS-SA solver, using both convective schemes, obtains a lift coefficient with a maximum relative error of 1.3%. This ranks the SU2 RANS-SA JST model as third most accurate followed by the ROE scheme. The latter is expected to be more accurate due to its characteristics mentioned in Section 4.3.1. The most accurate lift coefficient is found by Araya with the RANS-SA model. The level of agreement indicated by the relative error of the most accurate studies is also reflected in their resulting pressure drag coefficient. While the results of the SU2 RANS-SA and Araya's RANS-SA and k-ω simulations exhibit a maximum difference of 2 drag counts, the other studies show a discrepancy of 3 up to 6 drag counts with respect to the SU2 RANS-SA results. While the spread seems significant, all results are captured within a range of 8 drag counts which is 6% of the average pressure drag.

On the other hand, the friction drag components show a wider spread in the results. The maximum difference between the results is 9 drag counts, which is equal to approximately 17% of the average friction drag. This larger spread is ascribed to the varying levels of boundary layer mesh refinement used in the studies. The results for the friction drag can namely reflect the mesh quality as the built-up of the prism layers highly influences the accuracy with which the viscous effects are resolved. Nonetheless, the SU2 RANS-SA results are well within the range set by the earlier conducted studies, indicating that both the mesh and the solver exhibit a favourable performance. While most studies do not discuss the resulting pitching moment coefficient, Crovato et al. do. However, the value resulting from this research is 8% larger than predicted by the SU2 RANS-SA model. This large error is attributed to the low accuracy of the results of Crovato et al. as indicated by the relative error of 5.3% for the lift coefficient. While the exact number differs, the order of magnitude and the direction of the pitching moment do agree, which is the most important. To summarise, the performance of the SU2 RANS-SA models with respect to both the predicted pressure distributions and aerodynamic coefficients is deemed satisfactory. The predictive power for the coefficients is furthermore supported by the fact that it presents one of the smallest relative errors for the lift coefficient. In addition, it is found that the ROE scheme provides more accurate results, however at the cost of a higher computational time. Therefore, the JST scheme, which provides sufficient accurate results with a favourable convergence behaviour, is preferred.

Table 4.2: SU2 RANS-SA solver aerodynamic coefficients validation using numerical data of the Onera M6 wing.

	Turb. model	C_L [-]	Rel. error C_L [%]	C_{D_p} [-]	C_{D_f} [-]	C_D [-]	C_m [-]
SU2 RANS JST	SA	0.255	1.29	127	53	180	-0.181
SU2 RANS ROE	SA	0.261	1.03	126	53	179	-0.180
Araya RANS [53]	SA	0.260	0.64	127	48	175	N/A
Araya RANS [53]	k-ω	0.262	1.42	128	51	179	N/A
Araya RANS [53]	SST	0.253	2.07	132	57	189	N/A
Le Moigne & Qin RANS [54]	Baldwin-Lomax	0.270	4.52	124	50	174	N/A
Nielsen & Anderson RANS [55]	SA	0.253	2.07	N/A	N/A	168	N/A
Crovato et al. RANS [56]	SA	0.272	5.29	N/A	N/A	181	-0.196

4.4. Optimisation Module Verification

The final aspect of the aerodynamic shape optimisation that needs to be verified is the FFD optimisation method. This is done by optimising the Onera M6 wing with the objective of minimising the drag coefficient. For equivalency, similar constraints as the ones outlined in Chapter 3 are imposed. This results in a minimum thickness-to-chord ratio of 5.4% up to 7.7% for a number of predetermined wing sections. Additionally, continuity constraints are imposed on the root and tip section of the wing, as well as a fixed lift coefficient which is to be attained. The optimisation is based on a FFD box located around the entire wing, similar to the box visualised in Figure 3.12. Including the continuity constraints, this results in 198 control points, or design variables, which can be used to tweak the design. The optimisation follows the same gradient-based process as the optimisation outlined in Chapter 3, hence an Euler flow model is used. The inviscid Euler mesh for the Onera M6 wing is obtained from a test case provided by SU2. Note that the accuracy of the resulting design is limited as the optimisation is based on a relatively coarse mesh. This is because this verification step is focused on evaluating the performance and behaviour of the optimiser rather than obtaining an accurate optimum design. Following from the shape optimisation, the process converged within 23 design iterations, resulting in a drag coefficient reduction of 7.8%. The effect on the cross-sectional shape of the wing at a spanwise location of η = 0.50 is visualised in Figure 4.7. The pressure distributions on the upper surface of the wing for both the original and optimised geometry are presented in Figure 4.8.

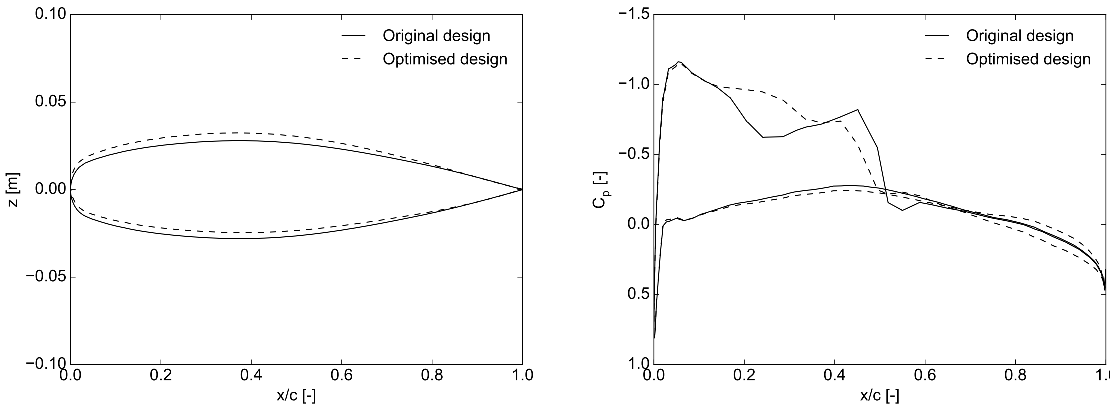

(a) Airfoil cross-section at η = 0.50 **(b)** C_p distribution at η = 0.50

Figure 4.7: SU2 optimisation verification using the Onera M6 wing: local cross-sectional shape and pressure distribution.

It can be seen that the optimisation successfully reduces the upper surface shock wave strength by adjusting the curvature profile of the wing on both the suction and pressure side. This behaviour is expected as the supervelocities, which lead to shock waves, can be controlled by adjusting the effective curvature of the airfoil. The optimisation of the Onera M6 wing thereby verifies the capabilities and working principle of a FFD-based shape optimisation. The method is able to effectively move towards an optimum design while satisfying aerodynamic and geometric constraints. Moreover, as the gradient-based optimisation shows the expected and desired behaviour, the continuous adjoint method used to obtain the gradients is verified as well. In particular, the drag coefficient decreases gradually throughout the optimisation process with a number of sudden increases as the gradient-based optimiser verifies its direction by taking a step in a different direction. Note however that a gradient-based algorithm cannot guarantee that the global optimum is found as it can get stuck in a local extremum. Nonetheless, a reduction in the drag coefficient of approximately 8% with the imposed constraints in place and with a relatively coarse mesh is deemed an acceptable result.

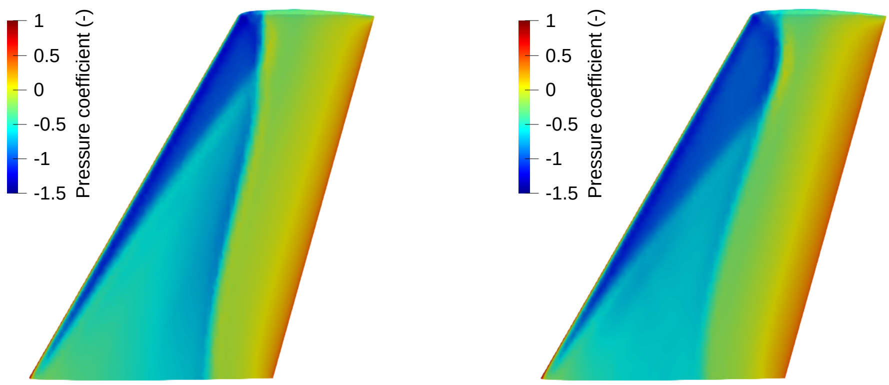

(a) Original wing design **(b)** Optimised wing design

Figure 4.8: SU2 optimisation verification using the Onera M6 wing: upper surface pressure distributions.

5 Results & Discussion

The aerodynamic shape optimisation of the Flying V outer wing is conducted after the optimisation strategy is implemented and validated. The optimisation takes place at the design point, which corresponds to the cruise conditions. As prescribed by top level requirements, the cruise conditions are dictated by a Mach number of 0.85 at an altitude of 11 km. The corresponding design lift coefficient is based on the drag polar constructed by Oosterom, and amounts to 0.26 [15]. As an equality constraint is imposed on the resulting lift coefficient, the angle of attack corresponding to the design lift coefficient is obtained through an iterative process. This makes the angle of attack an additional result of the optimisation. An initial guess must however be provided and is estimated to be 3.0°based on previous studies [11, 15, 16].

Additional flight conditions and reference values are established to fully describe the flow in the CFD analyses. The Reynolds number is an important parameter for this as it determines the flow regime in which the CFD analyses take place. In particular, either a laminar or turbulent boundary layer flow is expected depending on the value for the Reynolds number. The number is based on the Mean Aerodynamic Chord (MAC) of the aircraft $\bar{c}$, the free stream density ρ_∞ and viscosity μ_∞, as well as the cruise speed V_{cr} according to Equation 5.1. At a cruise altitude of 11 km and with a MAC of 17.7 m as obtained from the Flying V model implemented in ParaPy, the Reynolds number amounts to 1.135x10^8. Remaining relevant flight conditions and reference values needed to setup the CFD analyses are summarised in Table 5.1. Note that the location of the centre of gravity is used to evaluate the pitching moment. As described in Chapter 3, this is located at 52.8% of the total aircraft length. Additionally, the reference area of the aircraft is used to obtain the dimensionless force coefficients.

$$Re = \frac{\rho_\infty \cdot V_{cr} \cdot \bar{c}}{\mu_\infty} \tag{5.1}$$

Table 5.1: Flight conditions and reference values used in the SU2 RANS and Euler flow analyses.

Flight Conditions			Reference Values		
M	0.85	-	$\bar{c}$	17.7	m
h_{cr}	11.0	km	S_{ref}	877	m^2
Re	1.135x10^8	-	x_{cg}	30.6	m
C_L	0.26	-	T_∞	217	K
α	3.0	°	μ_∞	1.42x10^{-5}	Ns/m^2

All CFD analyses in this study are performed on a High Performance Computing (HPC) cluster as both Euler and RANS simulations are computationally demanding. This results in the ability to run the processes in parallel by being distributed over 48 to 80 cores of type AMD Opteron or Intel Xeon, which together provide at least 192 GB of memory. The gradient-based Euler shape optimisation terminates either after 100 design iterations, or when the change in the objective function between iterations is smaller than 1x10^{-5}, or when the KKT conditions are met. The Euler flow analyses themselves are terminated after 750 iterations as it is found that most flow solutions converge to a maximum root-mean-squared error of 10^{-8} for the flow properties within this number of iterations. Additionally, as the baseline optimisation is developed with the aim of being a quick evaluator of the starting point for the FFD shape optimisation, it can be performed on a local notebook. The process is in this case distributed over 8 cores of type Intel Xeon, amounting to 8 GB of memory.

This chapter presents and discusses the results of the various steps taken in the aerodynamic design process. The first step is however to evaluate the correlation between the results of the Euler+ and RANS flow models such that a comparison between the aircraft designs is possible. This is discussed in Section 5.1. Afterwards the geometry preparation design step is outlined in Section 5.2 after which the baseline optimisation is discussed in Section 5.3. The single and dual step FFD optimisations are subsequently presented in Sections 5.4 and 5.5 respectively. After establishing the designs and evaluating the effect of the design step, an overall performance comparison is made in Section 5.6. The chapter is concluded with a parameter sensitivity study shown in Section 5.7. The main results of the aerodynamic design process are summarised in Table 5.2, and Figures 5.2 and 5.3, and are discussed in the following sections. Additional pressure and friction coefficient distributions are provided in Appendix B.

Table 5.2: Aerodynamic coefficients and angle of attack for designs (0) to (4) at Re = 1.135x10^8 and M = 0.85.

Design	Flow model	C_L [-]	α [°]	C_D [-]	C_{D_p} [-]	C_{D_f} [-]	C_m [-]	C_L/C_D[-]
Linear Design (0)	RANS-SA	0.260	2.6	146	63.6	82.0	0.035	17.9
Initial Design (1)	RANS-SA	0.260	2.0	122	75.9	45.6	0.038	21.4
Baseline Design (2)	RANS-SA	0.260	2.2	136	90.3	45.9	0.044	19.1
Baseline Design (2)	Euler+	0.260	1.6	136	N/A	N/A	0.069	19.1
Single Step Design (3)	Euler+	0.260	1.2	128	N/A	N/A	0.074	20.3
Dual Step Design (4)	Euler+	0.260	1.4	134	N/A	N/A	0.071	19.4

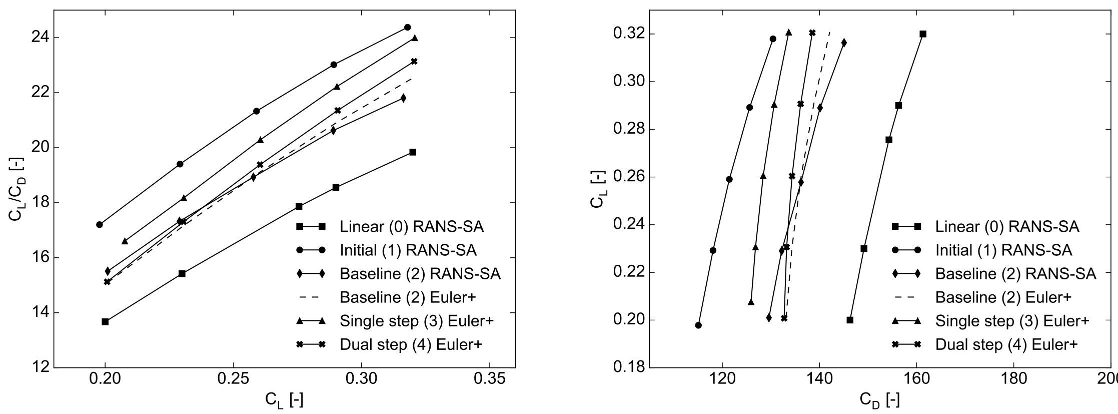

(a) Maximum C_L/C_D versus C_L **(b)** Drag polar

Figure 5.1: Aerodynamic performance of designs (0) to (4) at Re = 1.135x10^8 and M = 0.85.

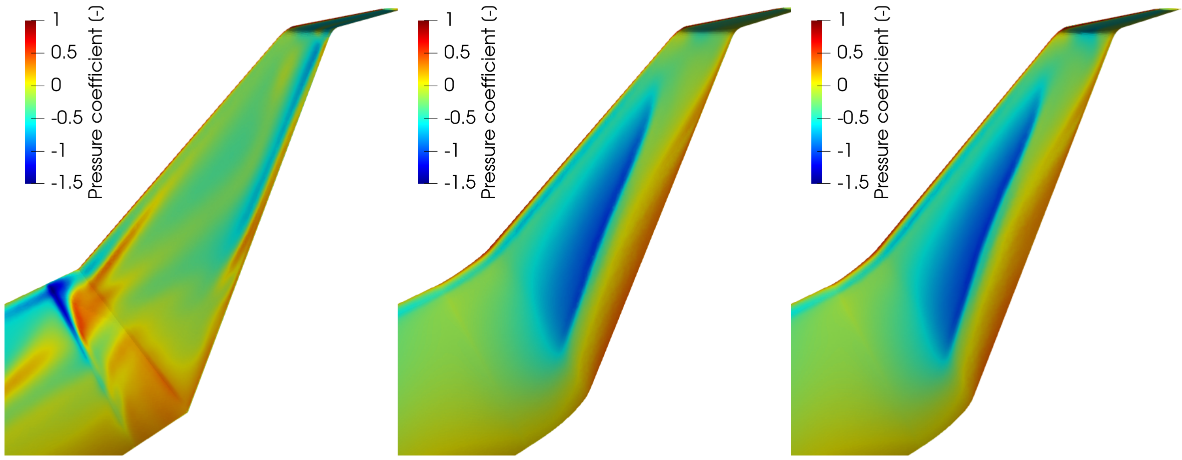

(a) Linear design (0) **(b)** Initial design (1) **(c)** Baseline design (2)

Figure 5.2: SU2 RANS-SA outer wing upper surface pressure distributions of the linear (0), initial (1) and baseline (2) designs at Re = 1.135x10^8, M = 0.85, and C_L = 0.26 with $\bar{c}$ = 17.7 m.

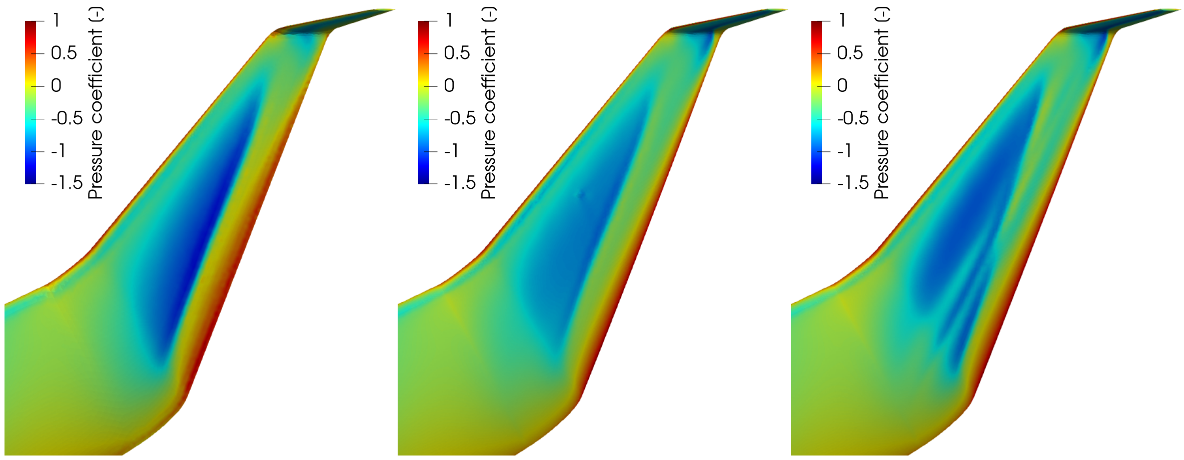

(a) Baseline design (2) **(b)** Single step design (3) **(c)** Dual step design (4)

Figure 5.3: SU2 Euler outer wing upper surface pressure distributions of the baseline (2), single (3) and dual step (4) designs at M = 0.85, and C_L = 0.26 with $\bar{c}$ = 17.7 m.

5.1. Flow Model Correlation

Two flow models are used to analyse the designs developed in this study, these are the Euler+ and RANS models as outlined in Chapter 3. To be able to compare the designs, a correlation is established between these inherently different models. This enables the resulting aerodynamic efficiency of designs (0) up to (4) to be compared while not being influenced by the nature of the flow model with which these efficiencies are obtained. The correlation is found by analysing *baseline design (2)* with both the SU2 RANS and Euler+ models. Note that various turbulence models are used during the RANS analyses to provide a better picture of the performance of the Euler+ model. The RANS analyses are augmented with the SA, SA-E, and SST models incorporated in SU2. The results for these simulations are collected in Table 5.3. To evaluate the lower-fidelity Euler+ model at off-design conditions as well, the drag polar for *baseline design (2)* is obtained using both models and is shown in Figure 5.1. In accordance with Chapter 4, Table 5.3 shows that the performance difference of the various turbulence models is negligible. The maximum difference in drag coefficient as found by the SU2 RANS analyses is 1.5 drag counts, which is equal to 1.1% of the average drag. This variation is directly linked to the resulting lift-to-drag ratio. The error for the pitching moment coefficient is with 2.3% however slightly larger. This is attributed to the fact that a deviation in a small value results in a larger relative error. In general, the variation in the SU2 RANS results is limited. Therefore, it is decided to compare the Euler+ model to the SU2 RANS-SA model as this turbulence model is used in the other analyses conducted in this study.

It is expected that the drag coefficient is underestimated as the viscous effects are taken into account via the empirical viscous drag module of Faggiano [11]. This is because the relations developed to evaluate the form factor of the various aircraft components were originally developed for a traditional tube-wing aircraft [17]. The underestimation of the drag coefficient is confirmed by the results in Table 5.3. The drag coefficient predicted by the Euler+ model is 3.9 drag counts lower compared to the SU2 RANS-SA results. This error of 2.9% is directly seen in the overestimation of the lift-to-drag ratio by the same amount. This error is however not consistent over the entire range of operating conditions as can be seen in Figure 5.1. The error between the models increases with increasing lift coefficient, while for lower lift coefficients the Euler+ model resembles the RANS-SA model more closely. This implies that the Euler+ model is not reliable for lift coefficients larger than the design lift coefficient. The reduced accuracy at higher lift coefficients can be attributed to the enhanced viscous effects occurring at higher angles of attack, which are not captured by the empirical drag module. However, as the deviation in drag coefficient at the design condition is known, the difference of 3.9 drag counts is added to the results of the Euler+ model such that they can be compared to the designs analysed by the SU2 RANS-SA model. The correction is applied to the data shown in Table 5.2 and Figure 5.1.

Next to the drag coefficient, the results for the other aerodynamic coefficients deviate as well. In case of the lift coefficient, this is reflected in the required angle of attack as found by the analyses. As shown in Table 5.3, the angle of attack is severely underestimated by the Euler+ model, meaning that the lift curve slope is overestimated. A deviation of 0.6°is observed by comparing the Euler+ and SU2 RANS-SA models. An even larger error is observed in the pitching moment coefficient, which is overestimated by 0.025 according to the Euler+ model. This amounts to more than 50% of the total pitching moment coefficient. This is a known characteristic of the Euler equations as they tend to overestimate the strength of the suction areas. The large suction area on the nose of the aircraft due to the integration of the cockpit as found by Brouwer and van der Pluijm [12, 13] therefore influences the pitching moment coefficient more in the Euler+ model. However, this overestimation of the suction strength means that the pitching moment coefficient is closer to zero than what is indicated by the model. A smaller pitching moment coefficient is desired as it brings the aircraft closer to its trim condition, hence smaller control surface deflections are needed to trim the aircraft, which reduces the trim drag. Knowing the limitations of the Euler+ model and applying the correction for the drag coefficient, the Euler+ model in general provides a good indication of the aerodynamic performance of the designs. Interpreting the results in off-design conditions and for the pitching moment coefficient should however be done with care.

Table 5.3: Aerodynamic coefficients and angle of attack of baseline design (2) for various SU2 RANS turbulence models and the Euler+ model at Re = 1.135x10^8 and M = 0.85.

Flow Model	C_L [-]	α [°]	C_D [-]	C_m [-]	C_L/C_D [-]
RANS-SA	0.26	2.2	136.2	0.044	19.08
RANS-SA-E	0.26	2.3	137.1	0.043	18.96
RANS-SST	0.26	2.1	135.6	0.044	19.17
Euler+	0.26	1.6	132.3	0.069	19.65

5.2. Geometry Preparation

The geometry is re-parameterised before the automated design process is conducted, thereby converting *linear design (0)* into *initial design (1)*. The re-parametrisation, which makes use of the new lofting technique explained in Chapter 3, alters the resulting geometry significantly. The changes in cross-sectional shape at the spanwise locations of η = 0.60 and 0.80 are visualised in Figure 5.4 in combination with the local pressure distributions. The pressure distribution on the complete upper surface of the designs is visualised in Figures 5.2a and 5.2b. From Figure 5.4a, it can be seen that the new lofting technique removes the C0 discontinuities in the streamwise direction. This is reflected by the elimination of the shock waves on the upper and lower surface at the positions where these kinks occurred. This can clearly be observed in Figures 5.2a & 5.2b in which the upper surface pressure distribution exhibits a more gradual change at the transition from the inboard to the outboard wing. The re-parametrisation also ensures that section 4 can be removed from the planform parametrisation as explained in Chapter 3. By removing this section, the transition from oval section 3 to the transonic airfoil of section 5 is more gradual as the shape change is spread out over a larger spanwise distance. The downside of this gradual change is that it results in a significantly thicker outboard wing, even at more outboard stations as seen in Figure 5.4b.

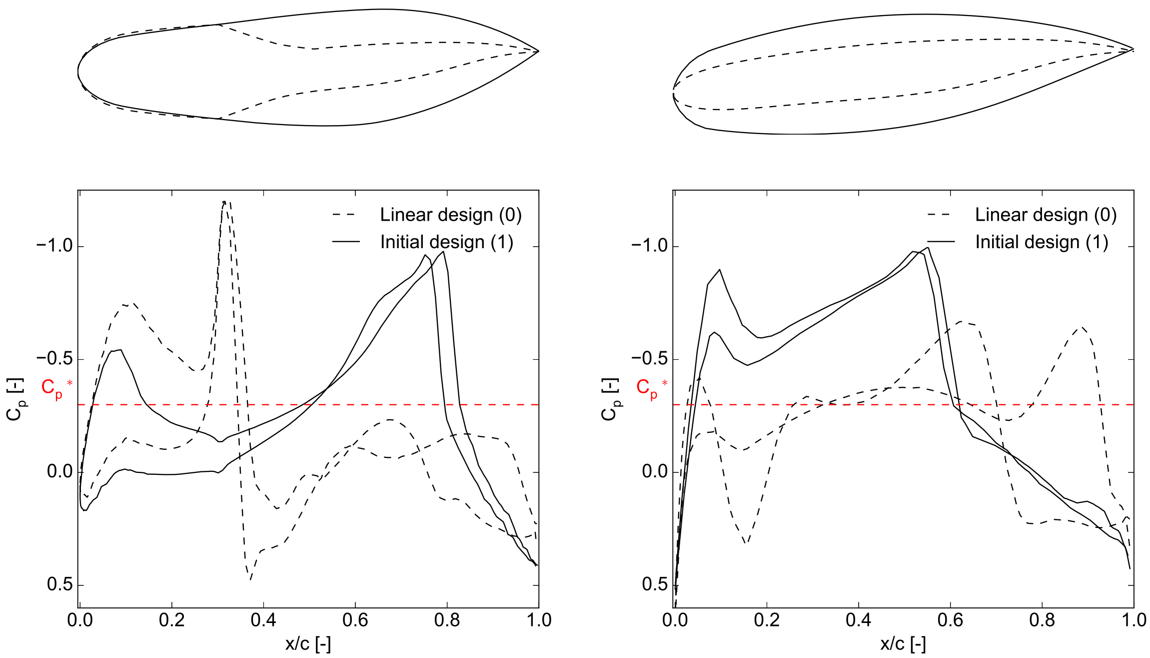

(a) η = 0.60 **(b)** η = 0.80

Figure 5.4: RANS-SA pressure coefficient and airfoil section of the linear (0) and initial (1) design at C_L = 0.26, Re = 1.135x10^8, M = 0.85 and C_p^* = -0.30.

The increased thickness of the wing is undesired when considering the transonic design conditions. This increased thickness namely results in shock waves on both the upper and lower surface of the wing, as visualised in Figures 5.2b and B.1b. As the thickness of the wing is increased, so is the resulting curvature of the streamwise airfoil sections. An increased curvature leads to higher supervelocities which in turn lead to shock waves once a critical value is reached. It must however be noted that the shock wave captured in Figure 5.4b is a normal shock wave, meaning that the Normal Shock Relations of Anderson hold [57]. Based on these relations and the Mach number found in front of the shock wave, it is expected that a lower Mach number with respect to C_p^* would be present after the shock wave, as opposed to what is estimated by the SU2 RANS-SA model. This inconsistency is ascribed to the SA turbulence model, which exhibits a reduced accuracy when shock wave-boundary layer interaction flows are present [58]. An additional factor of the increased thickness of the wing is the larger leading edge radius, which leads to a stronger suction area on the leading edge of the wing as compared to *linear design (0)*. Nonetheless, the resulting pitching moment for *initial design (1)* is increased in the nose-up direction as seen in Table 5.2. This increase is expected due to the integration of the cockpit geometry in *initial design (1)* which is not incorporated into *linear design (0)*. The cockpit geometry introduces a large suction area on the nose of the aircraft contributing to the nose-up pitching moment [12, 13]. This in turn leads to larger required control surface deflections needed to trim the aircraft, thereby increasing the trim drag.

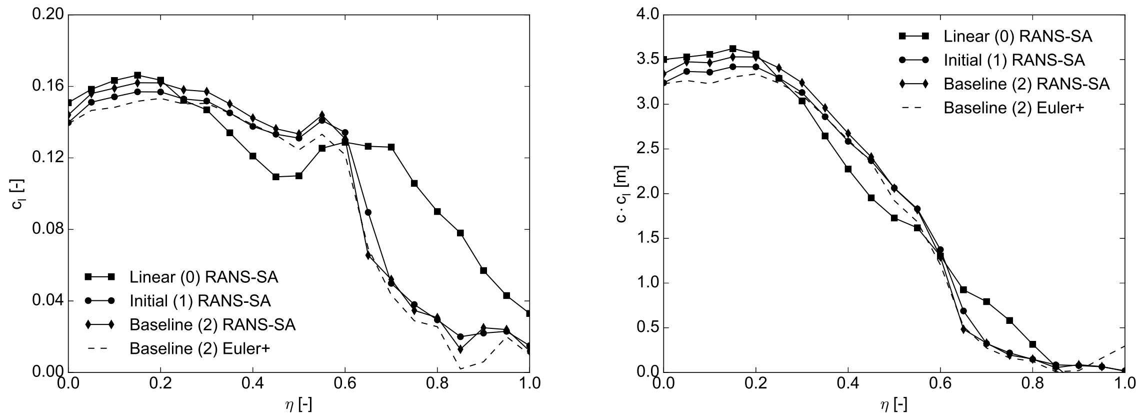

(a) Lift coefficient distribution **(b)** Lift distribution

Figure 5.5: Spanwise lift and lift coefficient distribution for the linear (0), initial (1) and baseline (2) design at C_L = 0.26, Re = 1.135x10^8 and M = 0.85.

The pressure distributions furthermore suggest that the outboard wing of *initial design (1)* is ineffective as it produces little lift. This effect is verified by analysing the spanwise lift distributions for the aircraft as visualised in Figure 5.5. The lift generated by *initial design (1)* shows a non-elliptical distribution with a drop in lift at the outboard wing. The location of the loss of lift is seen near η = 0.60, which corresponds to the thickest section of the outboard wing. *Linear design (0)* on the other hand shows a more elliptical lift distribution despite the strong shock waves occurring at the streamwise discontinuities. The difference in outboard wing efficiency is also clearly visible by comparing the sectional lift coefficient of both designs. Nevertheless, the overall aerodynamic performance of *initial design (1)* is significantly improved compared to *linear design (0)* as seen in Table 5.2. This is also reflected in Figure 5.1, in which *initial design (1)* outperforms *linear design (0)* over a wide range of operating conditions. Most importantly, the aerodynamic efficiency is increased by 19.6% at its design condition due to the new Gordon surfaces lofting technique.

As the flow model used to evaluate the aerodynamic performance of these designs is the SU2 RANS-SA model, the total drag can be divided into the pressure and friction drag components as shown in Table 5.2. It is noted that the pressure drag component increased by 12.3 drag counts after the re-parametrisation. This is attributed to the increased thickness and curvature of the wing, which makes the shock waves move aft. This aft movement increases the shocks in strength and causes additional aft suction due to the local high supervelocities. The aft movement of the shock waves is furthermore captured in Figure 5.4. Alternatively, the friction drag almost halved according to the simulation results. This change is however not realistic as the friction drag component is dependent on the wetted area of the aircraft, which is not notably altered during the re-parametrisation. Additional analyses revealed that the prism layers in the computational mesh describing *linear design (0)* are distorted. Due to the undesirable characteristics such as the sharp leading and trailing edge kinks, and the toroidal geometry, a surface mesh with a limited quality can be created. This is directly translated to the prism layers as they are built-up starting from the surface of the aircraft. These erroneous predictions are also visualised in Figure 5.6 in which the chordwise friction coefficient displays nonphysical behaviour. No further investigation is performed to solve the quality issues of the mesh as the focus of this study is not placed on *linear design (0)*.

The mesh describing *initial design (1)* on the other hand is of sufficient quality as verified in Chapter 4. Additionally, physical phenomena lie at the origin of the friction coefficient behaviour observed in Figure 5.6. At both spanwise stations, the friction coefficient remains approximately constant until the shock waves at x/c = 0.60 and 0.80 are encountered respectively. After the shock waves, the friction coefficient drops to almost zero without recovering to its original value. This behaviour can be an indication of trailing edge flow separation. This phenomena is undesired as it creates a low pressure wake behind the wing which creates additional drag.

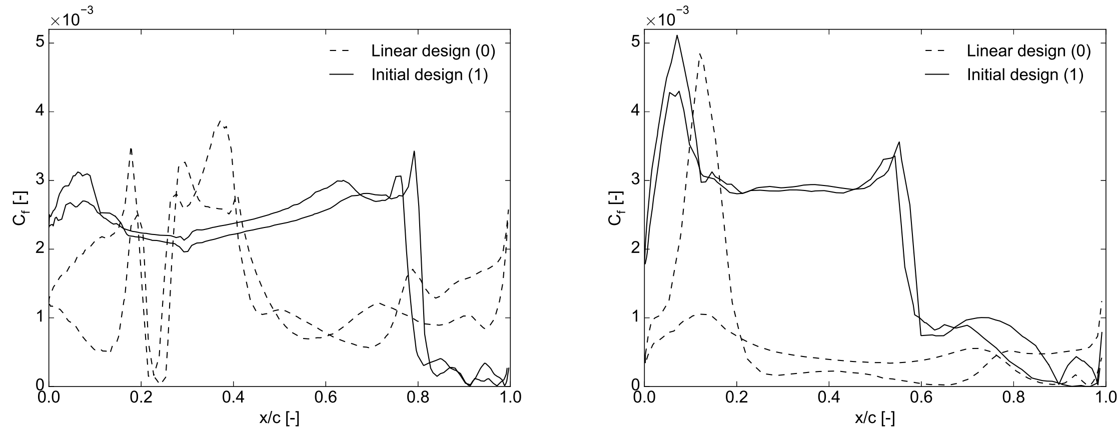

Figure 5.6: SU2 RANS-SA friction coefficient of the linear (0) and initial (1) design at C_L = 0.26, Re = 1.135x10^8 and M = 0.85.

5.3. Baseline Design Optimisation

The next step in the design process is to alter *initial design (1)* such that it can be used as a starting point for the FFD optimisation. The baseline optimisation provides an optimised planform geometry whereas the FFD optimisation is focused on the cross-sectional shape of the wing. The baseline optimisation is structured such that it efficiently moves towards *baseline design (2)* while incorporating additional design changes that are deemed necessary after evaluating results from previous studies. Most notably, a higher thickness-to-chord ratio for section 5 as well as a higher minimum taper ratio. As these changes in general oppose the design guidelines for transonic wings, it is expected that the performance of *baseline design (2)* is decreased. Specifically, these changes result in a thicker and more voluminous wing which results in stronger shock waves when considering transonic flows. The DE guided baseline optimisation does not tackle the issue of the increased thickness of the wing, but rather adjusts the spanwise lift distribution via the planform variables to enhance the efficiency of the outboard wing. To ensure a sufficiently large population size at the start of the optimisation, the number of individuals is equal to five times the number of design variables. The optimisation is terminated if the optimiser does not converge within 50 iterations. The selected design for *baseline design (2)* followed from the optimisation after 32 iterations taking 10 hours of computational time. The subsequent design evaluation is not included in this time as it is a manual process. The resulting design variables and metrics to evaluate the designs are shown in Table 5.4.

Table 5.4: Planform design variables and optimisation metrics for the initial (1) and baseline (2) design.

Parameter	Unit	Initial design (1)	Baseline design (2)
b	m	14.75	14.65
Λ_{out}	°	40.70	39.57
λ	-	0.10	0.12
L_4	m	1.50	1.18
δ	°	1.00	1.04
ϵ_5	°	-4.37	-5.48
S_{ref}	m^2	875.31	876.74
δs_{max}	cm	10.97	8.86
S_{con}	m^2	27.59	27.75

A direct consequence of the implemented design changes is seen in the value obtained for the taper ratio. This value is equal to the lower bound as dictated by the minimum required taper ratio of 0.12 to ensure a sufficiently large tip structure. The behaviour of the optimiser with respect to this design variable confirms that an increased taper ratio is not desired. To reach the objective of creating an elliptical lift distribution, the optimiser increases the negative incidence angle of the tip section. This underlines the efficiency of using the incidence angle for controlling the lift distribution. On the other hand, the lower sweep angle in combination with the change in b and L_4 are related to the constrained imposed on the reference area: a minimum change in reference area must be observed while incorporating the design changes. This results in a reference area increase of 1.4 m^2 for *baseline design (2)*. This relative change of 0.16% ensures that the wing loading for both designs is the same, thereby maintaining similar low speed characteristics.

To furthermore ensure a feasible design is selected for *baseline design (2)*, the outboard control surfaces are sized. As discussed in Chapter 3, the approximate minimum required area for the control surface is obtained from the sub-scale flight model and yields 27.85 m^2 [31]. It is however observed that, in general, the resulting control surface area increases when the maximum allowed offset between the hinge line and camber lines increases as well. As an increased offset leads to a more inefficient deflection of the surfaces, a balance must be found between the allowed offset and the resulting control surface area. This yields the results presented in Table 5.4 and Figure 5.7. It is seen that *baseline design (2)* is able to provide a larger control surface area with a smaller maximum offset, in which the maximum offset is found in close proximity to the point where the leading edge changes in sweep angle. This is attributed to the complex geometry in this area, therefore a rapid change in the location of the camber lines is observed which a straight hinge line cannot follow.

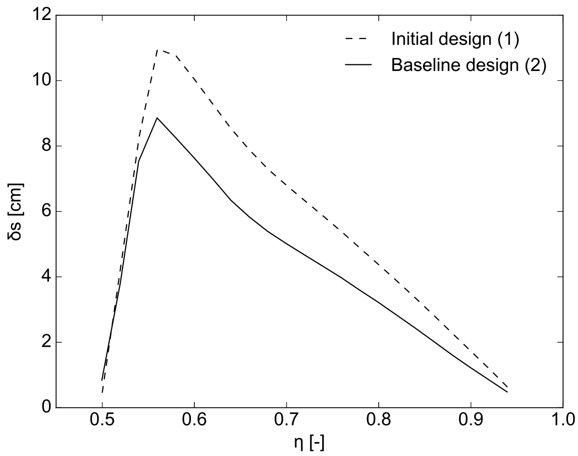

Figure 5.7: Hinge line offset w.r.t. the camber line at various spanwise locations for the initial (1) and baseline (2) design.

While *baseline design (2)* outperforms *initial design (1)* on the feasibility aspect due to the integrated design changes and a better control surface design, it falls short with respect to the aerodynamic performance. As seen in Table 5.2, the aerodynamic efficiency is decreased by 10.7% at its design condition, while a similar decrease is observed over a wider range of operating conditions in Figure 5.1. The decrease in lift-to-drag ratio is caused by the increase in pressure drag of 14.4 drag counts, which in turn is the result of stronger shock waves extending more outboard. This is visualised in Figures 5.2 and 5.8. The strength and extend of the shock waves is increased due to the incorporated design changes which result in a thicker wing with a higher curvature. The higher curvature increases the supervelocities and thereby the shock wave strength. Particularly the outboard sections of the wing suffer from an increased shock wave strength as seen in Figure 5.8b. The effects of the design changes are more pronounced there as the tip airfoil of section 5 exhibits an increase in thickness of 37.5%.

The effect of the stronger shock waves is also represented by the behaviour of the friction coefficient as visualised in Figure 5.9. The friction coefficient approaches closer to zero after the shock wave for *baseline design (2)*, indicating a higher chance of trailing edge flow separation. Also the resulting friction drag component increased in magnitude by 0.65%. This small increase is attributed to the increase in wetted area by the same order of magnitude. The effect of the optimisation can also be observed in Figure 5.5. While the objective of the optimisation is to enhance the elliptical lift distribution, *baseline*

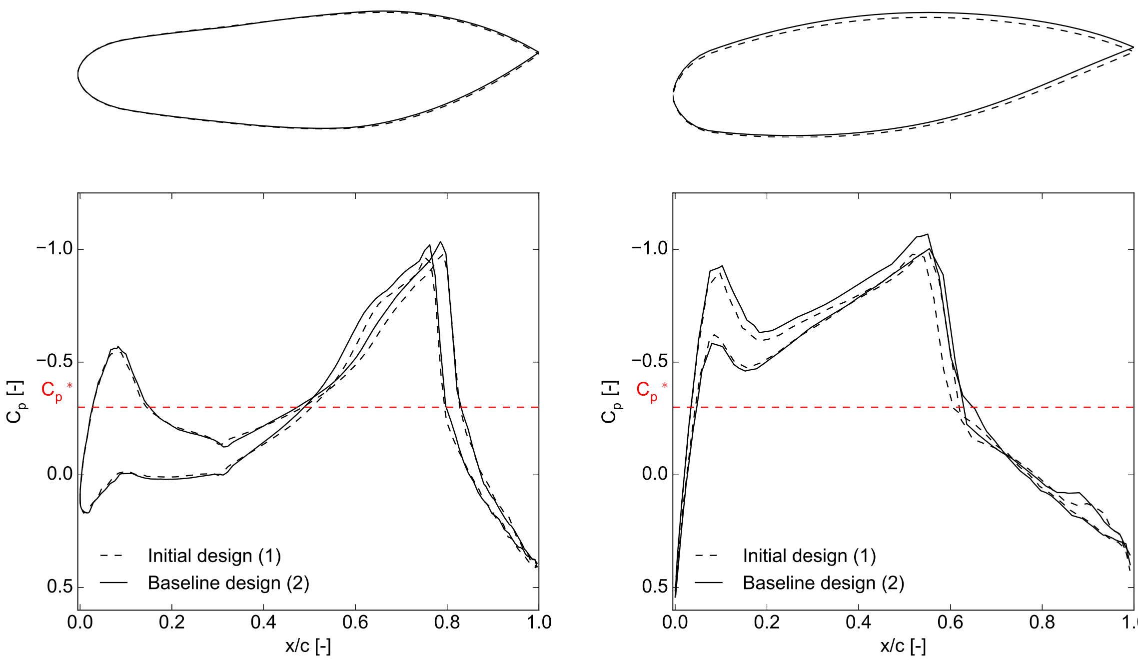

(a) η = 0.60 **(b)** η = 0.80

Figure 5.8: SU2 RANS-SA pressure coefficient and airfoil section of the initial (1) and baseline (2) design at C_L = 0.26, Re = 1.135x10^8, M = 0.85, and C_p^* = -0.30.

design (2) does not present a more efficient outboard wing than *initial design (1)*. The adverse effects of the incorporated design changes pose a significant challenge for the optimiser to overcome, thereby not resulting in an improved design compared to *initial design (1)*. All in all, *baseline design (2)* exhibits an inferior aerodynamic efficiency due to the increased thickness of the wing leading to an increase in the pressure drag of almost 19%. Nonetheless, the feasibility level of the design is improved due to the incorporated design changes and the more favourable control surface design with a maximum hinge line offset of 8.9 cm.

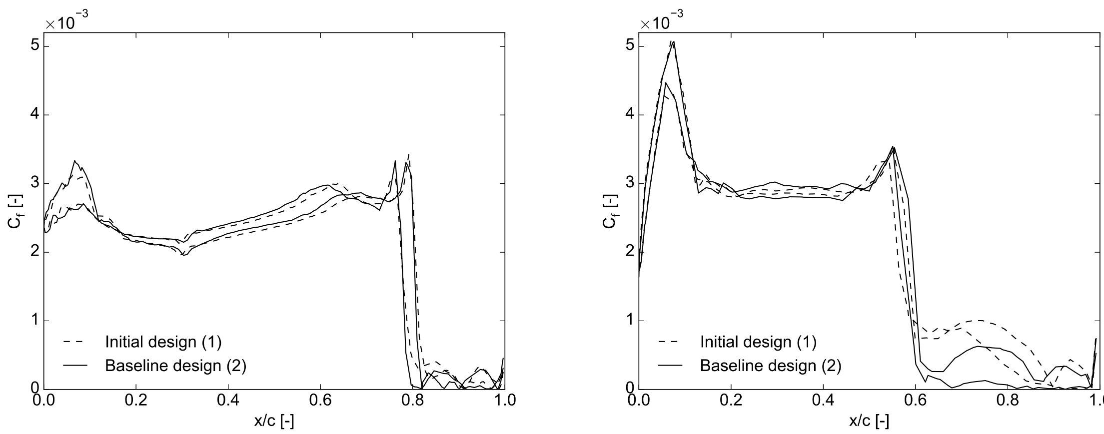

(a) η = 0.60 **(b)** η = 0.80

Figure 5.9: SU2 RANS-SA friction coefficient of the initial (1) and baseline (2) design at C_L = 0.26, Re = 1.135x10^8 and M = 0.85.

5.4. Single Step Optimisation

The next step of the design process is the FFD optimisation, which is focused on the cross-sectional shape of wing rather than the planform design. The objective of the FFD optimisation is to increase the lift-to-drag ratio which is degraded due to the incorporated design changes outlined in Section 5.3. As the integration of the control surfaces is neglected in this optimisation approach, the process consists of one step. This transforms *baseline design (2)* into *single step design (3)*. The ignored control surface integration is also represented by the constraints implemented during this optimisation. Solely continuity constraints on the root and tip section of the outboard wing are imposed, hence the control points in these, and the adjacent planes, are not allowed to move. The total number of control points needed to describe the FFD box is then a trade-off between the design flexibility and the computational effort. Based on earlier conducted studies [37–39], the FFD box in this study consists out of 12 control points in both the x (chordwise) and y (spanwise) direction, and 2 in the z direction. Including the continuity constraints, this yields a total of 240 design variables. The optimisation resulted in *single step design (3)* after 22 design iterations taking 6.5 hours in total.

Single step design (3) presents a lift-to-drag ratio of 20.3 which is an increase of 6.3% compared to *baseline design (2)* as analysed by the augmented Euler+ model. The complete overview of the aerodynamic performance of the design is shown in Table 5.2 and Figure 5.1. The increased aerodynamic performance also affects the angle of attack in cruise which reduced from 1.6°for *baseline design (2)* to 1.2°for *single step design (3)*. Note however that the Euler+ model severely underestimates the angle of attack as compared to the SU2 RANS-SA model which predicts a cruise angle of attack of 2.2°for *baseline design (2)*. Nonetheless, it can be safely assumed that the FFD optimisation results in a decrease in the required angle of attack of an equivalent magnitude. A lower angle during cruise is desired as this means that a lower angle of attack can be attained during landing. This results in a shorter landing gear length to avoid a wing strike, thereby reducing the weight of the aircraft.

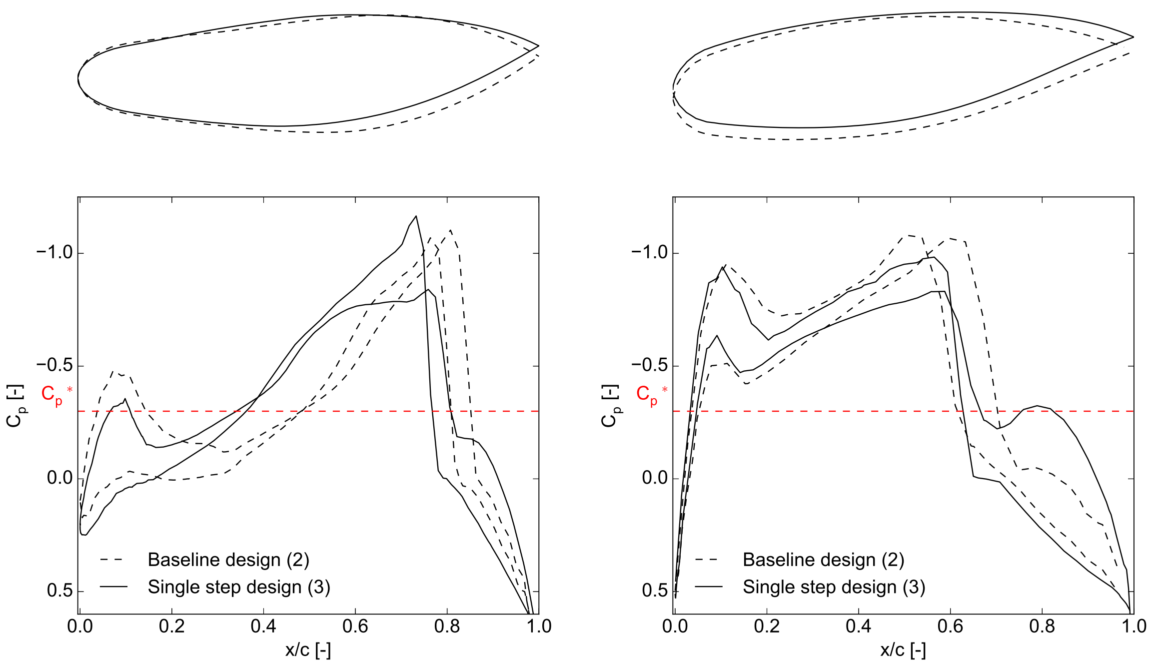

(a) η = 0.60 **(b)** η = 0.80

Figure 5.10: SU2 Euler pressure coefficient and airfoil section of the baseline (2) and single step (3) design at C_L = 0.26, M = 0.85, and C_p^* = -0.30.

The improvement in the overall aerodynamic performance of the design is ascribed to the reduction in shock wave strength as clearly visualised in Figure 5.3 and 5.10. The curvature of the upper surface is reduced such that lower supervelocities occur, thereby reducing the shock wave strength. This can be seen in the chordwise pressure distributions at x/c = 0.78 and x/c = 0.60 for η = 0.60 and η = 0.80 respectively. An adverse effect of the decrease in shock strength is the increase in the nose-up pitching moment as seen in Table 5. Also for the pitching moment coefficient, the results for the Euler+ model are not completely accurate as they are overestimated compared to the SU2 RANS-SA model. Nonetheless, the increasing trend is valid and is caused by the reduced shock wave strength on the outboard wing, which makes the suction area on the nose of the aircraft relatively stronger. This behaviour causes an increase in trim drag as the control surfaces need to have a larger deflection to counteract this nose-up tendency. On the other hand, the shock wave on the lower surface of the wing increased in strength, specifically in the inboard wing sections as observed in Figure B.2. Additionally, it shows that a lambda shock is present on the lower surface, which is seen in Figure 5.10b at x/c = 0.60 and 0.80. Also an increase in the tip shock strength is presented in Figure 5.3. This is the result of the continuity constraint imposed on the tip section, making it relatively thicker compared to the rest of the wing which reduced in thickness.

Following from the lift distribution shown in Figure 5.11, the change in cross-sectional shape of the wing furthermore results in a more efficient outboard wing for *single step design (3)*. The sudden loss of lift near η = 0.60, is removed and a more elliptical distribution is obtained. The main reason for this improvement is found in the movement of the leading and trailing edge of the streamwise airfoil sections seen in Figure 5.10. This results in a more negative incidence angle, thereby rendering the outboard wing more efficient. While the objective of the baseline optimisation is to enhance the lift distribution, the single step FFD optimisation performs this task better. This can be attributed to the fact that the FFD optimisation provides more design flexibility to overcome the adverse effects of the increased wing thickness as opposed to the baseline optimisation. To summarise, *single step design (3)* outperforms *baseline design (2)* due to the reduced upper surface shock wave strength in combination with a reduced angle of attack and a more efficient outboard wing. The design can however experience more trim drag due to the increased nose-up pitching moment.

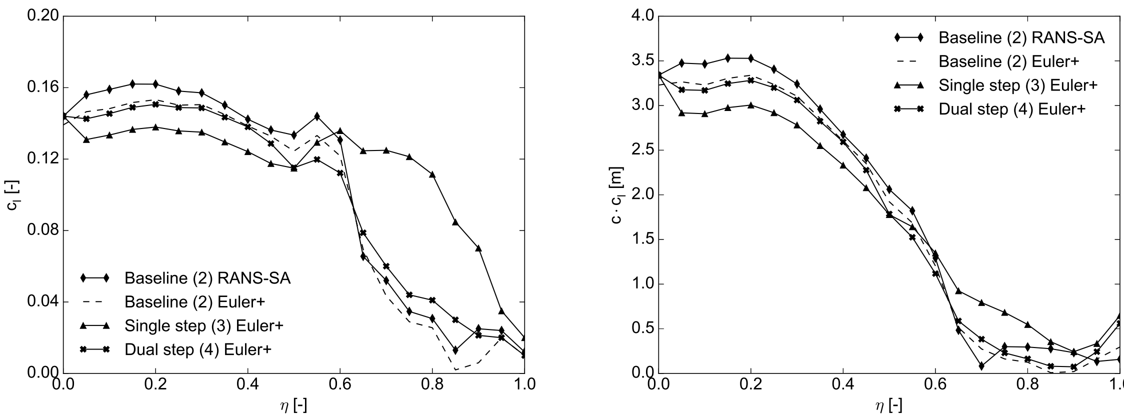

(a) Lift coefficient distribution

(b) Lift distribution

Figure 5.11: Spanwise lift and lift coefficient distribution for the baseline (2), single (3) and dual step (4) design at C_L = 0.26 and M = 0.85.

5.5. Dual Step Optimisation

To account for other disciplines besides aerodynamics, the integration of the control surfaces is considered during the dual step FFD optimisation. This provides a better picture of the potential of the Flying V, while ensuring the feasibility of the design on multiple levels. As explained in Chapter 3, the integration of the control surface design splits the FFD optimisation in two steps by using two different FFD boxes based on the hinge line location. Also in this case, the FFD boxes are described by 12 control points in the x and y direction, and 2 in the z direction. Additional continuity constraints are however imposed compared to the single step FFD optimisation. The plane of the FFD box coinciding with the plane of the hinge line is namely constrained by a continuity constraint. For the first step in this process, in which the wing in front of the hinge line is optimised, this means that the aft face of the box is constrained. Whereas the front face is constrained during the second optimisation step in which the geometry aft of the hinge line is addressed. This results in a total of 220 design variables for both steps of the FFD optimisation. The first optimisation step is finished after 30 design iterations in 7.5 hours. Subsequently, the second step of the optimisation terminated after 28 design iterations in 5.8 hours. The reduced time for the second step can be attributed to the fact that a smaller area is optimised, thereby smaller geometry and mesh deformations are needed. This means that both of these steps visualised in the optimisation loop in Figure 3.11 require less computational time.

The final result of this FFD optimisation is called *dual step design (4)* and presents an aerodynamic efficiency of 19.4 as obtained by the augmented Euler+ model. Translating to a mere 1.6% increase compared to *baseline design (2)*. This immediately provides an indication of the effect of the control surface integration. Due to the fixed plane of the hinge line, the cross-sectional shape of the wing cannot change significantly. This is best seen in Figure 5.12b at x/c = 0.65, where the location of the hinge line in this section is clearly visible due to the unchanged geometry. Also the movement of the trailing edge is limited due to the control surface integration, thereby reducing the design flexibility and the possibility of obtaining a favourable lift distribution. This is verified by Figure 5.11. As the incidence angle only slightly changed, *dual step design (4)* exhibits a marginally better lift distribution than *baseline design (2)*. Another effect of the reduced design flexibility is the small decrease in upper surface shock wave strength. As presented in Figure 5.3, the non-uniform deformation even results in additional shock waves on the inboard wing sections. This results in a more adverse behaviour of the pressure coefficient as seen in Figure 5.12a at x/c = 0.75 and 0.85. Additionally, a lambda shock is observed on the lower surface of the wing at x/c = 0.80 in Figure 5.12b and B.2.

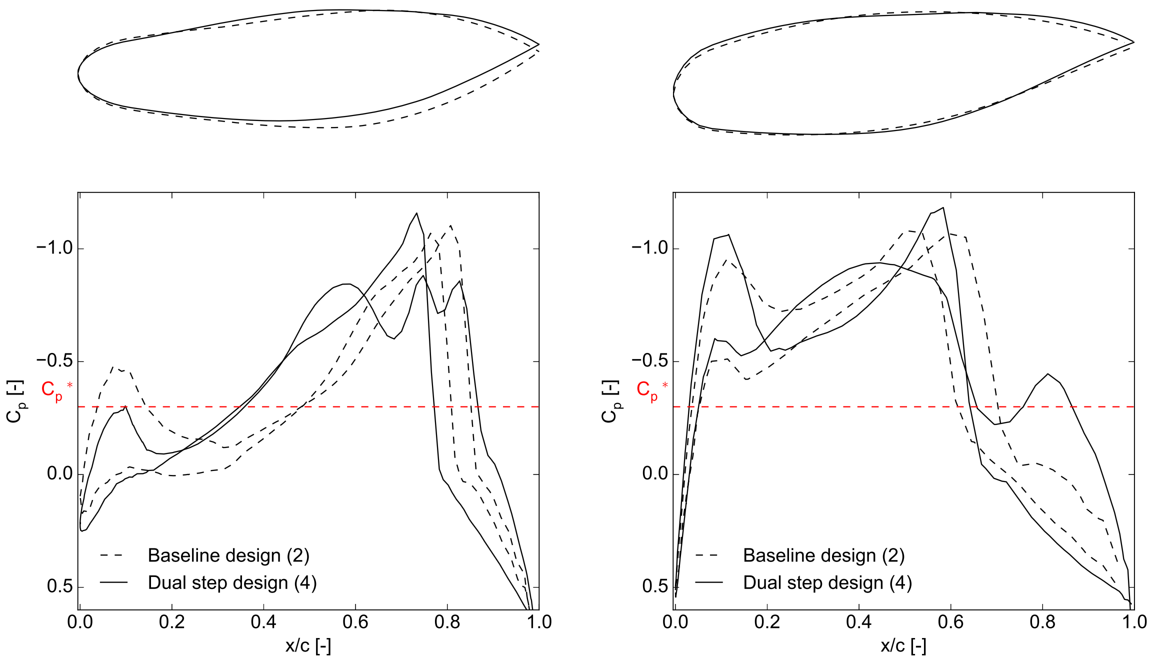

(a) η = 0.60

(b) η = 0.80

Figure 5.12: Euler pressure coefficient and airfoil section of the baseline (2) and dual step (4) design at C_L = 0.26, M = 0.85 and C_p^* = -0.30.

Despite the small changes in geometry and addition of small shock waves, the overall shock wave strength on the outboard wing is to some extend less compared to *baseline design (2)*. This is confirmed by the small increase in pitching moment coefficient shown in Table 5.2. This is attributed to the suction area on the nose of the aircraft becoming relatively stronger due to the weaker outboard wing shocks, thereby influencing the pitching moment increasingly. Again, this can result in additional trim drag due to the increased control surface deflections. Also observed in Table 5.2 is the decrease in cruise angle of attack of 0.2°, yielding a lower aircraft weight due to the reduced landing gear length required to fulfil landing restrictions.

5.6. Overall Design Comparison

Previous sections focus on the effects of the individual design steps, however also an overall design comparison is conducted. The comparison is divided into the analyses of the aerodynamic performance summarised in Table 5.2, and an additional analyses of the Oswald efficiency factor of the designs. Section 5.6.1 discusses the performance aspects, whereafter Section 5.6.2 dives into the determination and results of the Oswald efficiency factor.

5.6.1. Aerodynamic Performance

To evaluate the best design steps and determine the effects of the implemented constraints and design changes, all designs are evaluated in an open framework. A notable observation is the fact that the aerodynamic efficiency of *single step design (3)* increased with 6.3% compared to *baseline design (2)*, however, no improvement is present when comparing the design against *initial design (1)*. Specifically, the lift-to-drag ratio of *single step design (3)* is 5.2% lower than the efficiency of *initial design (1)*. This underlines the severity of the adverse effects of the design changes incorporated into the baseline optimisation; a higher thickness-to-chord ratio in combination with a larger taper ratio is detrimental for the design of a transonic wing. However, *single step design (3)* outperforms *initial design (1)* on another aspect. A reduced cruise angle of attack can be attained which can have favourable impacts on the design of the aircraft. While it is known that the Euler+ model underestimates the angle of attack, an approximate correction can be made by looking at the predictions for *baseline design (2)* for both the SU2 RANS-SA and Euler+ models presented in Section 5.1. If the angle of attack is underestimated by 0.6°by the Euler+ model, it means that *single step design (3)* requires a 0.2°smaller angle of attack than *initial design (1)*. Even a small decrease can impact the weight of the landing gear through the snowball effect. Another aspect worth considering is the lift distribution. *Single step design (3)* exhibits a more favourable lift distribution as opposed to *initial design (1)*. This can be seen in Figures 5.5 and 5.11. *Initial design (1)* shows a large drop in lift at η = 0.60 whereas *single step design (3)* presents a more gradual decrease towards the tip of the wing, thereby increasing the outboard wing efficiency.

A larger decrease in aerodynamic efficiency is observed when comparing *initial design (1)* to *dual step design (4)*. The lift-to-drag ratio for the latter is namely 9.3% lower. Additionally, the outboard wing efficiency is not significantly improved compared to *initial design (1)* as seen in Figures 5.5 and 5.11. This is attributed to the limitations imposed on the design flexibility due to the integration of the control surfaces. A better understanding of the effect of the control surface integration is provided by comparing *single step design (3)* and *dual step design (4)*. The most important effect of the reduced design flexibility is the 4.4% lower lift-to-drag ratio for *dual step design (4)* as compared to *single step design (3)*. From this, it can be deduced that the integration of the control surfaces has a non-negligible impact on the resulting design and aerodynamic performance of the aircraft. In detail, the integration significantly limits the design flexibility as the control points in the plane of the hinge line are frozen. Adjacent planes and their control points are also frozen due to the implemented continuity constraint. The surface curvature and trailing edge position can therefore not be altered sufficiently, thereby limiting the reduction of supervelocities and increase in outboard wing efficiency respectively. Considering all designs, solely *initial design (1)* meets the target lift-to-drag ratio for the Flying V of 20.5 as found by Oosterom and Vos [59]. However, *single step design (3)* is relatively close to this and can be further tweaked by also addressing the design of the inboard wing and the winglets. However, the feasibility aspect of this design is debatable.

Another important performance metric is the pitching moment coefficient as this determines the amount of trim drag the aircraft experiences. To minimise this drag, a strict constraint is imposed on the value of the pitching moment coefficient during the FFD optimisation. Nevertheless, none of the designs meet this criterion as seen in Table 5.2. In particular, the pitching moment increases in the nose-up direction with every design step taken. This is caused by the effect of the large suction area on the nose of the aircraft in combination with the relatively inefficient outboard wing. It must however be noted that the pitching moment coefficients predicted by the Euler+ model are overestimated by 0.025 as concluded in Section 5.1. The required control surface deflections to trim the aircraft are therefore expected to be smaller, thereby resulting in less trim drag than following from the values listed in Table 5.2. A solution for the increased pitching moment coefficient is found in shifting the centre of gravity forward which can be done without affecting the stability margin. On the other hand, increasing the outboard loading also decreases the nose-up tendency and simultaneously improves the efficiency of the outboard wing. To summarise, *initial design (1)* is superior in terms of aerodynamic efficiency, however *single step design (3)* presents the most efficient outboard wing. Additionally, *dual step design (4)* represents the most feasible design as it incorporates the required design changes as well as the control surface integration. These however also limit the design flexibility of the optimiser, resulting in a deteriorated aerodynamic performance.

5.6.2. Oswald Efficiency Factor

Additional performance comparisons can be performed based on the Oswald efficiency factor. The Oswald efficiency factor is a measure of the deviation in drag of a wing or aircraft with respect to a wing or aircraft exhibiting the same aspect ratio but with a perfectly elliptical lift distribution. This value is based on the zero lift drag component as obtained from the empirical viscous drag module of Faggiano [11], and the total drag coefficient listed in Table 5.2. An additional result of this calculation is the expected maximum lift-to-drag ratio, and the corresponding lift coefficient. The results for the analyses are collected in Table 5.5. The highest Oswald efficiency factor is found for *initial design (1)*, followed by *single step design (3)* and *dual step design (4)*. This ranking corresponds to the designs with the highest lift-to-drag ratio as found by the CFD analyses in Table 5.2.

A discrepancy is however observed between the maximum lift-to-drag ratio as obtained using the Oswald efficiency factor and the values acquired for the drag polar curves visualised in Figure 5.1. The drag polar curves do not show a maximum value, but steadily increase with increasing lift coefficient. These results imply that the aircraft can fly at higher lift coefficients with a higher efficiency than assumed before. This is however deemed unfeasible. The root cause for this problem is found in the fact that SU2 does not model 3D effects, while these effects can severely impact the aerodynamic performance especially at high lift coefficients where separation can occur [60]. Analysis shows that all designs experience a local Mach number higher than 1.3 at high lift coefficients, meaning that shock induced separation is expected yielding more pronounced 3D effects. Moreover, the SA turbulence model is known to be inaccurate when shock wave-boundary layer interaction flows are present [58, 60]. The drag polar curves shown in Figure 5.1 are therefore deemed inaccurate at higher lift coefficients. Thence, the expected maximum lift-to-drag ratio is assumed to be closer to the values obtained using the Oswald efficiency factor as shown in Table 5.5. These results also imply that the design lift coefficient must be increased to approximately 0.30 to reach the point of maximum efficiency. The current design lift coefficient of 0.26 is therefore underestimated.

Table 5.5: Zero lift drag coefficient and Oswald efficiency factor for designs (0) up to (4).

Design	Flow model	C_{D_0} [-]	S_{ref} [m^2]	AR [-]	e [-]	$(\frac{C_L}{C_D})_{\text{max}}$ [-]	$C_{L_{\text{opt}}}$ [-]
Linear Design (0)	RANS-SA	79.9	875.1	4.83	0.673	17.9	0.29
Initial Design (1)	RANS-SA	75.6	875.1	4.83	0.965	22.0	0.33
Baseline Design (2)	RANS-SA	76.2	876.5	4.82	0.732	19.1	0.29
Baseline Design (2)	Euler+	76.2	876.5	4.82	0.746	19.3	0.29
Single Step Design (3)	Euler+	76.7	876.5	4.82	0.867	20.7	0.31
Dual Step Design (4)	Euler+	76.4	876.5	4.82	0.773	19.6	0.30

5.7. Parameter Sensitivity Study

All designs following from the aerodynamic design process feature an undesirable thick outboard wing. Both FFD optimisations have limited design flexibility to solve this issue due to the continuity constraint imposed on the root of the outboard wing, corresponding to oval section 3. A parameter sensitivity study is therefore conducted to evaluate the effect of reducing the thickness of section 3. By reducing the thickness of the wing root, the gradual thickness change towards the tip is less, thereby resulting in an overall thinner wing. Note however that oval section 3 cannot be freely adjusted as the shape is dictated by top level requirements related to the placement of cargo containers. Decreasing the thickness of the oval section therefore means that the resulting design might violate these requirements. However, to evaluate whether the violation is deemed acceptable, the benefits of a reduced thickness are investigated. The parametrisation of section 3 is visualised in Figure 5.13 [16]. The three variables describing the thickness of the section are the crown height H_1, the oval cabin height H_2, and the keel height H_3. Decreasing both the keel and crown height results in parameter study design 1, whereas decreasing the oval cabin height results in parameter study design 2. *Baseline design (2)* is taken as reference to evaluate the resulting aerodynamic performance which is obtained using the SU2 RANS-SA model. The results of the parameter sensitivity study are shown in Table 5.6. Additionally, the change in streamwise airfoil profile at η = 0.60 is visualised in Figure 5.14.

Following from the results of parameter study design 1, it is observed that decreasing the total thickness by 9.4% results in a 0.94% increase in lift-to-drag ratio. On the other hand, reducing the thickness by 4.7% using the oval cabin height yields an efficiency improvement of 0.37%. Moreover, a small decrease in friction drag is observed for both designs, however a larger decrease is found for design 1. By decreasing the keel and crown height, the upper and lower surface reduce in curvature, resulting in a slight decrease in wetted area. Additionally, due to the reduced curvature, lower supervelocities and thus weaker shock waves are present over the wing, thereby reducing the pressure drag as well. Decreasing the keel and crown height is therefore more effective in increasing the lift-to-drag ratio than adjusting the oval cabin height. A trade-off must however be made to evaluate whether the increase in efficiency is sufficient to accept the violation of top level requirements. A solution can be found in combining this approach with other thickness reducing techniques on the outboard wing. This can eventually result in the desired efficiency gain without a strong violation of the top level requirements.

Table 5.6: Oval section 3 design parameters and SU2 RANS-SA aerodynamic coefficients at C_L = 0.26, Re = 1.135x10^8 and M = 0.85.

Design	H_1 [m]	H_3 [m]	H_2 [m]	α [°]	C_D [-]	C_{D_p} [-]	C_{D_f} [-]	C_m [-]	C_L/C_D [-]
Baseline Design (2)	0.45	0.45	1.22	2.2	136.2	90.3	45.9	0.044	19.08
Parameter study 1	0.35	0.35	1.22	2.2	135.0	89.5	45.5	0.043	19.26
Parameter study 2	0.45	0.45	1.12	2.2	135.8	90	45.8	0.044	19.15

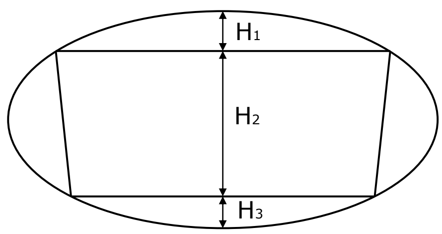

Figure 5.13: Oval cabin parametrisation by Hillen [16].

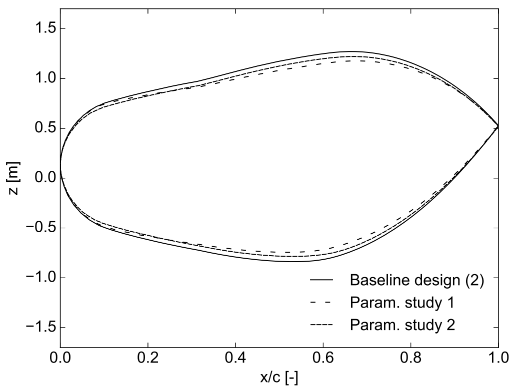

Figure 5.14: Cross-sectional shape at η = 0.60 for baseline design (2), and parameter study designs 1 and 2.

6 Conclusion

The goal of this study is to optimise the design of the outboard wing of the Flying V to maximise the lift-to-drag ratio at its design condition. For this, an aerodynamic design strategy is devised which consists out of various steps. The first step is the geometry preparation in which the existing linear lofted geometry is re-parameterised using Gordon surfaces. This step removes the streamwise discontinuities present in the linear lofted geometry, as well as other undesirable characteristics. This is followed by the so-called baseline design optimisation in which the planform of the aircraft is optimised to improve the lift distribution. Additionally, necessary design changes following from earlier conducted studies are implemented, which result in a more feasible and lager tip structure. The feasibility level of the design is further increased by incorporating the design of the outboard control surfaces. Once the baseline design optimisation is performed, the constrained aerodynamic shape optimisation of the outer wing is conducted following the Free-Form Deformation (FFD) parametrisation approach. Relevant constraints include a fixed design lift coefficient, a range of acceptable pitching moment coefficients, continuity constraints related to the transition of the new wing to the existing geometry, and finally the integration of the control surfaces. The FFD shape optimisation is based on the Euler equations augmented with an empirical viscous drag module. Additionally, the designs originating from the geometry preparation and the baseline design optimisation steps are analysed using a Reynolds Averaged Navier Stokes (RANS) equations flow model. This provides a better insight into the contribution of the pressure and friction drag components.

The first step of the design strategy, in which the geometry is re-parameterised using Gordon surfaces, results in an aerodynamic efficiency increase of 19.6%. While the aerodynamic performance is enhanced due to the new lofting technique, it also results in a thick outboard wing leading to strong shock waves on both the upper and lower surface. These shocks render the outboard wing inefficient with respect to the amount of lift generated. The subsequent baseline design optimisation therefore aims to improve the lift distribution of the aircraft, as well as the feasibility aspect of the design. However, as the implemented design changes increase the wing thickness further, the lift-to-drag ratio decreases from 21.4 to 19.1. The FFD based shape optimisation thereafter tries to reduce the thickness of the wing as much as possible, while respecting the implemented constraints. This results in an aerodynamic efficiency of 19.4 in cruise conditions. To evaluate the effect of the outboard control surface constraint, an additional FFD optimisation is conducted in which this constraint is neglected. This optimisation results in a cruise lift-to-drag ratio of 20.3.

It is found that the largest increase in performance results from the re-parametrisation of the geometry. The resulting design also presents the highest aerodynamic efficiency among all designs developed in this study. However, as the design changes related to the tip structure, and the control surface integration are not considered in this step of the process, the feasibility level of this design is inferior. The design changes implemented to enhance the feasibility do however contradict the objective of this study to increase the maximum lift-to-drag ratio. By increasing the wing thickness significantly, they result in a wing opposing the design guidelines for transonic wings. The subsequent FFD shape optimisation therefore reduces the thickness as much as possible to minimise the shock wave strength on the wing. However, due to the continuity constraints related to the transition of the outboard wing to the inboard wing and winglet, the design flexibility and thus the changes in thickness are limited. This results in a final design in which the shock waves are still present. Additional analysis is thus needed to evaluate the best approach to reducing the thickness further without affecting top level requirements.

Also the integration of the outboard control surfaces further reduces the design flexibility of the optimiser. The efficiency increase reached during the FFD optimisation neglecting this constraint is significantly higher compared to the increase reached when imposing this constraint. The limited design flexibility due the control surfaces is furthermore seen in the resulting lift distribution of the designs. Whereas the FFD optimisation neglecting the control surface constraint results in a more elliptical lift distribution with a more efficient outboard wing, the optimisation including this constraint fails to improve the wing efficiency. This design then also exhibits a lift distribution with a loss of lift near the transition of the inboard to the outboard wing. From these results it can be deduced that the integration of the control surfaces has a non-negligible effect on the resulting design and aerodynamic performance of the aircraft. In particular, the integration constraint reduces the lift-to-drag ratio by 4.4%. The integration of the control surfaces should therefore be considered early in the design process to avoid adverse effects on the aircraft performance later in the design process. Overall, this study shows a successful constrained aerodynamic shape optimisation which results in an 8.4% and 13.4% increase in aerodynamic efficiency with respect to the initial linear lofted geometry depending on the integration of the control surface constraint. This design process thus not only result in an improved design from an aerodynamic perspective, but also from a structural and controllability point of view due to the implemented necessary design changes and the control surface design.

7 Recommendations

This study shows a successful constrained aerodynamic shape optimisation of the outer wing of the Flying V. However, additional research and possible improvements are recommended to fully exploit the potential of the aircraft. In particular, more research is needed to identify solutions to reduce the thickness of the outboard wing of the aircraft. Changes to the inboard wing layout can result in a more efficient transition from the inboard to the outboard wing. Thereby yielding a more effective Free-Form Deformation (FFD) optimisation which can improve the aerodynamic performance of the aircraft further. Additionally, as the Gordon surfaces lofting technique is also used to improve the inboard wing parametrisation, a study is needed into the effect of these changes related to the top level requirements driving the design of the inboard wing. Related to this is the fact that the Gordon surfaces lofting method used in this study is at an experimental level and not widely available in the ParaPy platform used to construct the Flying V geometry yet. This also means that the quality of the resulting surfaces is open to improvement, for example by allowing to loft through multiple profiles using one surface. An improved version of the current geometry can therefore be made once the Gordon surfaces functionality is rolled out completely.

The current study is limited to only analysing the designs constructed using the ParaPy platform with the higher-fidelity Reynolds Averaged Navier Stokes (RANS) equations flow model. Analysing the designs resulting from the FFD optimisation with this flow model is deemed outside the scope of the current study. However, to verify the aerodynamic performance of the designs and provide an indisputable comparison between the performance of all designs, the FFD optimised designs can also be analysed with the higher-fidelity RANS model. As the output of the FFD optimisation is an Euler mesh file containing the surface mesh of the deformed wing, a reverse engineering process is needed to retrieve the geometry and combine it with the existing geometry of the inboard wing and winglet. This allows for the construction of a new viscous mesh which can be used in the subsequent RANS analyses. As the reverse engineering process is complex, a study into the best practices to perform this process for this type of geometry is needed to ensure a high quality of the resulting geometry and subsequent mesh.

During this study it is also found that the FFD optimisation implemented in the flow solver SU2 is not able to perform these optimisations based on the RANS equations. The problem is related to the mesh deformation module of SU2. The elastic solid method currently implemented is not able to accurately deform meshes describing complex geometry while including prism layers. As SU2 is an open source platform, changes to the source code can be made. An alternative for the implemented mesh deformation method is found in the usage of radial basis functions to deform the mesh, which is more robust for viscous meshes. This method was investigated and incorporated into SU2 by Morelli et al. in their research related to aircraft icing simulations [61]. A study into the applicability to the current topic is needed to evaluate the necessity of developing a radial basis mesh deformation module.

An aspect of the FFD optimisation specific to this study is the implementation of the control surface integration constraint. The current implementation limits the design flexibility significantly, thereby hindering the optimiser to reach its full potential. A possible solution can be found in creating an additional module for the SU2 source code which automatically incorporates this constraint in the optimisation process as an additional analysis step. This module checks possible hinge line locations during every design iteration to evaluate the feasibility of the design. This removes the need to fully freeze control points in the optimisation process, thereby increasing the design flexibility. Finally, while the new parametrisation is based on the structurally efficient parametrisation of Hillen [16], significant changes are made due to the Gordon surfaces lofting technique. Therefore, the current structural design of the Flying V can be outdated. It is suggested to evaluate the validity of the existing structural design of the aircraft in combination with the geometry resulting from the new lofting technique. The additional research and possible improvements recommended in this chapter can increase the accuracy and efficiency of the developed aerodynamic design strategy in this study. Thereby contributing to the progress of the design of the Flying V.

References

[1] E. Torenbeek. "Blended Wing Body and All-Wing Airliners". In: *European Workshop on Aircraft Design Education (EWADE)* (2007), pp. 1–9.

[2] P. Smith and H. Okonkwo. "Review of Evolving Trends in Blended Wing Body Aircraft Design". In: *Progress in Aerospace Sciences* 82 (2016), pp. 1–23. DOI: 10.1016/j.paerosci.2015.12.002.

[3] N. Qin, A. Vavalle, and A.L. Moigne. "Spanwise Lift Distribution for Blended Wing Body Aircraft". In: *Journal of Aircraft* 42.2 (2005), pp. 356–365. DOI: 10.2514/1.4229.

[4] N. Qin, A. Vavalle, A. Le Moigne, M. Laban, K. Hackett, and P. Weinerfelt. "Aerodynamic considerations of blended wing body aircraft". In: *Progress in Aerospace Sciences* 40.6 (2004), pp. 321–343. ISSN: 0376-0421. DOI: 10.1016/j.paerosci.2004.08.001.

[5] N. Qin. "Aerodynamic Studies for Blended Wing Body Aircraft". In: *9th AIAA/ISSMO Symposium on Multidisciplinary Analysis and Optimization*. Multidisciplinary Analysis Optimization Conferences. American Institute of Aeronautics and Astronautics, 2002, pp. 1–11. DOI: 10.2514/6.2002-5448.

[6] J. Benad. "The Flying V - A new Aircraft Configuration for Commercial Passenger Transport". In: *Deutscher Luft- und Raumfahrtkongress 2015* (2015), pp. 1–8. DOI: 10.25967/370094.

[7] H. Smith. "College of Aeronautics Blended Wing Body Development Programme". In: *ICAS Congress 2000* (2000), pp. 1–10.

[8] R. Storck. *Flying Wings: Die historische Entwicklung der Nurflügelflugzeuge der Welt*. Vol. 1. Bernard & Graefe, 2002. ISBN: 3763762426.

[9] Z. Lyu and J.R.R.A. Martins. "Aerodynamic design optimization studies of a blended-wing-body aircraft". In: *Journal of Aircraft* 51.5 (2014), pp. 1604–1617. DOI: 10.2514/1.C032491.

[10] A.G. Lee, T.A. Reist, and D.W. Zingg. "Further exploration of regional-class hybrid wing-body aircraft through multifidelity optimization". In: *AIAA Scitech 2021 Forum*. 2021, pp. 1–21. DOI: 10.2514/1.C034703.

[11] F. Faggiono. "Aerodynamic Design Optimisation of a Flying V Aircraft". Thesis. Delft University of Technology, 2016.

[12] R. van der Pluijm. "Cockpit Design and Integration into the Flying V". Thesis. University of Technology Delft, 2021.

[13] Y. Brouwer. "Constrained Aerodynamic Optimization of the Flying-V Nose Cone and CenterBody Fairing". Thesis. University of Technology Delft, 2022.

[14] J. Horwitz. "Parametric Design of the Flying-V Winglets for Improved Lateral-Directional Stability and Control". Thesis. University of Technology Delft, 2021.

[15] W. Oosterom. "Flying-V Family Design". Thesis. University of Technology Delft, 2021.

[16] M. Hillen. "Parametrisation of the Flying V Outer Mould Line". Thesis. University of Technology Delft, 2020.

[17] E. Torenbeek. *Synthesis of Subsonic Airplane Design*. Delft University Press, 1982. ISBN: 90-247-2724-3.

[18] D.P. Raymer. *Aircraft Design: A conceptual approach*. American Institute of Aeronautics and Astronautics (AIAA), 1992. ISBN: 0-930403-51-7.

[19] B.M. Kulfan. "CST Universal Parametric Geometry Representation Method with Application to Supersonic Aircraft". In: *4th International Conference on Flow Dynamics* (2006), pp. 1–35. DOI: 10.1017/S0001924000003614.

[20] L. van der Schaft. "Development, Model Generation and Analysis of a Flying V Structure Concept". Thesis. Delft University of Technology, 2017.

[21] M. Claeys. “Flying V and Reference Aircraft Structural Analysis and Mass Comparison”. Thesis. Delft University of Technology, 2018.

[22] F. Palacios, J. Alonso, K. Duraisamy, M. Colonno, J. Hicken, A. Aranake, A. Campos, S. Copeland, T. Economon, A. Lonkar, T. Lukaczyk, and T. Taylor. “Stanford University Unstructured (SU2): An open-source integrated computational environment for multi-physics simulation and design”. In: *51st AIAA Aerospace Sciences Meeting including the New Horizons Forum and Aerospace Exposition*. Aerospace Sciences Meetings. American Institute of Aeronautics and Astronautics, 2013, pp. 1–60. DOI: 10.2514/6.2013-287.

[23] O. Gur, W.H. Mason, and J.A. Schetz. “Full-Configuration Drag Estimation”. In: *Journal of Aircraft* 47.4 (2010), pp. 1356–1367. DOI: 10.2514/1.47557.

[24] M. Drela and H. Youngren. *AVL 3.26 user primer*. 2006. URL: https://web.mit.edu/drela/Public/web/avl/.

[25] R. Storn and K. Price. “Differential Evolution – A Simple and Efficient Heuristic for global Optimization over Continuous Spaces”. In: *Journal of Global Optimization* 11.4 (1997), pp. 341–359. ISSN: 1573-2916. DOI: 10.1023/A:1008202821328.

[26] T. Nieuwenhuizen. “Conceptual Design Optimisation of a Flying V Aircraft”. Thesis. University of Technology Delft, 2021.

[27] W.J. Gordon. “Spline-Blended Surface Interpolation Through Curve Networks”. In: *Journal of Mathematics and Mechanics* 18.10 (1969), pp. 931–952. ISSN: 00959057, 19435274. (Visited on 05/03/2022).

[28] M. Siggel, M. Pelz, K. Rusch, and J. Kleinert. “The TiGL Geometry Library and its Current Mathematical Challenges”. In: *Simulation & Software Technology*. Workshop DLR / Cologne University. 2017.

[29] Marco Palermo and Roelof Vos. “Experimental Aerodynamic Analysis of a 4.6%-Scale Flying-V Subsonic Transport”. English. In: *AIAA Scitech 2020 Forum*. AIAA Scitech 2020 Forum. United States: American Institute of Aeronautics and Astronautics Inc. (AIAA), 2020. ISBN: 9781624105951. DOI: 10.2514/6.2020-2228.

[30] R.C. Nelson. *Flight Stability and Automatic Control*. Aerospace series. McGraw-Hill, 1989. ISBN: 9780070462182.

[31] A. Ruiz Garcia, M.T.H. Brown, D.M. Atherstone, N. van Arnhem, and R. Vos. “Aerodynamic Model Identification of the Flying V from Sub-Scale Flight Test Data”. In: *AIAA Scitech 2022 Forum* (2022). DOI: 10.2514/6.2022-0713.

[32] Giorgio Giorgi and Tinne Kjeldsen. *Traces and Emergence of Nonlinear Programming*. Jan. 2014. ISBN: 978-3-0348-0438-7. DOI: 10.1007/978-3-0348-0439-4.

[33] D. Tabak and B.C. Kuo. *Optimal Control by Mathematical Programming*. Instrumentation and controls series. Prentice-Hall, 1971. ISBN: 9780136381068.

[34] Thomas W. Sederberg and Scott R. Parry. “Free-Form Deformation of Solid Geometric Models”. In: SIGGRAPH ’86. New York, NY, USA: Association for Computing Machinery, 1986, pp. 151–160. ISBN: 0897911962. DOI: 10.1145/15922.15903.

[35] Guangda Yang, Andrea Da Ronch, Jernej Drofelnik, and Zheng-Tong Xie. “Sensitivity assessment of optimal solution in aerodynamic design optimisation using SU2”. In: *Aerospace Science and Technology* 81 (2018), pp. 362–374. ISSN: 1270-9638. DOI: 10.1016/j.ast.2018.08.012.

[36] Richard P. Dwight. “Robust Mesh Deformation using the Linear Elasticity Equations”. In: *Computational Fluid Dynamics 2006*. Ed. by Herman Deconinck and E. Dick. Berlin, Heidelberg: Springer Berlin Heidelberg, 2009, pp. 401–406. ISBN: 978-3-540-92779-2. DOI: 10.1007/978-3-540-92779-2_62.

[37] Yin Yu, Zhoujie Lyu, Zelu Xu, and Joaquim R. R. A. Martins. “On the influence of optimization algorithm and initial design on wing aerodynamic shape optimization”. In: *Aerospace Science and Technology* 75 (2018), pp. 183–199. ISSN: 1270-9638. DOI: 10.1016/j.ast.2018.01.016.

[38] Z. Lyu and J. R. R. A. Martins. “Aerodynamic design optimization studies of a blended-wing-body aircraft”. In: *Journal of Aircraft* 51.5 (2014), pp. 1604–1617. DOI: 10.2514/1.C032491.

[39] Zhoujie Lyu, Gaetan K.W. Kenway, and Joaquim R.R.A. Martins. “Aerodynamic shape optimization investigations of the common research model wing benchmark”. In: *AIAA Journal* 53.4 (2015), pp. 968–985. DOI: 10.2514/1.J053318.

[40] PF Roysdon. “Blended wing body lateral-directional stability investigation using 6DOF simulation”. In: *Proceedings of the Institution of Mechanical Engineers, Part G: Journal of Aerospace Engineering* 228.1 (2014), pp. 7–19. DOI: 10.1177/0954410013483633.

[41] Kelei Wang and Zhou Zhou. “Aerodynamic Design, Analysis and Validation of a Small Blended-Wing-Body Unmanned Aerial Vehicle”. In: *Aerospace* 9.1 (2022). ISSN: 2226-4310. DOI: 10.3390/aerospace9010036.

[42] M. Palermo. “The Longitudinal Static Stability and Control Characteristics of a Flying V Scaled Model: An Experimental and Numerical Investigation”. Thesis. University of Technology Delft, 2019.

[43] A. Ruiz Garcia. “Aerodynamic Model Identification of the Flying V using Wind Tunnel Data”. Thesis. University of Technology Delft, 2019.

[44] R. Viet. “Analysis of the flight characteristics of a highly swept cranked flying wing by means of an experimental test”. Thesis. University of Technology Delft, 2019.

[45] J. Blazek. *Computational Fluid Dynamics: Principles and Applications*. Elsevier, 2005. ISBN: 0080430090.

[46] F. Menter. “Two-equation eddy-viscosity turbulence models for engineering applications”. In: *AIAA Journal* 32 (1994), pp. 1598–1605. DOI: 10.2514/3.12149.

[47] William Chan, Reynaldo Gomez, Stuart Rogers, and Pieter Buning. “Best Practices in Overset Grid Generation”. In: *32nd AIAA Fluid Dynamics Conference and Exhibit*. 2002. DOI: 10.2514/6.2002-3191.

[48] W. Versprille. “Aerodynamic Shape Optimization of a Liquid-Hydroge-Powered Blended-Wing-Body”. Thesis. University of Technology Delft, 2021.

[49] H. Schlichting and K. Gersten. *Boundary-Layer Theory*. Vol. 8. Springer, 2000. ISBN: 3540662707.

[50] P.M. Kurowski and Society of Automotive Engineers. *Finite Element Analysis for Design Engineers*. Electronic publications. SAE International, 2017. ISBN: 9780768083705.

[51] N.S. Gokhale. *Practical Finite Element Analysis*. Finite To Infinite, 2008. ISBN: 9788190619516.

[52] V. Schmitt and F. Charpin. *Pressure Distributions on the Onera-M6-Wing at Transonic Mach Numbers: Experimental Data Base for Computer Program Assessment*. Tech. report 138. Fluid Dynamics Working Group 04, AGARD AR, 1979.

[53] Guillermo Araya. “Turbulence Model Assessment in Compressible Flows around Complex Geometries with Unstructured Grids”. In: *Fluids* 4 (Apr. 2019), p. 81. DOI: 10.3390/fluids4020081.

[54] Alan Le Moigne and Ning Qin. “Variable-Fidelity Aerodynamic Optimization for Turbulent Flows Using a Discrete Adjoint Formulation”. In: *AIAA Journal* 42.7 (2004), pp. 1281–1292. DOI: 10.2514/1.2109.

[55] Eric J. Nielsen and W. Kyle Anderson. “Recent Improvements in Aerodynamic Design Optimization on Unstructured Meshes”. In: *AIAA Journal* 40.6 (2002), pp. 1155–1163. DOI: 10.2514/2.1765.

[56] Adrien Crovato, Hugo S. Almeida, Gareth Vio, Gustavo H. Silva, Alex P. Prado, Carlos Breviglieri, Huseyin Guner, Pedro H. Cabral, Romain Boman, Vincent E. Terrapon, and Grigorios Dimitriadis. “Effect of Levels of Fidelity on Steady Aerodynamic and Static Aeroelastic Computations”. In: *Aerospace* 7.4 (2020). ISSN: 2226-4310. DOI: 10.3390/aerospace7040042.

[57] John D. Anderson. *Fundamentals of aerodynamics*. 5th. McGraw-Hill, Feb. 2011. ISBN: 9780073398105.

[58] Li Ma, Lipeng Lu, Jian Fang, and Qiuhui Wang. “A study on turbulence transportation and modification of Spalart–Allmaras model for shock-wave/turbulent boundary layer interaction flow”. In: *Chinese Journal of Aeronautics* 27.2 (2014), pp. 200–209. DOI: 10.1016/j.cja.2014.02.008.

[59] Wilco Oosterom and Roelof Vos. “Conceptual Design of a Flying-V Aircraft Family”. In: *AIAA AVIATION 2022 Forum*. 2022. DOI: 10.2514/6.2022-3200.

[60] Francisco Palacios, Thomas Economon, Aniket Aranake, Sean Copeland, Amrita Lonkar, Trent Lukaczyk, David Manosalvas-Kjono, Kedar Naik, A Padrón, Brendan Tracey, Anil Variyar, and Juan Alonso. “Stanford University Unstructured (SU2): Analysis and Design Technology for Turbulent Flows”. In: Jan. 2014. DOI: 10.2514/6.2014-0243.

[61] Myles Morelli, Tommaso Bellosta, and Alberto Guardone. “Efficient radial basis function mesh deformation methods for aircraft icing”. In: *Journal of Computational and Applied Mathematics* 392 (2021), p. 113492. ISSN: 0377-0427. DOI: 10.1016/j.cam.2021.113492.

A

Onera M6 Wing Pressure Distributions

This appendix contains all chordwise pressure distributions obtained during the validation process of the SU2 RANS-SA model based on the Onera M6 Wing. Due to the similarity of the pressure distributions, the results for a limited number of spanwise locations are discussed in detail in Chapter 4. For sake of comparison, the complete set of pressure distribution comparisons is presented here.

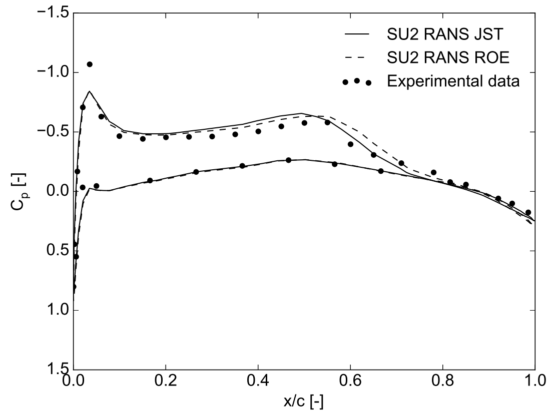

(a) η = 0.20

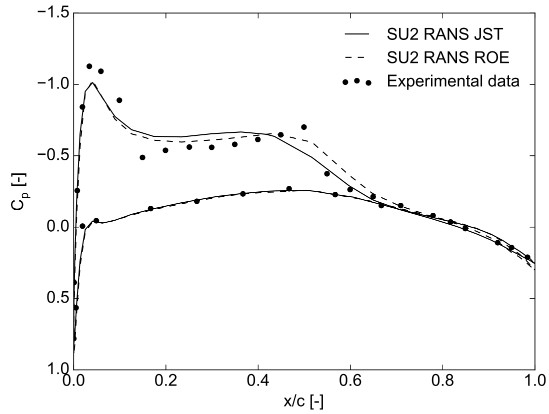

(b) η = 0.44

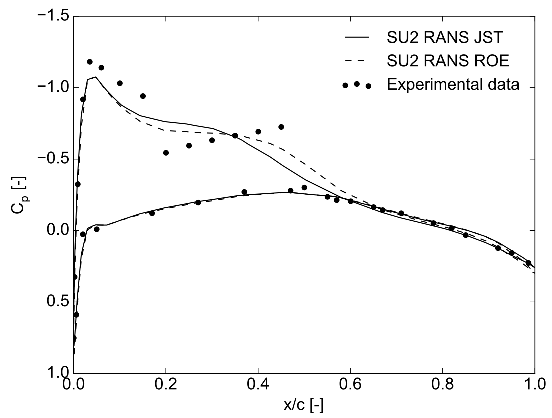

(c) η = 0.65

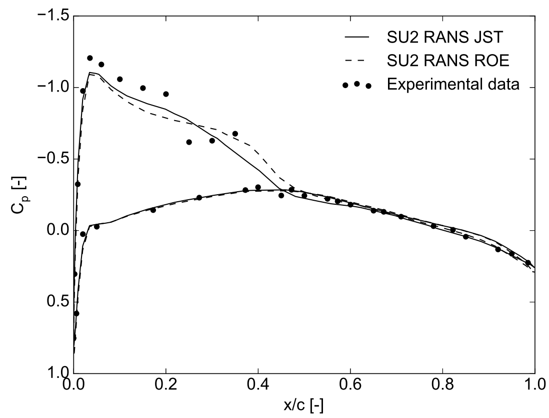

(d) η = 0.80

Figure A.1: SU2 RANS-SA solver validation using experimental data of the Onera M6 wing test 2308 at spanwise wing stations η = 0.20, 0.44, 0.65, 0.80.

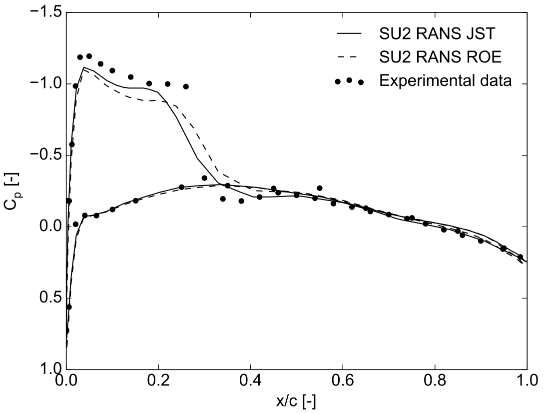

(a) η = 0.90

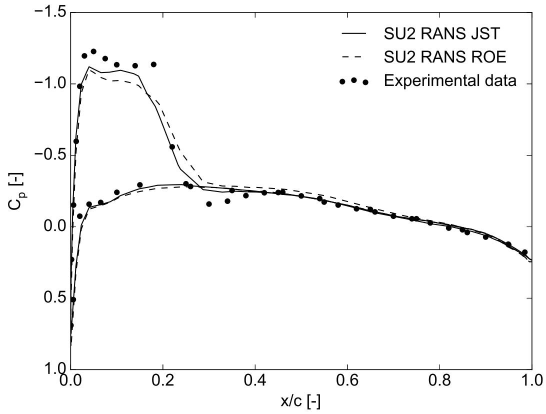

(b) η = 0.95

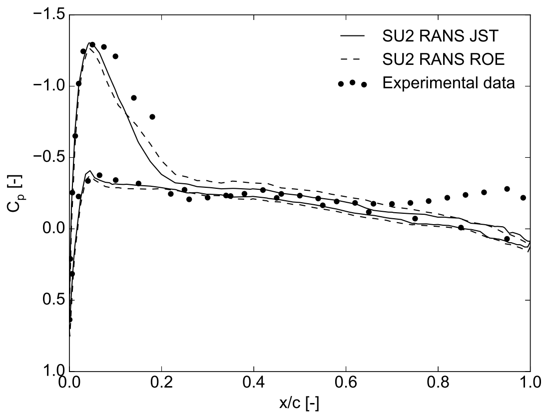

(c) η = 0.99

Figure A.2: SU2 RANS-SA solver validation using experimental data of the Onera M6 wing test 2308 at spanwise wing stations η = 0.90, 0.95, 0.99.

B

Flying V Pressure & Friction Distributions

This appendix contains additional pressure and friction distributions as obtained during the aerodynamic design process of the outer wing of the Flying V. The presented figures display the pressure coefficient along the complete lower surface of the outboard wing, as well as the chordwise pressure and friction coefficient distributions for additional spanwise locations. Due to the similarity of the distributions, the results for a limited number of spanwise locations are discussed in detail in Chapter 5. For sake of comparison, the complete set of chordwise pressure and friction coefficient distributions is presented here.

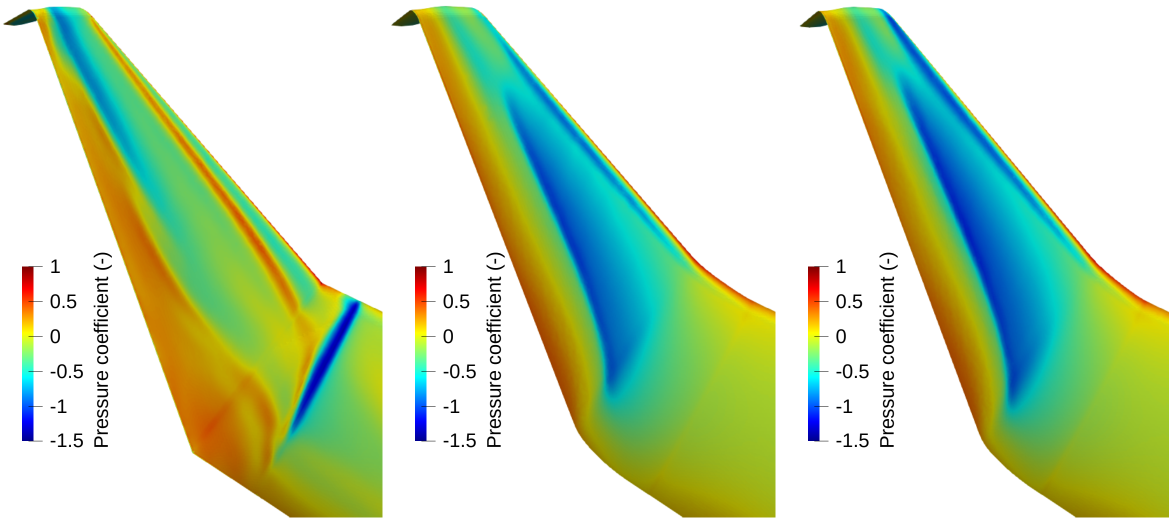

(a) Linear design (0) **(b)** Initial design (1) **(c)** Baseline design (2)

Figure B.1: SU2 RANS-SA outer wing lower surface pressure distributions of the linear (0), initial (1) and baseline (2) designs at Re = 1.135x10^8, M = 0.85, and C_L = 0.26 with $\bar{c}$ = 17.7 m.

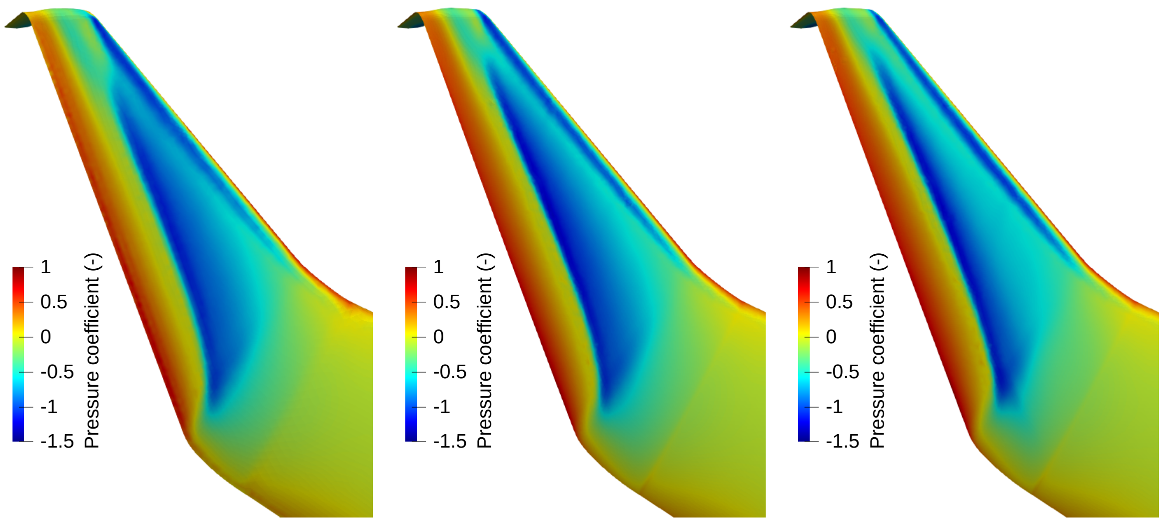

(a) Baseline design (2) **(b)** Single step design (3) **(c)** Dual step design (4)

Figure B.2: SU2 Euler outer wing lower surface pressure distributions of the baseline (2), single (3) and dual step (4) designs at M = 0.85, and C_L = 0.26 with $\bar{c}$ = 17.7 m.

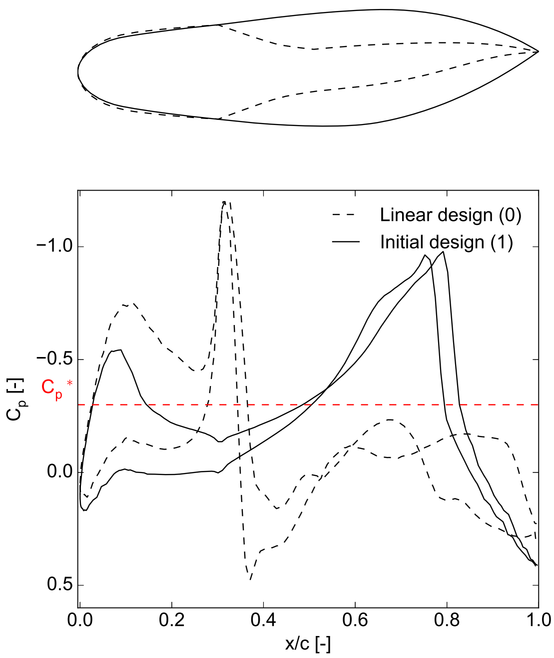

(a) η = 0.60

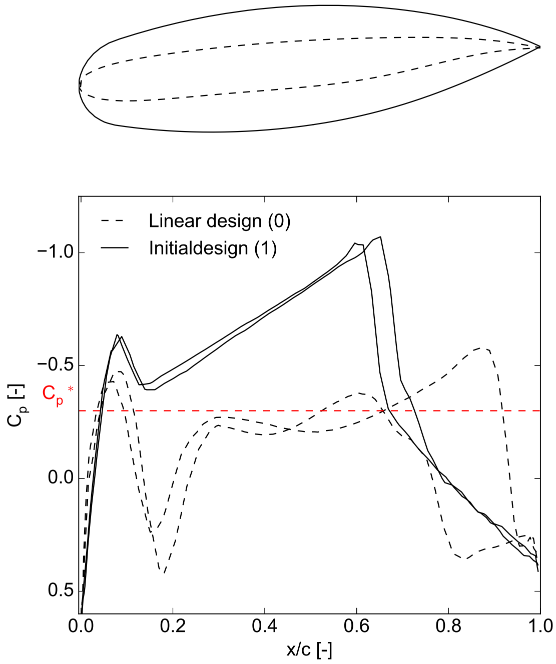

(b) η = 0.70

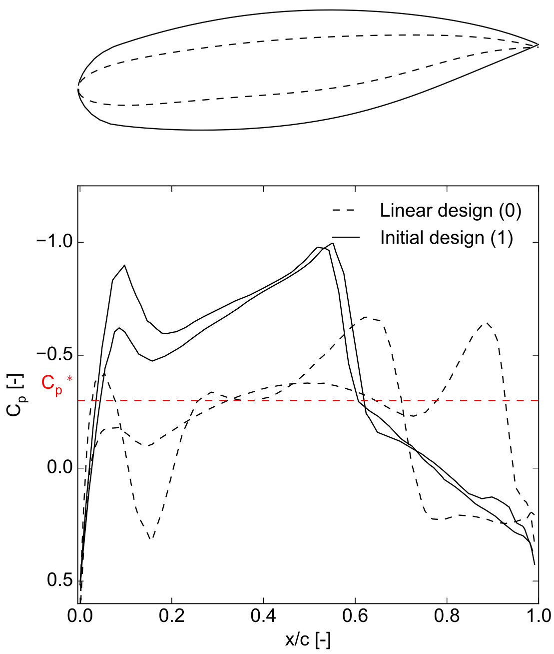

(c) η = 0.80

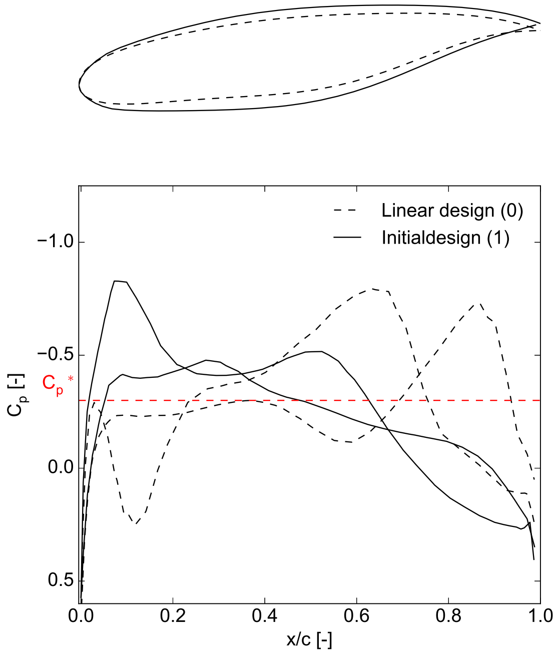

(d) η = 0.90

Figure B.3: RANS-SA pressure coefficient and airfoil section of the linear (0) and initial (1) design at C_L = 0.26, Re = 1.135x10^8, M = 0.85 and C_p^* = -0.30 for η = 0.60, 0.70, 0.80 & 0.90.

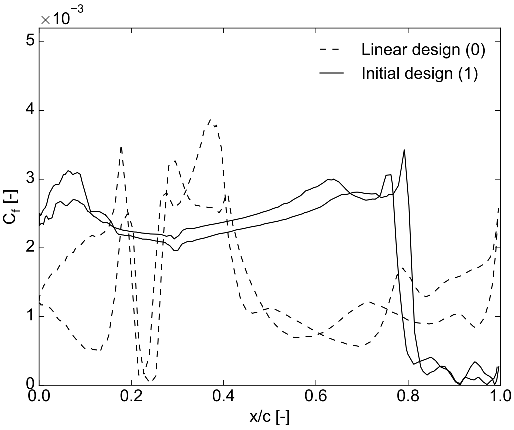

(a) η = 0.60

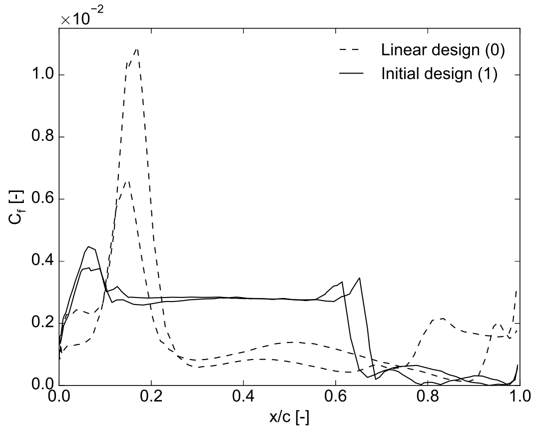

(b) η = 0.70

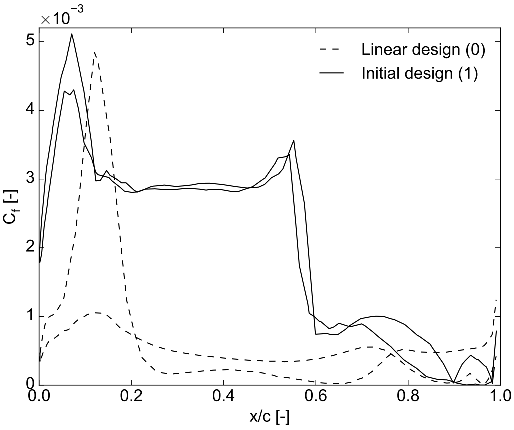

(c) η = 0.80

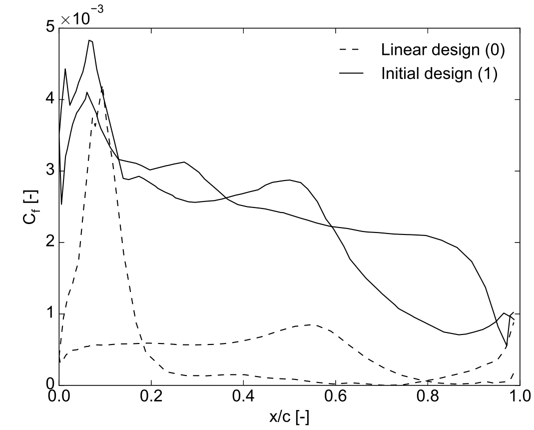

(d) η = 0.90

Figure B.4: SU2 RANS-SA friction coefficient of the linear (0) and initial (1) design at C_L = 0.26, Re = 1.135x10^8 and M = 0.85 for η = 0.60, 0.70, 0.80 & 0.90.

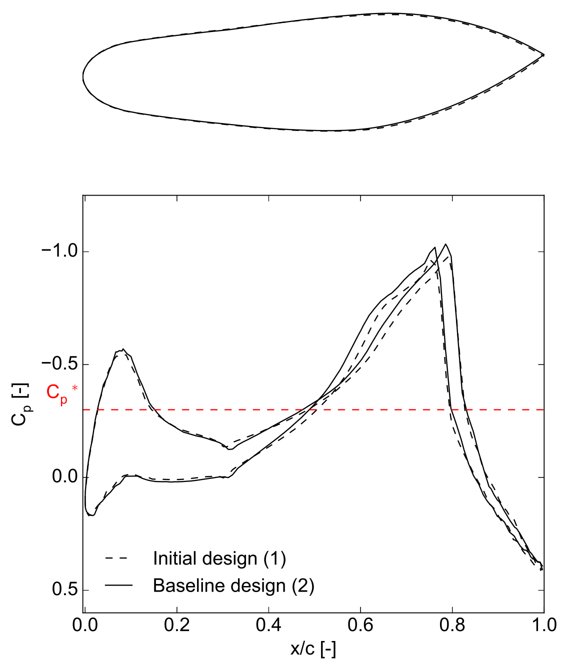

(a) η = 0.60

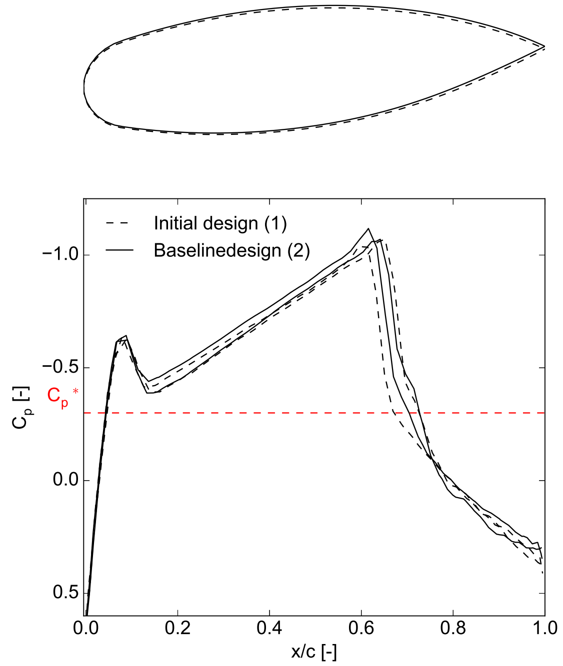

(b) η = 0.70

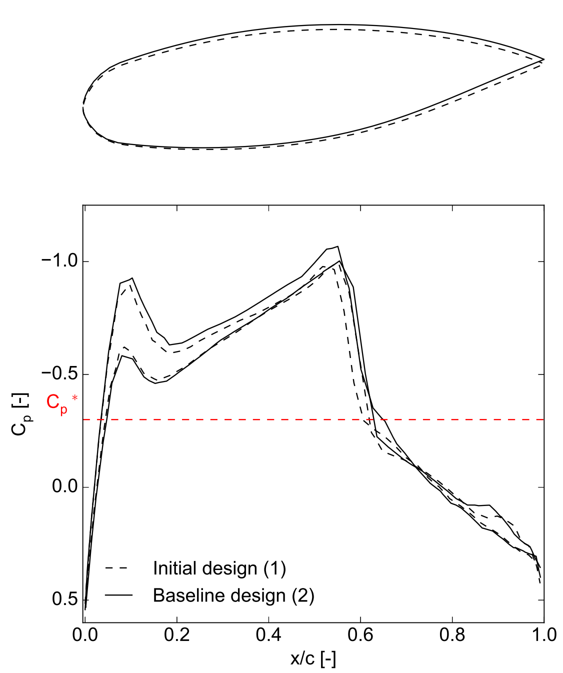

(c) η = 0.80

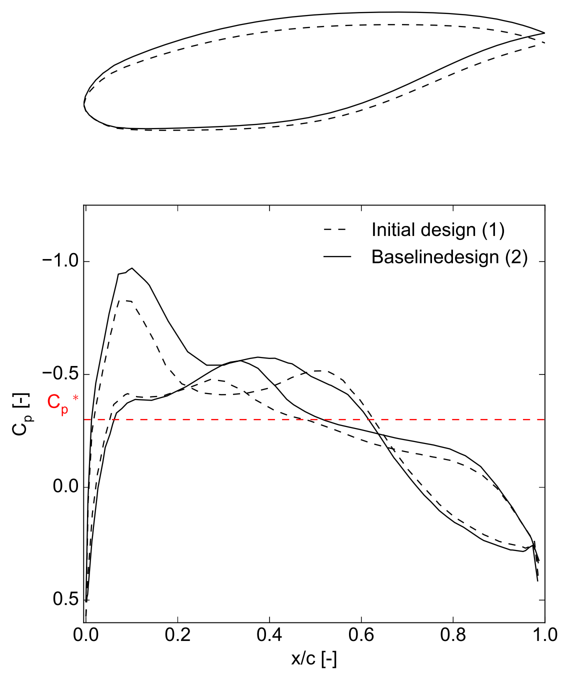

(d) η = 0.90

Figure B.5: RANS-SA pressure coefficient and airfoil section of the initial (1) and baseline (2) design at C_L = 0.26, Re = 1.135x10^8, M = 0.85 and C_p^* = -0.30 for η = 0.60, 0.70, 0.80 & 0.90.

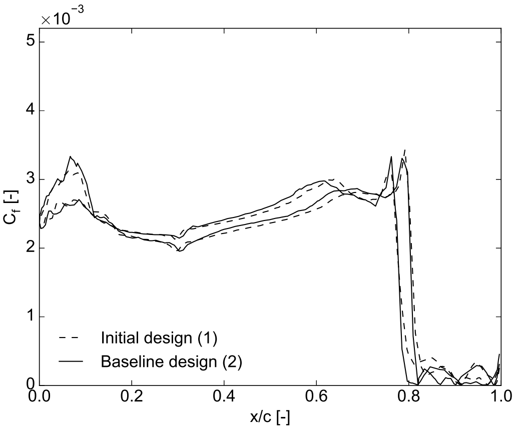

(a) η = 0.60

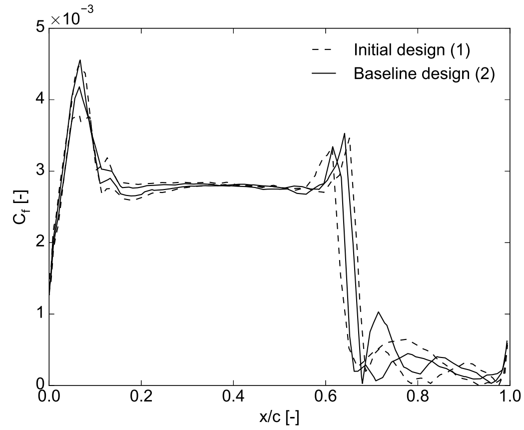

(b) η = 0.70

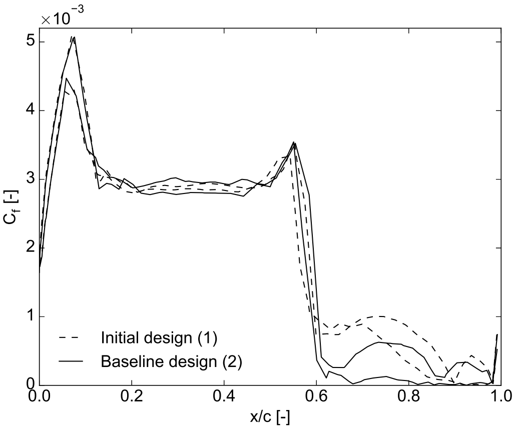

(c) η = 0.80

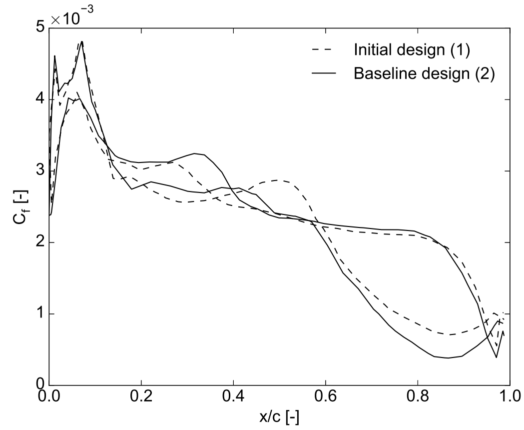

(d) η = 0.90

Figure B.6: SU2 RANS-SA friction coefficient of the initial (1) and baseline (2) design at C_L = 0.26, Re = 1.135x10^8 and M = 0.85 for η = 0.60, 0.70, 0.80 & 0.90.

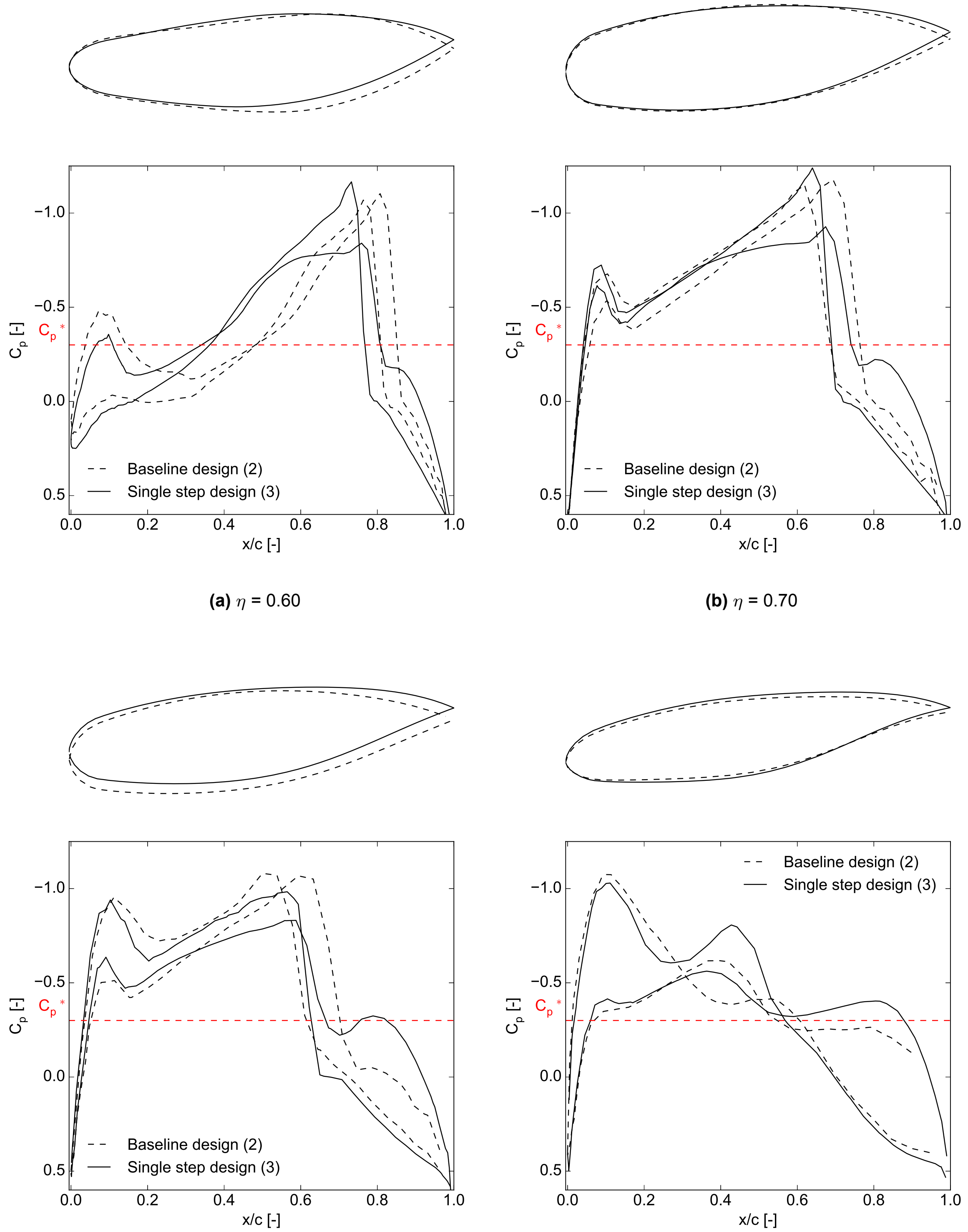

(a) η = 0.60

(b) η = 0.70

(c) η = 0.80

(d) η = 0.90

Figure B.7: RANS-SA pressure coefficient and airfoil section of the baseline (2) and single step (3) design at C_L = 0.26, Re = 1.135x10^8, M = 0.85 and C_p^* = -0.30 for η = 0.60, 0.70, 0.80 & 0.90.

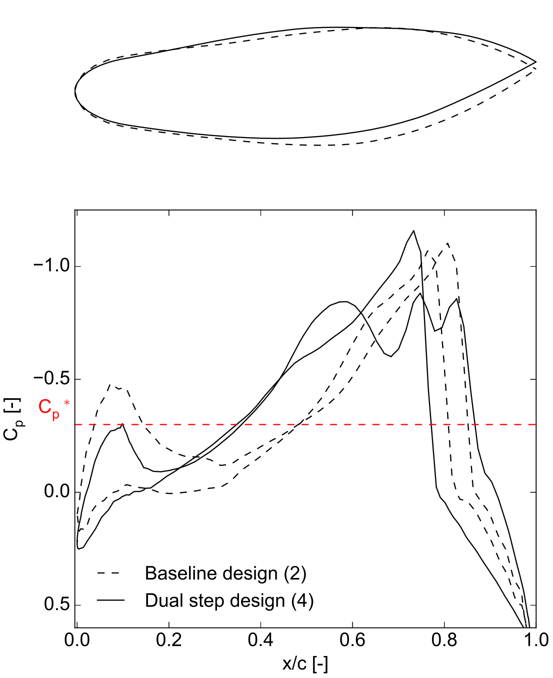

(a) η = 0.60

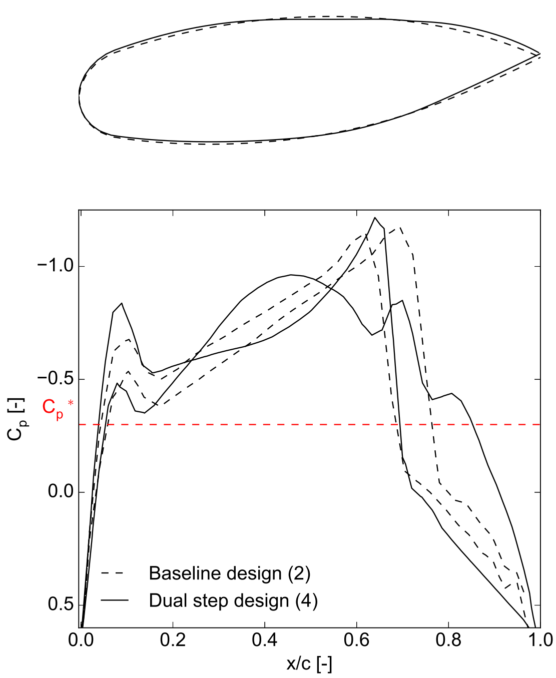

(b) η = 0.70

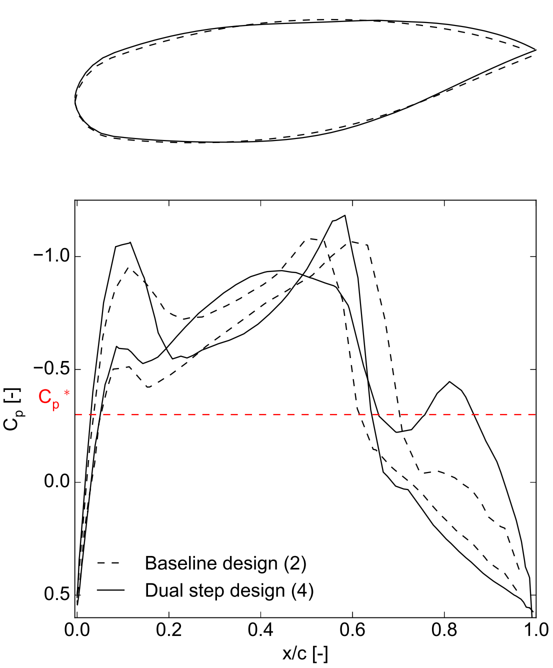

(c) η = 0.80

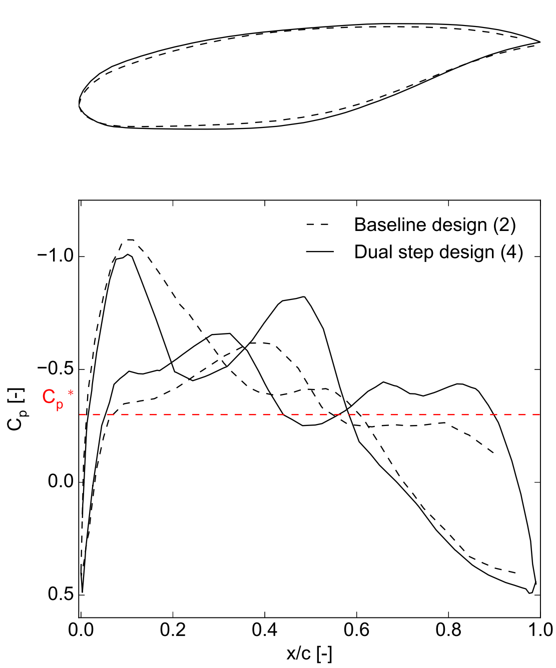

(d) η = 0.90

Figure B.8: RANS-SA pressure coefficient and airfoil section of the baseline (2) and dual step (4) design at C_L = 0.26, Re = 1.135x10^8, M = 0.85 and C_p^* = -0.30 for η = 0.60, 0.70, 0.80 & 0.90.